UNIVERSITY
OF TRENTO - Italy
Department of Physics

Development of Cobalt based Nano Catalysts for Energy and Environment

BY

RAJU EDLA

Doctor of philosophy in Physics

December-2014

APPROVED BY
SUPERVISING COMMITTEE:

Supervisor: Prof. Antonio Miotello

Co-Supervisor: Dr. Nainesh Patel

Development of Cobalt Based Nano Catalysts for Energy and Environment

By

RAJU EDLA

Thesis

Presented to the Doctoral School of Physics

University of Trento at Trento

in Partial Fulfillment

of the Requirements

for the Degree of

Doctor of philosophy in Physics

December-2014

Dedication

To my Family and Friends

Acknowledgement

During the past three years at University of Trento I had the chance to meet lots of new and interesting people. Through scientific discussions with people around me I was able to gain new insights, novel ideas and overcome problems that I had encountered in the course of my research work. Therefore it is impossible to thank every single one personally. Nevertheless a few people deserve a personal thank you.

This is indeed a privilege and great pleasure to express my gratitude and deep regard to my supervisor Prof. Antonio Miotello, who has given me an opportunity under his great supervision. I am also indebted to Dr. Nainesh Patel for his suggestions and guidance to obtain a better understanding of subject and also immense help in preparing manuscripts for scientific publications. It will be always less than whatever I say about these two individuals and however, I express myself to honor their invaluable guidance, keen interest, encouragement, deep involvement, and utmost care on a day to day basis throughout my research work.

I am deeply grateful to Prof. D. C. Kothari for his initial guidance and help while joining in PhD. Moreover, I take this opportunity to thank Dr. Rohan Fernandes for his valuable suggestions and guidance at the beginning of my research career and great help during the first days in Trento. I must thankful to Nicola Bazzanella who has provided me a huge help in obtaining all the SEM images with best quality, and Cristina Armellini for the XRD measurements covered in this thesis.

I am also greatful to Zakaria El Koura and Dr. Michele Orlandi who have always been there to give a helping hand in carrying out my experiments. My sincere thanks to Claudio Cestari for his support with his exceptional skills in fabrication of experimental

set ups. Additionally I would like to thank also technical assistant Lugino for his cooperation in solving the problems related to the experimental setups.

Many of my friends who have helped me in these years; especially I would like to thank all my friends in Trento for their support and encouragement. Along with them I thank all my close friends back in India for being there with me in this period. I express my deepest gratitude to the Almighty for being with me all the time. Finally I thank all those who have, directly or indirectly, helped me all along.

Abstract

There is a rising concern about energy and environment for future. Transition from current fossil fuels to green fuels and building of cleaner environment to lead sustainable life is at enormous task. Hydrogen gas is recognized as a clean fuel and may be a sustainable solution. Hydrogen can be directly used as clean fuel in fuel cells with no harmful by-products. Chemical hydrides with high hydrogen storage capacity in terms of gravimetric and volumetric efficiencies are the most promising candidates to supply pure hydrogen at room temperature. Among them, Ammonia Borane (NH_3BH_3, AB) and Sodium borohydride ($NaBH_4$, SBH) have drawn a lot of interest as they are stable, non-flammable, and nontoxic. Large amount of pure hydrogen gas is released during the *hydrolysis* of these hydrides in presence of certain catalysts and the by-products are non-toxic, environmentally safe and can be recycled. Co based catalysts are considered as good candidates for catalyzed hydrolysis owing to their good catalytic activity, low cost and effortless synthesis. In favor of environmental concern, especially the air pollution (conversion of CO to CO_2) and water pollutions (organic pollutants) are vital problems and there is a serious need to mitigate these problems. Cobalt (Co) based materials are with high catalytic activity for hydrolysis, organic pollutants degradation and CO oxidation. So, a single Co based catalysts as powders and as immobilized coatings prepared by chemical reduction method and pulsed laser deposition (PLD) were studied for hydrogen production by hydrolysis of AB and SBH and thin film coatings Co_3O_4 were studied for CO oxidation and organic pollutants degradation. On the basis of characterization results, the role of catalyst to enhance catalytic activity is discussed in hydrolysis, CO oxidation and pollutants degradation reactions. The stability and reusability of these catalysts have also been investigated.

Table of Contents

List of Tables

List of Figures

Overview of the Thesis

In the **chapter 1**, we have discussed the need for clean energy and environment for the future. How hydrogen can be a promising solution as a clean fuel, especially for vehicular applications and portable devices. Hydrogen can be produced by catalytic hydrolysis of chemical hydrides using appropriate catalyst. This hydrogen can then be supplied to fuel cell to produce electricity. The aim of this thesis is to present catalysts that are economical, easy to synthesize and also have a high hydrogen production rate. **Chapter 2** describes the techniques used for catalysts preparation and the experimental setup that was used to carry out the hydrogen generation measurement. In **Chapter 3**, we see that Co-B powder supported over various mesoporous silica particles such as MCM-41, FSM-16 and SBA-15 for hydrolysis of NH_3BH_3 and Co_3O_4 nano particles assembled coatings for hydrolysis of$NaBH_4$. We discuss the enhanced catalytic activity by studying the effect of the various supports and the catalyst as immobilized form. In **Chapter 4**, we will discuss how the Co_3O_4 nano particles assembled coatings catalyst, operates the methylene blue dye degradation by photo catalysis. After that the Co_3O_4 coatings prepared by physical and chemical methods in the form of 3-D urchin structures for methylene blue dye degradation and a detailed comparative study of the catalyst coatings were discussed. We study and discuss the role of particle size and morphology for enhanced catalytic activity, Later, we also test these catalyst coatings for stability, to check if these catalysts can conserve their enhanced properties for longer times and reuse. In **Chapter 5**, we discuss CO oxidation system design, optimization and for the first time how the Co_3O_4 nano particles assembled coatings prepared by PLD show catalytic activity towards CO oxidation measurements in terms of conversion temperature and stability.

Chapter 1

Energy and Environment

Everything is energy and that's all there is to it. Match the frequency of the reality you want and you cannot help but get that reality. It can be no other way. This is not philosophy. This is physics.

1.1 Introduction

1.1.1 Energy

The world around us has changed significantly over the past few years. Technology has become one of the main drivers of economic and social development. The rapid advancement of Information Technology (IT) all over the world has transformed not only the way we think, but also the way we act. All aspects of human life have been affected by various technologies [1]. Needless to say that practically all the technologies run on electricity and therefore the use and share of electricity is increasing very rapidly time by time, faster than total primary energy supply (TPES). The electricity is generated by various sources of Energy. Energy is one of the major issues which highly affect the economy of a country in the world and the energy requirements for most of the countries are growing at very rapid rate. The major sources for the energy in the world are fossil fuels (Oil, Coal, Nuclear, and Natural Gas). We continue to consume fossil fuels without regard for the consequences. We assume our inherited good fortune of coal, oil and natural gas will go on forever. But are there limits to growth? Yes. The depletion of our resources is not a phenomenon that will happen sometime in the distant future. It is happening now. It has already altered the objectives and alliances of international diplomacy, empowered the political aspirations of producer nations, restructured how world markets work, and changed the economics of fossil fuel exploration, production, transportation and consumption. It is also increasing the price of gasoline, diesel, propane, jet, and heating oil fuels, along with electricity, fertilizer, soil amendments, and thousands of every other products.

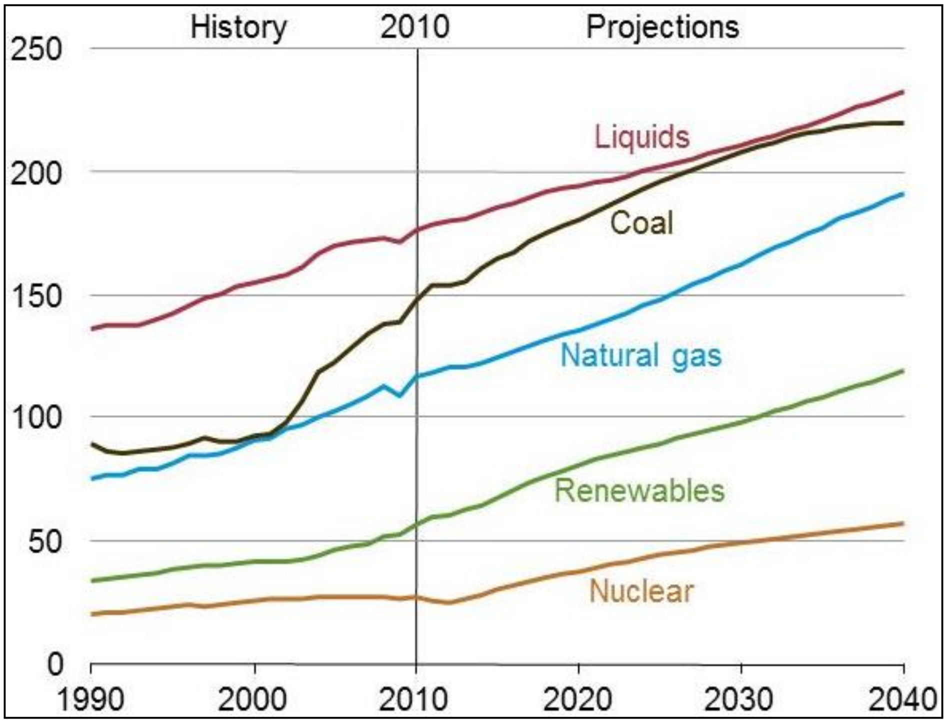

Figure 1.1- World energy consumption by fuel type 1990-2040 (Quadrillion Btu) [2]

From fig. 1.1 it can be seen that the use of the energy sources increasing over the time and the fossil fuels continue to supply most of the world's energy. Natural gas and coal still supply more than three-fourths of total world energy consumption. Petroleum and other liquid fuels remain the largest source of energy, but their share of world marketed energy consumption seems to decline by 2040 [2, 3].

These forms of energy are rapidly depleting, i.e., in the next 40-50 years we will run out of both oil and natural gas respectively, while coal will last only for the next 129 years. If countries do not increasingly diversify their reliance upon fossil fuels, there will be economic tragedies in the near future.

1.1.2 Environment

With a growing population and technology around the world, the need for more energy causing dramatic increase of worldwide consumption of fossil fuels thus creating greater consequences on the environment through release of Green House Gas (GHG) emissions. This causes air pollution and effect on human and aquatic life. The Gases that trap heat in the atmosphere thereby increase the global temperature.

Global carbon emissions from fossil fuels have significantly increased since 1900. Emissions increased by over 16 times between 1900 and 2008. The GHC emissions by human activities and from source of energy are shown in fig. 1.2, clearly indicating that fossil fuels are the primary source for CO_2 gas emissions of 56.6 % (Fig. 1.2b). Energy supply means burning of coal, natural gas, and oil for electricity and heat is the largest single source of global GHC emissions (25.9 %), industry and forestry also contributes to a great extent for GHC emissions[4].

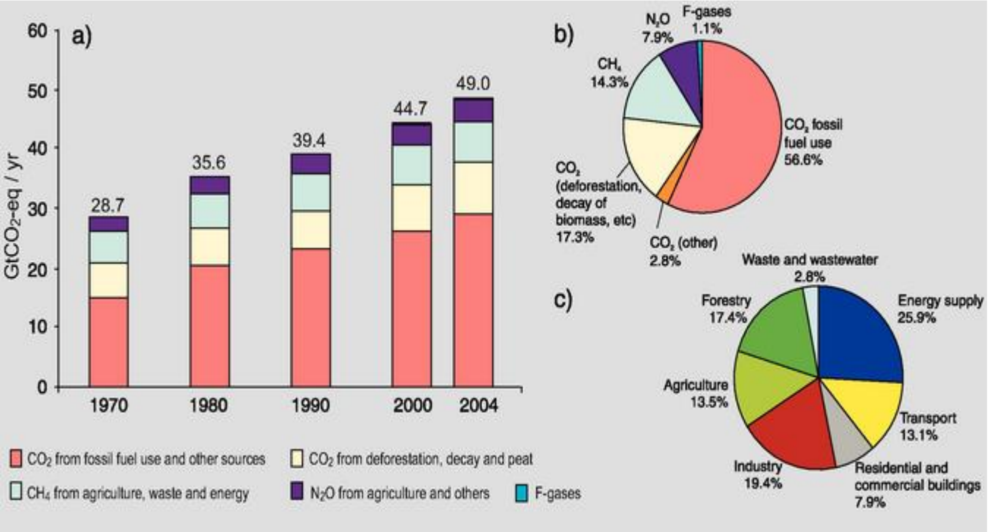

Figure 1.2- (a) Global annual green house gas emissions. (b) Global emissions by human activities, (c) Global emissions by various source of production [4].

The release of GHCs into the environment is causing changes to the earth surface temperature. The global average surface temperature rose 0.6 to 0.9 °C between 1906 and 2005 [5] as shown in fig. 1.3. The rate of temperature increase has nearly doubled in the last 50 years and certainly the temperatures are going to increase further.

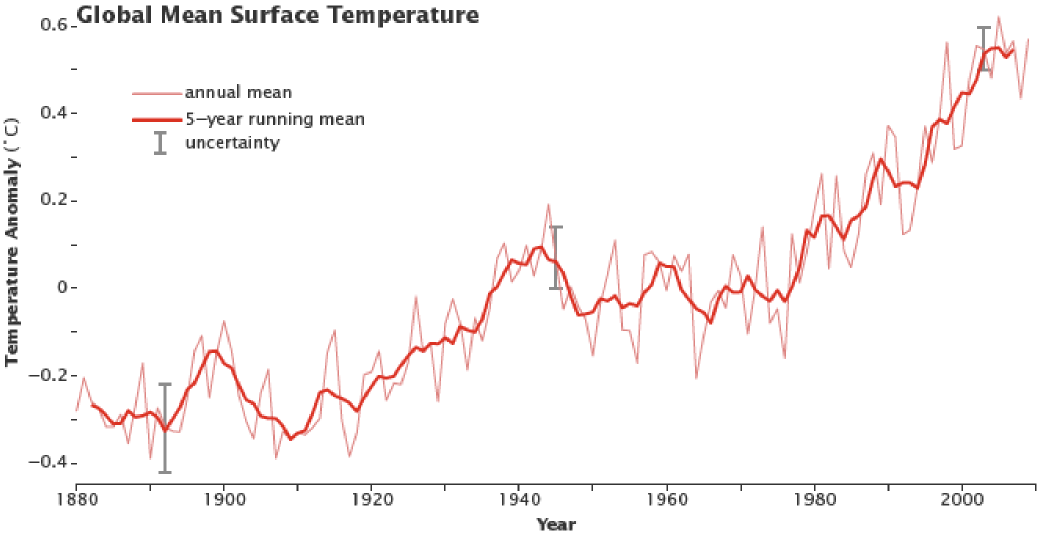

Figure 1.3- Effect of GHG emissions on Global surface mean temperature with time[5].

1.2 Motivation in the search of clean fuels

By looking at the above studied data it is clearly visible that use of the conventional energies such as fossil fuels (coal, natural gas and petroleum), results both in scarcity of energy and environmental impact, e.g. *global warming, acid rains, climate change, water pollution and air pollution* in future. At final, a very poor quality of human life on this planet will result indicating that today's world is facing urgency to switch for an alternative fuels. Concerns about energy security, the impact of fossil fuel emissions on the environment, and sustained high world oil prices support expanded use of *nuclear power and renewable energy*. At the same time awareness in society, government policies for energy, technology developments for cleaner environment and incentives should be provided to improve the prospects for non-fossil forms of energy in many countries around the world. Among the various alternatives sources available, "***Hydrogen (*****H_2*****)"*** is an ideal fuel to replace the fossil fuels. Regarding pollution, we need to find technological solutions to mitigate the present existing scenario by CO_2 capture and storage[6, 7], converting CO_2 into useful fuels by various methods[8, 9]. Carbon Monoxide (CO) is also one of the main air pollutant that has to be taken care off [10]. In the similar way other emissions [11, 12] have to be mitigated to make better future.

1.3 Hydrogen

Hydrogen (H_2) is the lightest element, most abundant, but less than 1% in molecular form[13], non polluting, i.e. by product is only water and can be produced from a large variety of sources mainly from hydrocarbons [13, 14], water splitting by electrolysis[15, 16], thermolysis or hydrolysis reaction of chemical hydrides[17, 18], or reversibly storing it in chemical hydrides [19, 20] and processes driven from solar light[21-23]. Use of H_2 as a fuel will not only reduce our dependence on fossil fuels but also enable energy security, at the same time will take care of the climate change issues. H_2 has a density of only 0.0899 kg/m^3 at normal temperature and pressure, which states that storing H_2 as gas at larger volumes requires very high pressures and safety issues [13]. Liquid hydrogen also has a low density of 70.8 kg/m^3 i.e. 7 % of that of water. The liquid hydrogen has a very low boiling point (20.3 K) and thus requires fairly sophisticated technology to prepare and maintain it in this state[13, 24]. By virtue of exceptionally low density, hydrogen has the best gravimetric energy density of any fuel, but its volumetric energy density is poor. The energy content of H_2 is 141.78 MJ per kg of H_2, 3 times higher than conventional fuel [25].

For a transition to a hydrogen economy to occur through the operation of market forces, H_2 technologies must compete effectively with fossil fuels and other alternatives to them. In particular, devices that use hydrogen such as "*fuel cells*" must compete successfully with devices that use competing fuels (e.g. hybrid propulsion systems) and H_2 must compete successfully with electricity and secondary fuels (e.g. gasoline, diesel fuel and methanol) [26]. If we look at the H_2 cycle from production to end use and compare with carbon cycle, it results the superiority of the H_2 [19] fuel as shown in figure 1.4. H_2 is a sustainable form of energy coming from water and various types of renewable energy filling our surrounding environment with no pollution.

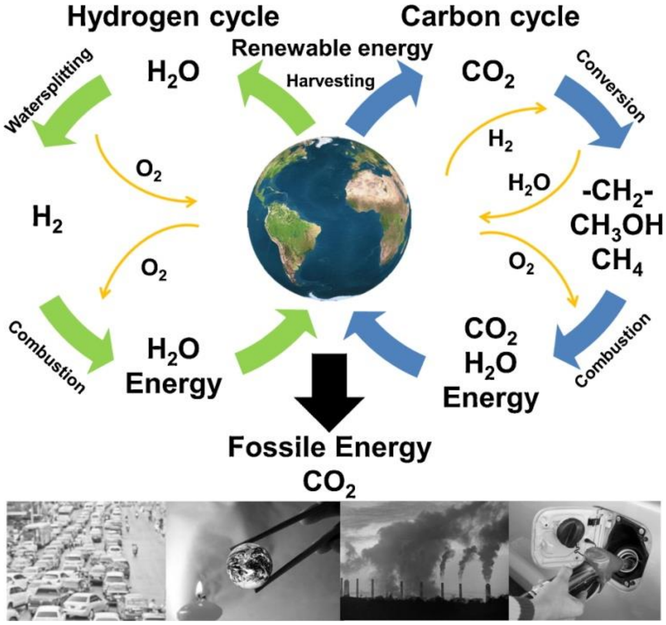

Figure 1.4- Comparative illustration of Hydrogen cycle vs Carbon cycle[19]**.**

1.4 Hydrogen Production

Hydrogen (H_2) has been identified as a most efficient energy carrier which when used in fuel cell produces almost zero emission of greenhouse gases. However, the current production of H_2 is mostly based on steam reforming of natural gas where the final products contain greenhouse gases (CO_2 and CO) [13, 25]. Thus, it is necessary to implement cleaner routes to produce H_2 using least amount of energy to make the hydrogen energy cycle environmentally green. A brief discussion on various H_2 production technologies can give a better understanding idea about need and necessity of alternative technologies to access H_2.

H_2 can be produced from various sources such as, nuclear, natural gas and coal, biomass, and other renewable sources (solar, wind, hydroelectric, or geothermal energy). This diversity of sources makes hydrogen a promising energy carrier and important for energy security. The production of H_2 can be achieved via various process technologies, including *thermal* (natural gas reforming, renewable liquid and bio-oil processing, biomass, and coal gasification), *electrolytic* (water splitting using a variety of energy resources), and *photolytic* (splitting of water using sunlight through biological and electrochemical materials) [27, 28].

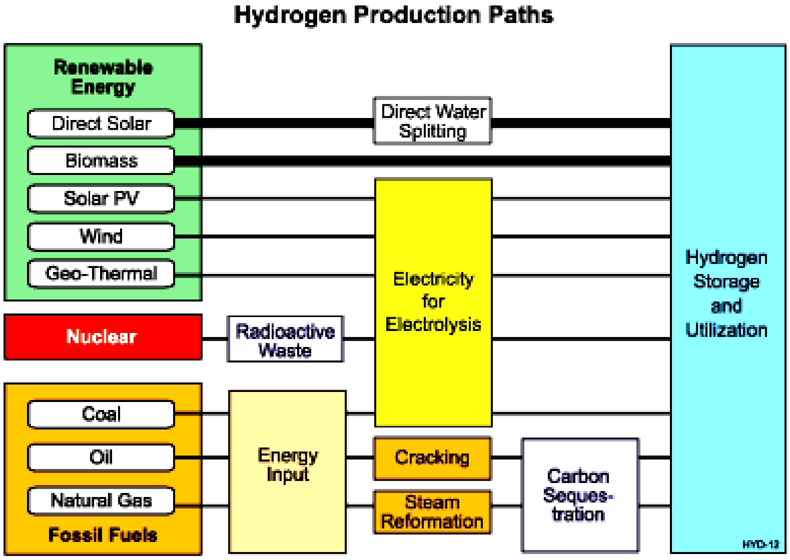

Figure 1.5- Hydrogen production pathways from various sources[29]

The annual production of H_2 is estimated to be about 55 million tons with its consumption increasing by approximately 6% per year. Nowadays, H_2 is mainly produced by the steam reforming of natural gas, a process which leads to massive emissions of greenhouse gases. Close to 50% of the global demand for H_2 is currently generated via steam reforming of natural gas, about 30% from of reforming refinery/chemical industrial off-gases, and 18% from coal gasification, 3.9% from water electrolysis, and 0.1% from other sources [27, 30]. Electrolytic and plasma processes demonstrate a high efficiency for hydrogen production, but unfortunately they are considered as high energy intensive processes [31]. Figure 1.5 shows the existing technologies for H_2 production worldwide and table 3.1 gives information on cost and performances analysis of various techniques for H_2 production [32]. Data from table 1.1 clearly indicating that still H_2 production from fossil fuels is very intensive and most of the other technologies are under research and development stage.

Table 1.1- Cost and performance characteristics of various hydrogen productions [32]

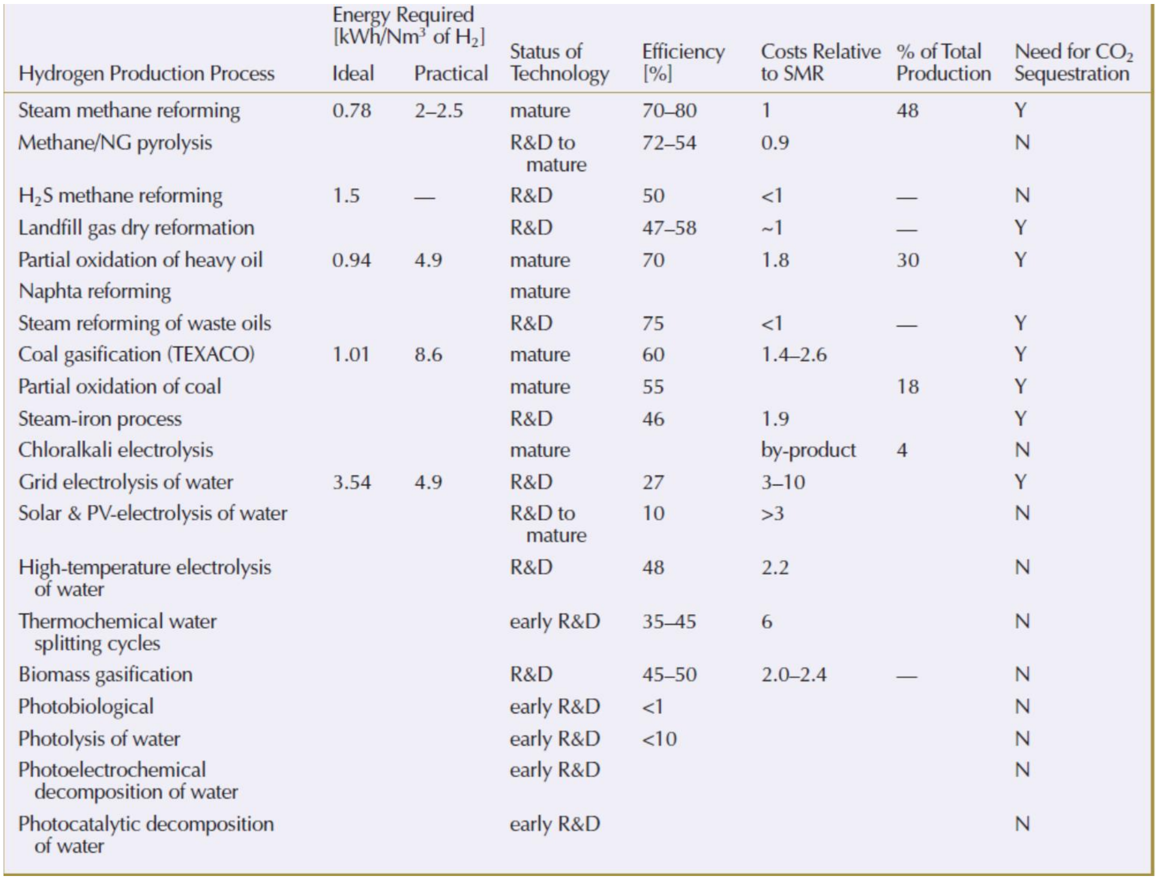

Hydrogen Production Process	Energy Required [kWh/Nm^3 of H_2]		Status of Technology	Efficiency [%]	Costs Relative to SMR	% of Total Production	Need for CO_2 Sequestration
	Ideal	Practical					
Steam methane reforming	0.78	2–2.5	mature	70–80	1	48	Y
Methane/NG pyrolysis			R&D to mature	72–54	0.9		N
H_2S methane reforming	1.5	—	R&D	50	<1	—	N
Landfill gas dry reformation			R&D	47–58	~1	—	Y
Partial oxidation of heavy oil	0.94	4.9	mature	70	1.8	30	Y
Naphta reforming			mature				
Steam reforming of waste oils			R&D	75	<1	—	Y
Coal gasification (TEXACO)	1.01	8.6	mature	60	1.4–2.6		Y
Partial oxidation of coal			mature	55		18	Y
Steam-iron process			R&D	46	1.9		Y
Chloralkali electrolysis			mature		by-product	4	N
Grid electrolysis of water	3.54	4.9	R&D	27	3–10		Y
Solar & PV-electrolysis of water			R&D to mature	10	>3		N
High-temperature electrolysis of water			R&D	48	2.2		N
Thermochemical water splitting cycles			early R&D	35–45	6		N
Biomass gasification			R&D	45–50	2.0–2.4	—	N
Photobiological			early R&D	<1			N
Photolysis of water			early R&D	<10			N
Photoelectrochemical decomposition of water			early R&D				N
Photocatalytic decomposition of water			early R&D				N

Although H_2 is often presented as the near future fuel, the deployment of a hydrogen-based fuel is rather difficult. H_2 has to be *produced, stored, distributed, and used*, but each of these steps is hindered. Intense research focuses on solving the scientific and technological issues on each of them.

H_2 storage is a particularly difficult problem[13, 33]. It is a key issue to be addressed with regard to vehicular applications. It is necessary to store H_2 *safely, easily, reversibly, and at high gravimetric/ volumetric capacities*. Several solutions have been proposed. These are categorized into two groups:

1. Physical storage of H_2 (high pressure, low temperature, and adsorption) and
2. Chemical storage of H_2 (for example, hydrides, amine–borane adducts, and amides/imides). [13, 25, 34].

Adsorption is a borderline situation between physical and chemical storage. However, because most of the adsorbents discussed in the literature only have relatively weak interactions with H_2 and the H_2 is molecularly adsorbed and not dissociated, it is mostly categorized as a physical storage technology. At room temperature and atmospheric pressure, none of the currently-known adsorbents has storage capacity as required. H_2 forms metal hydrides with some metals and alloys leading to solid-state storage under moderate temperature and pressure that gives them the important safety advantage over the gas and liquid storage methods. Metal hydrides have higher H_2-storage density than H_2 gas or liquid H_2 [35]. Hence, metal hydride storage is a safe, volume-efficient storage method for on-board vehicle applications [13, 17-19, 28, 34].

1.5 Fuel cell

There are many advantages with the fuel cells as compared to other power generators like for example high efficiency. A typical combustion-based fossil fuel power plant operates at about 35% efficiency, while a fuel cell operates at about 40 to 60% efficiency to produce electricity [36], noiseless operation, virtually no moving part, by product emission is only water vapor[37]. All these advantages make it as most appropriate and ideal engine or device for greener future. A fuel cell is a device that converts chemical energy from H_2 fuel into electricity through a chemical reaction between hydrogen and oxygen or another oxidizing agent [37]. A simple fuel cell is made of several sections with different materials[36, 38] as shown in figure 1.6.

The chemical reaction sequence in fuel cell is expressed in eq. 1.1 and eq. 1.2 as half cell reactions at Anode and Cathode respectively. Three key sectors in fuel cell are the anode, cathode, and electrolyte. The electrodes are porous and normally made of carbon cloth or carbon fiber [38]. A polymer membrane is sandwiched between the two electrodes. At the interface between the electrode and the polymer membrane there is a layer with catalyst particles (typically platinum supported on carbon) [38].

$$Anode: \qquad H_2 \rightarrow 2H^+ + \ 2e^- \qquad (1.1)$$

$$Cathode: \qquad \frac{1}{2}O_2 \ + 2H^+ + 2e^- \ \rightarrow H_2O \qquad (1.2)$$

There are several types of fuel cells currently under development, each with its own advantages, limitations, and potential applications. They are differentiated by the kind of electrolyte, chemical reaction, fuel, catalyst and temperature required for its functioning. Comparative activity of various fuel cells with efficiency can be found elsewhere in literature [36, 37].

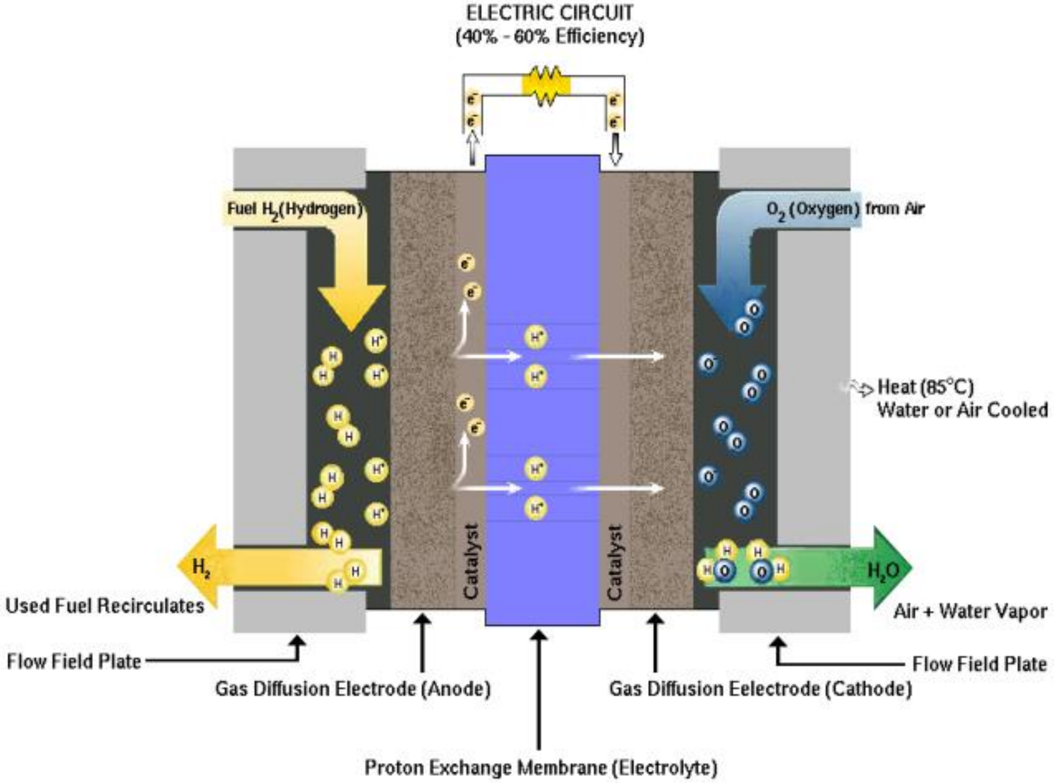

Figure 1.6- A schematics shows an operation of Polymer electrolyte membrane(PEM) fuel cell[36, 38]

Applications of fuel cell devices are vast and can be used from small mobile applications in daily life, stationary applications to transport and industrial applications [39] as depicted in the figure 1.7. Most of the applications are at prototype stage especially for transport and industrial applications because of draw backs associated with durability, stability and cost [39, 40].

The current performances of the fuel cells in various applications are still impressive, reflecting the past few years of enormous research work to improve their performances [40]. But to move towards a genuinely practical technology that can be mass-produced cost-effectively with durability and cost-effectively so that could be viable commercially.

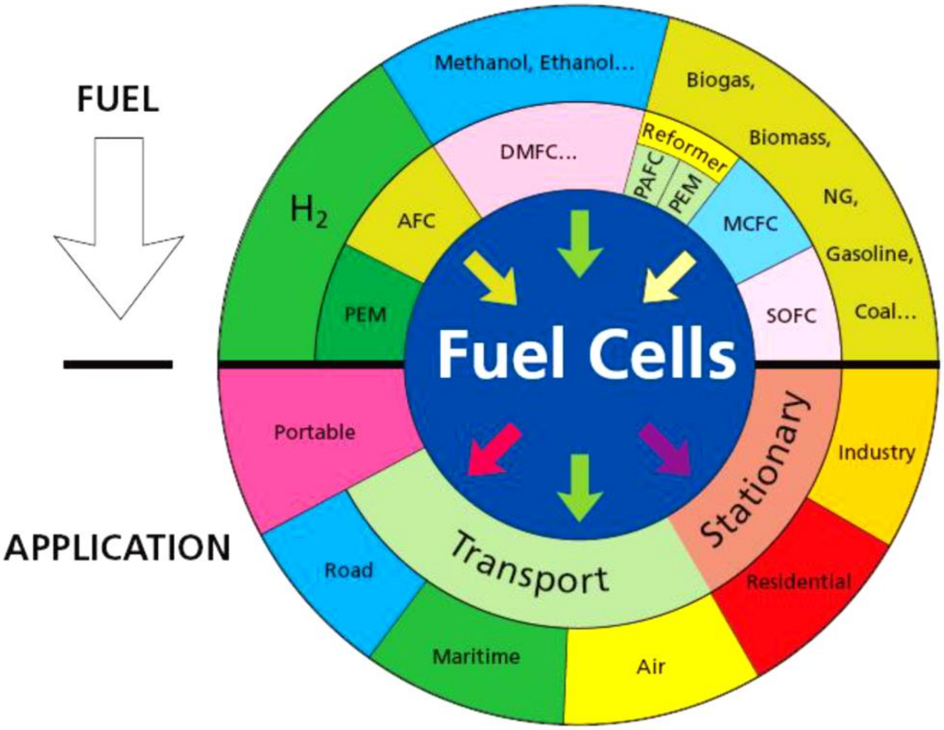

Figure 1.7- Fuel cell technology, possible fuels and application (PEM = Proton Exchange Membrane Fuel Cell; AFC = Alkaline Fuel Cells; DMFC = Direct Methanol Fuel Cell; PAFC = Phosphoric Acid Fuel Cell; MCFC = Molten Carbonate Fuel Cell; SOFC = Solid Oxide Fuel Cell

Chapter 2

Experimental Techniques and Catalysts synthesis

> *"Infancy is irretrievable. Its memories live underground. To what extent they return by stealth are triggered by various catalysts remains an ongoing question."*

2.1 Introduction

A catalyst is a substance that changes the rate of a chemical reaction. Unlike other reagents that participate in the chemical reaction, a catalyst is not consumed by the reaction itself. A catalyst may participate in multiple chemical transformations. Catalytic reactions have a lower rate-limiting free energy of activation than the corresponding un-catalyzed reaction, resulting in higher reaction rate at the same conditions.

Catalysts come in one of two types; homogeneous (reactants and catalyst are in the same phase normally liquid) or heterogeneous (where the reactants and catalysts are in separate phases normally gas or liquids over solids). Heterogeneous catalysts act in a different phase than the reactants. Most heterogeneous catalysts are solids that act on substrates in a liquid or gaseous reaction mixture. The economic contribution from catalysis is very remarkable. Estimates are that catalysis contributes to greater than 35 percent of global gross domestic product (GDP); the biggest part of this contribution comes from the generation of high energy fuels (i.e., gasoline, diesel, hydrogen) which depend critically on the use of small amounts of catalysts in our world's petroleum refineries. As a business, the catalyst market itself is growing, so that catalysis costs are much less than 0.1 percent of the sales revenue from the products which they create.

Catalysis is a key enabling technology in energy conversion, fuel production, and environmental mitigation. Nanomaterials with controlled morphology and electronic structure provide the best platform to catalyze desirable chemical transformations and bring the materials science perspective into catalyst discovery, leading to many opportunities in synthesis, characterization and applications in, for example, electrolyzers, solar cells, fuel cells and metal-air batteries. Today’s needs for clean energy and better environment call for new advanced nanomaterials to catalyze water splitting into hydrogen and oxygen, water purification, CO oxidation, CO_2 reduction into organic fuels, O_2 reduction and efficient fuel conversion. In parallel, there is an ever-increasing need to understand the chemistry happening on the surface of nanomaterials by advanced characterization techniques and modeling. We aimed at improving catalyst synthesis and performance for energy production and environmental clean-up. This chapter explains the experimental methodology adopted to achieve sustainable catalysts in various forms (powers and thin film coatings).

2.2 Synthesis of Powder catalysts

2.2.1 Synthesis of Co-B powder catalysts

Cobalt Boride (Co-B) powder catalyst is synthesized by chemical reduction method. In a typical procedure, an appropriate amount of cobalt chloride, $CoCl_2$ (Sigma-Aldrich) is reduced by using Sodium Borohydride ($NaBH_4$, SB) at room temperature (see eq. 2.1). The molar ratio of SB and $CoCl_2$ was kept larger than 2 to ensure complete reduction of

$CoCl_2$. SB solution was added drop wise in a glass beaker containing the aqueous solution of $CoCl_2$. The mixture is stirred using a magnetic stirrer until hydrogen liberation stops from the solution.

$$2CoCl_2 + NaBH_4 \rightarrow Co_xB + \ NaCl + 2\ H_2 \uparrow (g) \qquad 2.1$$

The resulting black powder of Co-B is separated from the solution by using a filtration process. The powder is extensively washed with distilled water in order to remove Cl^- and Na^+ ions (presence of these ions may degrade the catalytic activity of Co). The powder is finally washed with ethanol (99:9%) and then dried in continuous nitrogen flow at around 323 K.

2.2.2 Impregnation of Co-B nanoparticles in various porous materials

Firstly, various mesoporous silica particles (MSPs) were synthesized by well studied methods in the literature, and then impregnation of the Co-B nanoparticles in the various MSPs such as Mobil composition of matter no. 41(MCM-41), Folded Sheets Mesoporous Materials (FSM-16), Santa Barbara Amorphous (SBA-15) and the non-porous silica particles (NPSs) was carried out.

MCM-41*:* This type of mesoporous silica particles (MSPs) was synthesized by following procedure described in Lai et al. [41], by using *n*-cetyltrimethylammonium bromide (CTAB) as the surfactant template to assemble mesopores on the surface. CTAB (0.25 g) was first dissolved in 120 ml of deionized water and stirred for 30 min. NaOH (2 M, 0.875 ml), as a catalyst, was added to the above mixture, followed by adjusting the temperature at 353 K. Drop wise addition of tetraethylorthosilicate (TEOS, 99.999%) (1.25 ml) was carried out to the surfactant solution and resulting mixture was stirred at 353K for 2 h to obtain white silica precipitate. The solid powder obtained by centrifuging was washed thoroughly with distilled water and dried in vacuum at ambient temperature. After drying, silica powder (0.7 g) was refluxed in solution of 70 ml of methanol and 3.5 ml of HCl (35%) for 24 h in order to remove surfactant template (CTAB) over the surface. The white powder was separated by centrifuging the solution and later washed with distilled water and methanol followed by drying in vacuum. The obtained powder was treated at 398 K for 2 h to remove the OH^- group from the pore surface.

FSM-16: Kanemite ($NaHSi_2O_5$) and CTAB were used as precursor and template, respectively, to synthesize FSM-16 type MSP followed the method described in literature [42]. To synthesize kanemite, NaOH of 100 ml (0.528 M) was added to 50 g of sodium silicate solution ($SiO_2/Na_2O = 2.21$) to adjust $SiO_2/Na_2O = 2$. The mixture was stirred for 3 h at ambient temperatures. The excess water was removed by drying the solution at 393K for 15 h. After crushing, the dried sodium silicate powder was calcinated at 973K for 6 h in air to obtain white kanemite foam. Crushed kanemite powder (2 g) was dispersed in 20 ml of distilled water and stirred for 3 h. The resulting suspension was filtered out to obtain wet kanemite paste. This paste was mixed into 32 ml of CTAB (0.125 M) solution and then stirred for 3 h at 343 K. The pH of the dispersion was adjusted to 8.5 by adding HCl solution (2 M). The resulting mixture was stirred for another 3 h at 343 K. After cooling, filtered solid powder was washed with distilled water and then dried in air at ambient temperature. The as-synthesized silica powder was calcinated at 873 K for 6 h to remove the surfactant from the silica material to obtain FSM-16 MSP.

SBA-15: Pluronic (P123) was used as the surfactant template to fabricate SBA type MSP. The synthesis was carried out without hydrothermal conditions using the procedure described in Brahmkhatri et al.[43]. P123 (4 g) was first dissolved in 150 ml of HCl solution (2 M) under constant stirring at 308 K for 2 h. Later TEOS (8.5 g) was added to the above mixture and stirred for 20 h at 308 K. The resulting solution mixture was aged at 353 K for 48 h. The solid powder was separated by filtration and followed by washing with distilled water and ethanol. After drying at room temperature, the white powder was calcinated at 773 K for 6 h to burnout template molecules from the silica material.

Non-Porous Silica particles (NPSs) were also prepared by Stober method [44] by hydrolysis and condensation of TEOS in ethanol, and in the presence of ammonia (NH_3) as catalyst. The molar ratio of TEOS: NH_3: H_2O: Ethanol was kept about 1:1:10:30.

The Co-B catalyst was loaded on NPSs and on three different types of MSPs (MCM-41, SBA-15 and FSM-16) by impregnation–reduction method. 300 mg of all types of silica particles were immersed in the 4.5 ml of aqueous cobalt chloride solution (0.5 M). To have better particle dispersion the mixture was ultra-sonicated for 10 min and later left undisturbed for 24 h. After impregnation the samples were filtered to remove the excess $CoCl_2$ solution and dried in vacuum condition. The dried mixture was reduced by addition of 4.5 ml of aqueous $NaBH_4$ solution (1 M) and later stirred until the bubbles generation was ceased. The gray powder formed during the reaction was separated from the solution by sedimentation and filtration and later washed several times with distilled water and ethanol. In the end the catalyst was dried in vacuum under ambient condition.

2.2.3 Synthesis of Co_3O_4 Powder catalyst

Co_3O_4 Powder was prepared by the co-precipitation (CP) method as reported in the literature[45]. Diluted ammonia solution (25%) was added as a precipitator to the homogeneous 0.04 M aqueous solution of $CoCl_2$ under continuous stirring. After stirring at room temperature, the obtained cobalt hydroxide ($Co(OH)_2$) precipitate was filtered and subsequently washed with distilled water and ethanol. Finally, the $Co(OH)_2$ precipitated was vacuum dried and thermally decomposed at 400 °C for 2 h to obtain the Co_3O_4 powder.

2.2.4 Synthesis of 3D-Hierarchical Co_3O_4 urchins

3D-Hierarchial Co_3O_4 urchin-like nano structures were prepared by hydrothermal synthesis adapted from literature [46]. Typically, 1 mmol of $Co(NO_3)_2 \cdot 6H_2O$, 3 mmol of NH_4F and 5 mmol of $Co(NH_2)_2$ were dissolved in 35 ml of deionized water and sealed in a custom-built Teflon-lined aluminum autoclave with a 50 ml capacity (see figure 2.1).

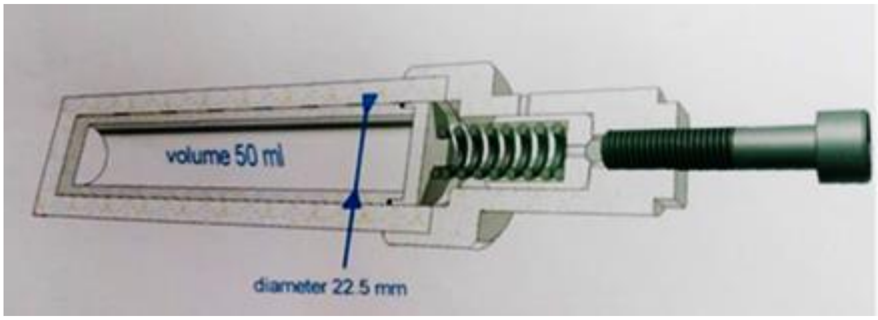

Figure 2.1- Schematic of custom-built Teflon-lined aluminum autoclave with a 50 ml capacity

The reactor was heated at 120°C for 5 h and allowed to cool down at room temperature. A pink precipitate was then collected by filtering on a sintered glass buchner funnel, washed several times with water and isopropanol and dried in air at 70°C for 45 min. The same procedure was followed to obtain thin films on glass, Si and fused silica substrates by placing them inside the reactor during the process. The obtained pink powders were annealed at temperatures 400 °C, 500 °C and 600 °C for 4 hr in a tubular furnace.

2.3 Synthesis of thin film catalysts

Two dimensional materials created by the process of condensation of atoms, molecules or ions, are called thin films. They have unique properties significantly different from the corresponding bulk materials as a result of their physical dimensions, geometry, and non-equilibrium microstructure. These characteristic features of thin films can be modified and tailored to obtain desired properties. The special properties of the thin films are that they are not fully dense, under stress and with defects. These features are the best qualities to design required supplies for science and technology. There are vast applications, starts from familiar household mirrors to optical coatings, very large scale integrated (VLSI) circuits, quantum engineering, integrated optics, energy and environment applications. The thin films could be of any type as metallic, oxides, alloys or mixed oxides depending on their specific application in various fields.

Progress in each of these areas depends upon the ability to selectively and controllably deposit thin films - thickness ranging from tens of nanometers to micrometers. It requires control often at the atomic level of film microstructure and microchemistry. There are a vast number of deposition methods available and in use today. All methods have their specific limitations and involve compromises with respect to process specifics, substrate material limitations, expected film properties, and cost. This makes it difficult to select the best technique for any specific application. Figure 2.2 explains the important parameters required, optimized or controlled to have the thin films of interest for applications.

The basic steps for the formation of a thin film are; emission of particles from the target material, transport and condensation on the substrate, each step is important to have the required properties of the film. The growth of the film on the substrate is very important and it involves the steps as nucleation, island formation and growth, coalescence of the islands and continued growth leads to have the final form. The nucleation and growth occur at defects or where the sites have high bonding energy [47].

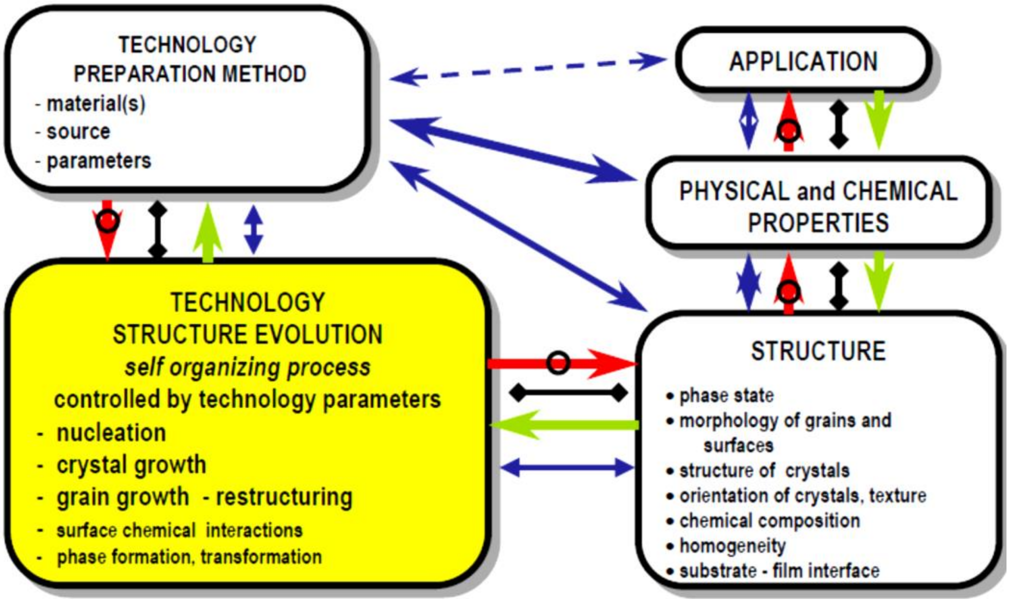

Figure 2.2- Important aspects of technology for the evolution of thin film materials of interest.

Deposition techniques fall into two broad categories, depending on whether the process is primarily chemical or physical.

2.3.1 Chemical deposition techniques:

Chemical vapor deposition (CVD) processes are widely used in industry due to their versatility for depositing a very large variety of elements and compounds. Here, a fluid precursor undergoes a chemical change at a solid surface, leaving a solid layer. Thin films from chemical deposition techniques tend to be *conformal*, rather than *directional*.

Chemical deposition is further categorized by the phase of the precursor as; Plating, Chemical solution deposition (CSD) or Chemical bath deposition (CBD), sol-gel, Chemical vapor deposition (CVD) ,MOCVD, Plasma enhanced CVD (PECVD), and Atomic layer deposition (ALD) [48].

Advantages:

- Uniform distribution over large areas.
- No compositional gradients across substrate.
- No need to break vacuum for source changes.
- More selective area deposition because of higher Activation energy for reaction with foreign substances.

Disadvantages:

- Mostly involve safety and contamination.
- Hydrides and carbonyls are poisonous (especially arsine).
- Metal organics are pyrophoric (ignite in contact with air).
- High cost for compounds with sufficient purity.

2.3.2 Physical vapor deposition techniques:

Physical deposition uses mechanical, electromechanical or thermodynamic means to produce a thin film of solid. Since most engineering materials are held together by relatively high energies, and chemical reactions are not used to store these energies, commercial physical deposition systems tend to require a low-pressure vapor environment to function properly; most can be classified as physical vapor deposition (PVD). The whole system is kept in a vacuum deposition chamber, to allow the particles to travel as freely as possible. Since particles tend to follow a straight path, films deposited by physical means are commonly *directional*, rather than *conformal, the various deposition techniques* are listed as Thermal evaporation techniques (Electron beam evaporation, Molecular beam epitaxy), Sputtering (DC, RF,), electro-hydrodynamic deposition (electro spray deposition), cathode arc deposition (Arc-PVD), Pulsed laser deposition (PLD) [48].

Advantages:

- Directional deposition.
- No need of chemicals as in chemical deposition techniques and extensive cleanups (are not environmentally friendly).
- Safer than those methods.
- Can be used on almost any type of inorganic material.

Disadvantages:

- Higher costs.
- The process requires complex machines that need skilled operators. Also, the rate at which coating is relatively slow.
- However, PVD coating is still one of the most effective methods of improving a surface’s strength and durability.

Pulsed laser deposition (PLD) technique: *PLD* especially used in this work is a physical method of thin film deposition where a pulsed laser beam, of wavelength generally in the UV range, is employed to ablate a target composed of the desired thin film material. PLD attracted much attention over the last 20 years, as it enables fabrication of multi-component stoichiometric films from a single target. The decoupling of the vacuum hardware and the evaporation power source makes this technique so flexible that it is easily adaptable to different operational modes without the constraints imposed by the use of internally powered evaporation sources. Applications of the technique range from the production of superconducting and insulating circuit components to improved wear and biocompatibility for medical applications. It is also used to deposit wide range of diamond-like carbon (DLC), ferroelectrics and wide band-gap semiconductors.

Basic Principle: In the deposition process a pulsed laser beam is focused on a piece of source material, in general referred to as the target (figure 2.3). The focusing of the laser beam results in a locally very high energy density (fluency) on the target surface. Upon absorption from a solid surface, the electromagnetic energy of the laser beam is converted first in electronic excitation and then in thermal, chemical and mechanical energy, that causes evaporation. The vaporized material, containing neutrals, ions, electrons etc., is known as a laser-produced plasma plume and expands rapidly away from the target surface (velocities typically ~10^6cms^{-1} in vacuum).

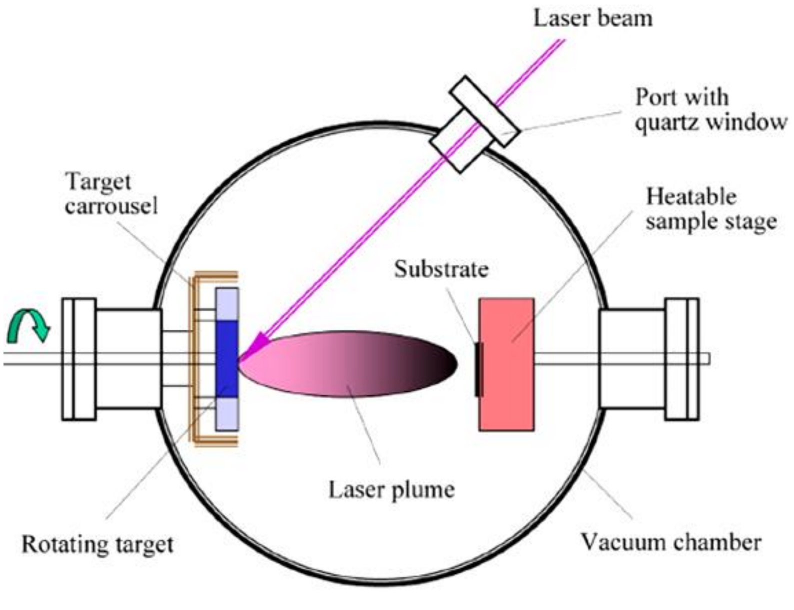

Figure 2.3- Schematic diagram of Pulsed Laser Deposition

Film growth occurs on a substrate upon which some of the plume material re-condenses. In practice, however, the situation is not so simple, with a large number of variables affecting the properties of the film, such as laser fluence, background gas pressure and substrate temperature. These variables allow the film properties to be manipulated somewhat, to suit specific applications.

Deposition Parameters: In a pulsed laser deposition system the adjustable parameters are: energy per laser pulse, pulses frequency, target to substrate distance, substrate temperature, and background gas pressure. The control of such parameters can be more or less critical for the quality of the film.

Experimental set-up: The experimental set-up [49] is schematically represented in Figure 2.4. The energy source used in the experiments is a KrF (λ = 248nm) excimer laser (LPX220i Lambda Physik) capable of operating at frequencies between 1 − 200 Hz. The pulse width is about 20 ns (FWHM) and the maximum pulse energy is 450mJ, having a maximum average power of 80W. The pulse energy can be lowered by dropping the pumping high voltage. The beam dimensions are 8mm ×23mm (vertical x horizontal), with the beam divergence of 1 mrad ×3 mrad (V x H). The beam is deflected by 90 ° using a dielectric mirror. The beam can be focused by a 30 cm focal length lens mounted on a slide permitting it to be moved along the beam direction. The slide is used to change the energy fluence on the target. The focused beam finally enters the chamber through a fused silica window and impinges on the target at 45°. Prior to the deposition PLD chamber was evacuated up to a base pressure of 10^{-6} mbar.

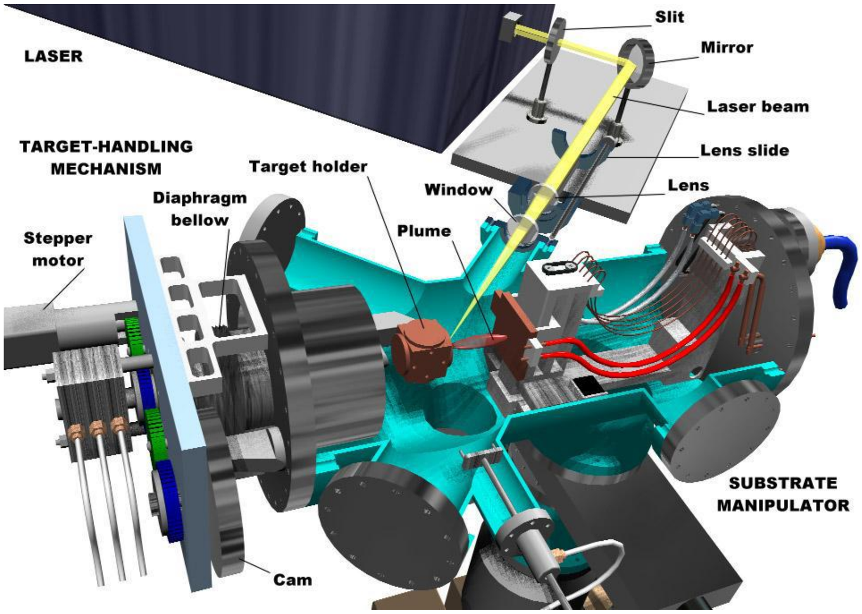

Figure 2.4- 3D view of our PLD apparatus [40]

Advantages: The technique of PLD was found to have significant benefits over other film deposition methods, including:

- The capability for stoichiometric transfer of material from target to substrate
- Control in thickness with energy and time of ablation
- Thus deposition can occur in both inert and reactive background gases.
- The use of a carousel, housing a number of target materials, enables multilayer films to be deposited without the need to break vacuum
- Different morphological and structural films can be obtained by changing the deposition parameters.
- Deposition of very small amounts as required (important for costly materials)

Disadvantages: In spite of these significant advantages (mentioned above), industrial uptake of PLD has been slow and to date most applications have been confined to the research environment.

- The plasma plume created during the laser ablation process is highly forward directed therefore the thickness of material collected on a substrate is highly non-uniform.
- The area of deposited material is also quite small.
- The ablated material may contain macroscopic globules of molten material, up to ~10μm diameter. The arrival of these particulates at the substrate is obviously detrimental to the properties of the film being deposited.
- The fundamental processes, occurring within the laser-produced plasmas, are not fully understood; thus deposition of novel materials usually involves a period of empirical optimization of deposition parameters.

2.3.4 Synthesis of nano particles (NPs) assembled Co_3O_4 and Co-B coatings

This section covers the preparation of nanoparticles (NPs) assembled Co_3O_4 and Co-B coatings with optimized parameters to achieve high catalytic results. To prepare catalyst films of Co-B, the catalyst powder was first synthesized by using the above mentioned chemical procedure (section 2.2.1). The powder is then cold pressed to cylindrical disks in on a stainless steel holder and is used as a target. PLD is performed at a repetition rate of 20 Hz, in vacuum and reactive oxygen atmosphere (4.5×10^{-2} mbar). Cobalt oxide films (Co_3O_4) are deposited by using a pure Co target under oxygen gas atmosphere (4.5×10^{-2} mbar) at various laser fluences with substrate temperature room temperature and 150 °C. The films are deposited on silicon substrates for the characterization and on glass substrates for testing their catalytic activity. The target to sample distance is maintained at 4.5 and 5.5cm for Co-B and Co_3O_4 respectively. Weight of the catalyst films is evaluated by measuring the weight of the glass before and after deposition, and kept approximately constant for all laser fluences by varying the number of laser pulses during deposition.

2.4 Hydrogen Measurement Set up

2.4.1 Experimental setup

The apparatus for hydrogen production is schematically divided in two main parts: *reaction chamber* (reactor) and *measurement system*.

Reaction chamber: The reactor is composed of a cylindrical flat flange vessel with off-centre bottom outlet valve and a stirrer guide at the bottom (see figure 2.5). It is surrounded by a jacket connected to a heating circulator bath for temperature control. The temperature is controlled within ±0:1K by a water bath with a digital temperature controller. The reactor is closed by a flat flange lid with five necks (a central socket, two angular side sockets and two parallel side sockets). There is a catalyst holder inside the reactor which is used to hold powder and thin films for the hydrolysis reaction.

Gas-volumetric (GV) measurements: In figure 2.5, a schematic diagram of the experimental apparatus for GV measurements of H_2 evolved from the catalyzed hydrolysis reaction is shown. The reactor is coupled through a gas tube with an Erlenmeyer flask containing water; the latter, in turn, is connected to a graduated cylinder placed on an electronic precision balance positioned lower with respect to the reactor and flask. The reaction chamber and the Erlenmeyer flask are assembled in a closed system. The decoupling between the flask and the cylinder is guaranteed by a stop cock. When the system is closed and the stop cock opened, the altitude difference between the flask and cylinder permits us to maintain a differential pressure between the two vessels.

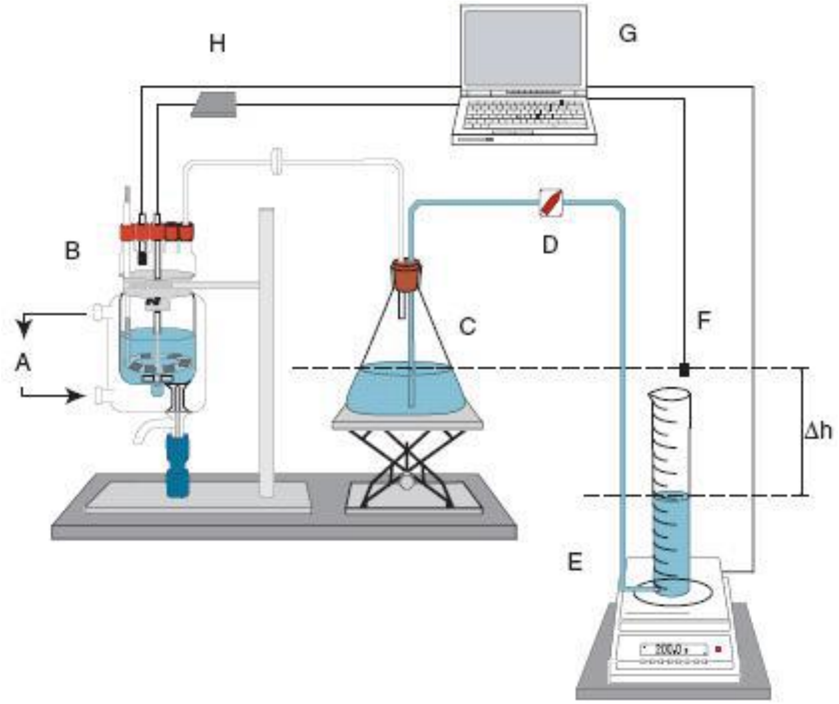

Figure 2.5 – Schematic diagram of the experimental apparatus for GV analysis: (A) thermostatic water bath system, (B) reaction chamber, (C) Erlenmeyer flask with water reserve and elevator, (D) stopcock, (E) graduated cylinder and electronic balance, (F) external pressure sensor, (G) input-output board and acquisition software, (H) stepper motor controller. The height-difference Δh between the water level contained in the chamber-flask system and that in the cylinder is also indicated [50].

This configuration ensures an air-tight seal of the whole system with a maximum inlet pressure up to 105 Pa relative to the ambient pressure. A typical experiment consists in the addition of 200 ml of reaction solution in the reactor. The catalyst (in the form of a film, powder or liquid) will be placed on the catalyst holder and inserted into solution and The H_2 production measurements will be done [50]. All electronic devices are controlled via a PC through data acquisition, it reads inlet and outlet pressure with two analogue inputs controls the stepper motor drive module and collects the experimental data.

2.5 Characterization of the catalysts

The surface morphology and composition of catalysts was studied by field emission gun scanning electron microscope (FEG-SEM, JSM 7001F, JEOL) equipped with energy-dispersive spectroscopy (EDS, INCA PentaFET-x3). Phase identification of the samples were studied recording Raman spectra with HORIBA JobinYvon Lab RAM Aramis Raman spectrometer with diode pumped solid state laser at 634 nm. Structural characterization of the samples in small-angle and wide-angle was performed by conventional X-ray diffraction (XRD) using the Cu Kα radiation (λ = 1.5414 Å) in Bragg–Brentano (θ–2θ) configuration. The Brunauer, Emmett and Teller (BET) surface area of the silica particles and Co-B supported over silica was determined by nitrogen absorption at 77 K using Quanta-chrome instrument (Quadra-Sorb 5.04) after degassing at 473 K for 2 h. Pore size, pore wall thickness of MSP, and pore structure, particle size and planes identification were examined by high resolution transmission electron microscope (HR-TEM) with a field emission FEI TECNAI F20 Super Twin FEG (S) TEM microscope operating at 200 kV

Chapter 3

Hydrolysis of Chemical Hydrides in presence of incorporated Co-B nano particles in Porous materials and Co_3O_4 Coatings

"The amount of sunshine energy that hits the surface of the Earth every minute is greater than the total amount of energy that the world's human population consumes in a year!

3.1 Introduction

H_2 from the chemical hydrides can be produced by either thermal decomposition [18] (thermolysis), or by hydrolysis [33]. Ammonia borane (NH_3BH_3, AB) and Sodium Borohydride ($NaBH_4$, SB) with high gravimetric and volumetric hydrogen storage ability are the most prospective candidates to supply pure H_2 for portable and on-board application at room temperature.

Ammonia borane (NH_3BH_3, AB) has come to the forefront in the 21st century. Though it has been known since 1955 when its synthesis was reported [51], it was only recently that this molecule attracted a considerable attention because of its H_2 storage capability [52]. AB has many attractive attributes, such as low molecular weight (30.7 $gmol^{-1}$), high H_2 densities (19.6 wt% H_2 and 0.145 $kgH_2\ L^{-1}$), relatively safe storage (relatively stable), and low-temperature dehydrogenation behavior. However, it also has drawbacks, and the most significant and problematic is storage irreversibility. Consequently, if sustainability is targeted, hydrogen must be regenerated off board.

H_2 can be produced either thermal decomposition of AB, or hydrolytic decomposition. The first is a three-step process, The first step commences at approximately 100 °C and releases 1 equiv. of H_2 (6.5 wt %). The second step occurs at a broad temperature range centered at approximately 150°C. The final step, which requires high temperatures (>1200°C), provides the third equivalent of H_2. Unwanted gaseous byproducts, such as borazine ($B_3N_3H_6$), are also liberated [53]-[54]. Alternative way to produce pure H_2 is Hydrolysis. It is safe and there is no observance of any unwanted products, and this reaction happens at room temperature very efficiently.

3.2 Hydrolysis of Chemical hydrides: NH_3BH_3 and $NaBH_4$

Hydrolysis is the second route for AB dehydrogenation [33, 55]. An aqueous solution of AB at pH 7 is stable for more than 80 days[56] The hydrolysis reactions AB is shown in equations 5 and 6 respectively[20].

$$NH_3BH_3 + 2H_2O \rightarrow BO_2{}^- + NH_4{}^- + 3H_2(g) \qquad 3.1$$

Therefore, H_2 release has to be catalyzed, and so far several metal-based catalysts have been studied and end product after hydrolysis is non toxic and environmentally safe. The hydrolysis reaction rate can be effectively increased by using several inorganic and organic acids but the reaction usually becomes uncontrollable. On the other hand, *solid state catalysts* such as precious and transition metals and their salts are found to be very efficient in accelerating the hydrolysis reaction in a controllable manner.

Noble catalysts like Pt, Rh, and Pd [57], Nano-clusters of noble metals Ru, Rh, Pd, Pt and Au supported on γ-Al_2O_3, C and SiO_2 [56], recyclable Au@Co core shell nanoparticles [58], Ni-Pt hollow nano spheres [59] have been utilized to enhance the H_2 production rate. However, these catalysts do not seem to be viable for industrial application by considering their cost and availability. Transition metals such as Co, Fe and Ni, when fabricated on nano scale with high surface area, can exhibit catalytic performance comparable to that of noble metals. Therefore a wide attention has been given to the non noble metals. Co, Fe, and Ni nano particles [60, 61], and Ni- supported on SiO_2 Al_2O_3, CeO_2 [62] and Co, Cu and Ni supported on γ-Al_2O_3, SiO_2 and C [63, 64].

Among the low cost materials, Cobalt Boride (Co-B) showed an exceptional catalytic activity mainly owing to its unique properties with high concentration of coordinative unsaturated sites, and its chemical stability [65, 66]. In addition, Co-B can be produced by simple chemical reduction of cobalt salt. However, due to the exothermic nature of the reduction reaction and ferromagnetic nature of the material, the produced Co-B NPs agglomerate to reduce the effective surface area which in turn hampers the catalytic activity considerably. Several routes were adopted in the past to avoid the agglomeration such as by doping with transition metals[67-69], by using organic templates [70] or by supporting the catalyst on high surface area materials such as rough carbon [71, 72]. However, the preparation of catalyst NPs of desired size, which allows tuning of catalytic activity, still remains a challenge. Thus, it is of paramount importance in developing a system that can provide a degree of freedom to control the size of the catalyst NPs during preparation as well as to maintain this size during the catalytic reaction and also at elevated temperatures. Thus, due to all these reasons, catalyst particles supported over porous materials such as alumina, silica, carbon, and zeolites seems to be a better option to deliver sustainable solution with improved catalytic activity for hydrolysis of AB.

Sodium tetrahydroborate ($NaBH_4$), shortly called sodium Borohydride (SB), is widely used as a reducing agent in industrial and laboratory applications. Due to its large volumetric (0.115 kg H_2 L^{-1}) and gravimetric (10.7 wt %) H_2 storage capacity, it has a high potential to be used as a synthetic fuel either in a direct Borohydride fuel cell or as a hydrogen storage material for mobile application [73]. Alkaline solution of SB is quite stable, non-flammable and non-toxic in nature and can produce H_2 on demand in presence of appropriate catalyst under ambient condition [68, 74]. For the commercial success of SB based H_2 generation system, the cost of SB must be substantially reduced. Recycling of sodium borate reaction product back to SB starting material is presently being studied. SB decomposes thermally to liberate H_2 [75], but the decomposition temperatures are above5 500 °C, so the thermolysis of SB is not give much attention. SB hydrolysis is most studied reaction because it generates H_2 at room temperature in presence of appropriate catalyst. The hydrolysis reaction of SB is shown in eqn. 6.

$$NaBH_4 + \ 2H_2O \rightarrow NaBO_2.2H_2O + 4H_2(g)\uparrow \qquad 3.2$$

The amount of H_2 produced and its generation rate to a great extent depends on the quality of the used catalyst. Traditionally, in the past, various noble metals were studied extensively like Pt, Pd, Ru [68] as solid-state catalysts to enhance the H_2 production rate. However, high cost and scarcity of these precious metals make it necessary to explore new routes to either minimize the usage of these metals or replace them with non-noble catalysts having comparable catalytic properties.

Overall, SB conversion is >90%. The most efficient catalyst reported so far is 10 wt% PtRu–$LiCoO_2$ [76, 77]. A H_2 generation rate of 560 L_{H2} min^{-1} $g_{PtRu}{}^{-1}$ was measured at 25°C for an aqueous solution with an effective capacity of 2.5 wt% [78]. However Pt is a noble metal. Hence cheaper metals have been investigated. The most attractive non-noble metal is cobalt [77]. For example, a 10 wt% Co–C catalyst showed a H_2 generation rate of about 130 L_{H2} min^{-1} g_{Co}^{-1} at 20 °C [79]. The methodology for highly active and stable catalysts is making supported nano particles to avoid agglomeration

3.3 Catalysts for Hydrolysis of Ammonia Borane (NH_3BH_3, AB)

Catalyst in the form of Co-B nanoparticles supported on various mesoporous silica particles (MSPs) such as Mobil composition of matter no. 41(MCM-41), Folded Sheets Mesoporous Materials (FSM-16), Santa Barbara Amorphous (SBA-15) and the non-porous silica particles (NSPs) was synthesized by chemical impregnation-reduction method as discussed in Chapter 2. After successful synthesis the catalyst powders were studied by various characterization techniques then employed for H_2 production by hydrolysis of AB, and compared with bare Co-B catalyst powder.

3.3.1 Morphological analysis of the catalysts

Scanning Electron microscope (SEM) image (fig. 3.1) of bare Co-B powder shows particle-like morphology having spherical shape and size in the range of 30-40 nm. Nevertheless all these particles are mostly present in agglomerated state.

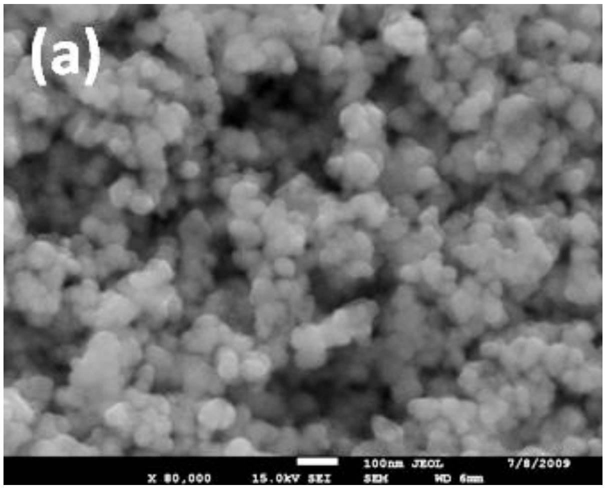

Figure 3.1- SEM image of bare Co-B powder

Agglomeration of the bare Co-B catalyst particles is due to the exothermic nature of the reduction reaction of $CoCl_2$ in presence of $NaBH_4$ and the high surface energy involved, these particles are mostly present in agglomerated state to acquire low specific surface area. In addition, ferromagnetic nature of the Co-B particles can also assist in agglomeration of NPs.

Transmission Electron microscope (TEM) images of unsupported NSPs and Co-B@NSPs are shown in fig. 3.2a and fig.3.2b. The unsupported NSPs particles are perfectly spherical and smooth surface with narrow size distribution in the range of 150–160 nm. The size of Co-B particles (30-40 nm) (dark spheres in fig. 3.2b) supported on the NSPs is similar to that of bare Co-B powder but slightly less agglomeration is observed on the support surface (see fig. 3.1 and fig 3.2b).

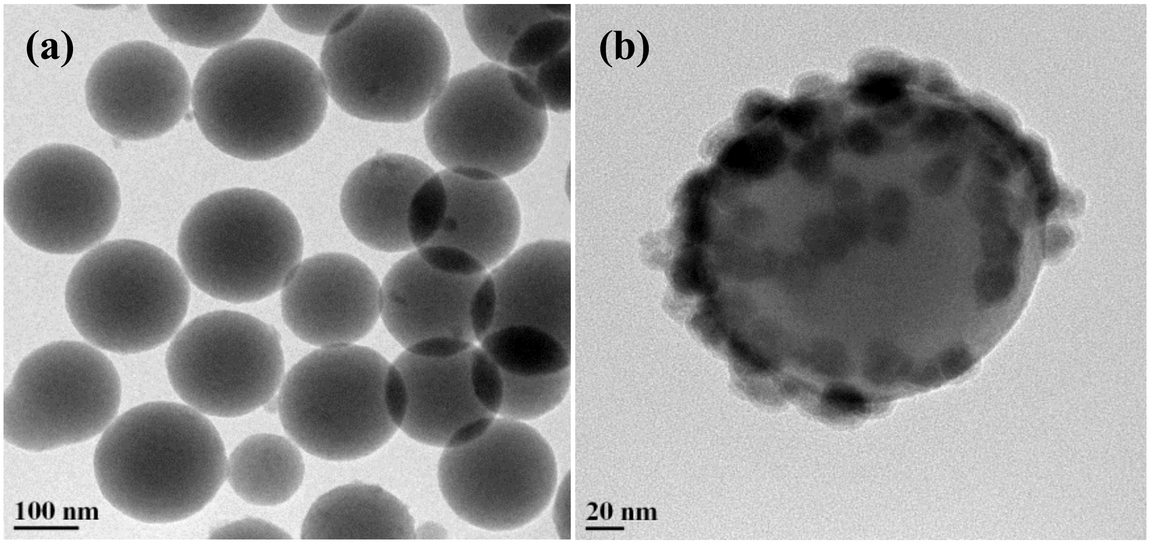

Figure 3.2- Bright field TEM micrograph of bare (a) NPS, (b) Co-B@NPS

MCM-41 silica particles mainly acquire irregular spherical shape with size in the range of 80–120 nm (fig. 3.3a). It is composed of regular hexagonal arrays of mesopores with uniform pore size as shown in the TEM image (Inset of fig. 3.3a). The distance that is repeated between the pores is measured around 4.5 nm, which is in perfect agreement with the spacing value (a_o) (table 3.1) obtained from the peak in the Small Angle X-ray Diffraction (SAXRD) pattern (discussed in the next section). The pore size and wall thickness were measured around 3.2–3.5 nm and 1–1.3 nm, respectively. These values are consistent to those obtained by SAXRD and Brunauer, Emmett and Teller (BET measurement (table 3.1).

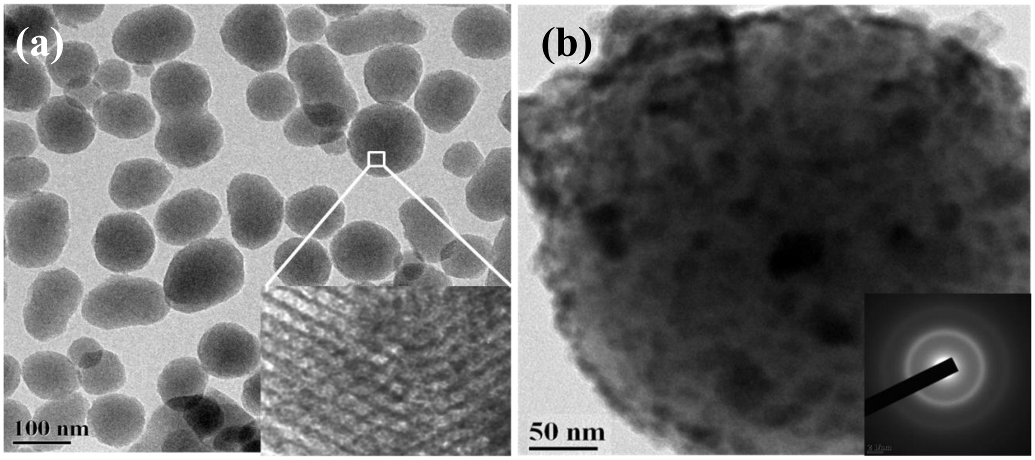

Figure 3.3- Bright field TEM micrograph of bare (a) MCM-41, (b) Co-B@MCM-41

Co-B particles supported on MCM-41 are much smaller in size with high degree of dispersion (fig. 3.3b). The particle size is distributed in range from 3 to 30 nm with maximum amount of particles (~ 90%) having size lower than 10 nm. Due to the irregular shape of particles and large thickness of the support, the determination of the exact particle size is hindered. However, a rough estimation indicates an average particle size of about ~8 nm which is larger than the pore sizes (in the range of 2-6 nm with average size of 3.5 nm) of MCM-41. This shows that most Co-B nanoparticles are located on the surface, with some portion of the particle anchored into the pores.

Crumpled paper like structure was observed for FSM-16 (fig 3.4a). TEM viewed down in the direction of the pore axis reveals a hexagonally ordered mesoporous structure with regular arrangement of pores of uniform size. The pores are seen to be arranged in the patches composed of regular rows on the silica sheet with the spacing of 4 nm between them. This value along with pore size (2.3–2.5 nm) and pore wall (1.2–1.4 nm) measured by TEM is in good agreement with that obtained by SAXRD and BET measurements (table 3.2 and table 3.3).

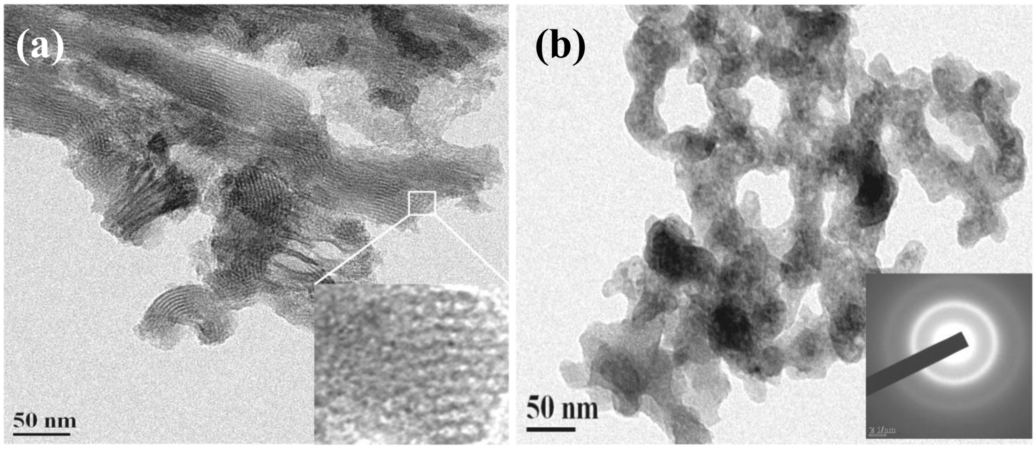

Figure 3.4- Bright field TEM micrograph of bare (a) FSM-16, (b) Co-B@FSM-16

In case of FSM-16 also, the Co-B particles are well dispersed on the surface having broad distribution of size in the range from 3 to 30 nm (fig 3.4b). However, most of them (90%) have size lower than 15 nm. Due to the irregular shape of particles and large thickness of the support, the determination of the exact particle size is hindered. Roughly calculated average particle size is about 12 nm. Particle size is greater than the pore size thus confirming that Co-B particles are located on the surface of with some portion of the particle anchored into the pores. SAED pattern for Co-B particles supported on MCM-41 and FSM-16 exhibits diffuse diffraction rings thereby confirming the amorphous nature of Co-B particle (further confirmed by XRD spectra in the next section).

SBA-15 shows well ordered hexagonal arrays of 2D mesoporous channels, especially along the direction of the pore axis (fig 3.5a) or in the direction perpendicular to the pore axis (fig 3.5c). However, the pores here are well distinct with bigger size (6.2 nm) and walls are much thicker (3.5 nm) than the MCM-41, SBA-15 (table 3.1 and 3.2).

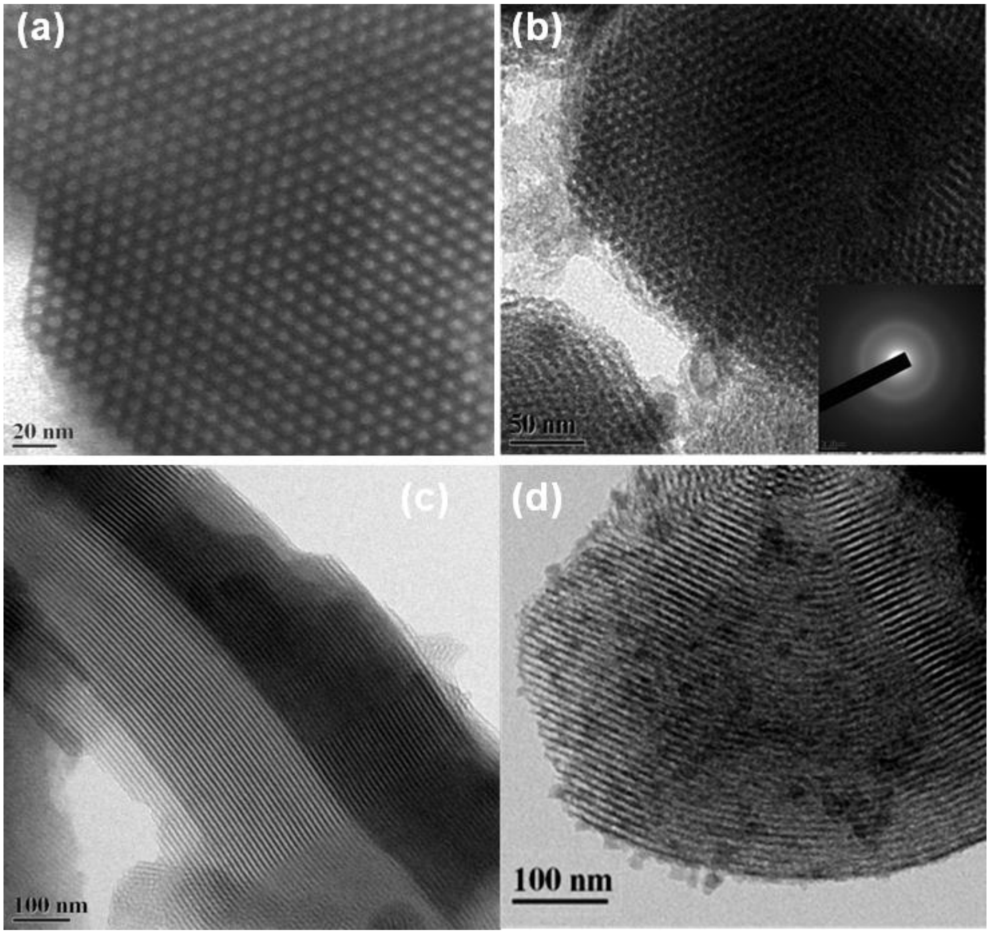

Figure 3.5- Bright field TEM micrographs of bare (a) and (c) SBA-15, (b) and (d) Co-B@SBA-15

Even though all the three MSPs have the similar pore structures, they accommodate Co-B particles in a quite different manner. As observed by the TEM micrographs, the Co-B particles are located on the outer surface of MCM-41 (fig 3.3b) and FSM-16 (fig 3.4b), while the Co-B catalyst particles are well placed inside the channel of the SBA-15 type silica (fig 3.5b). This was concluded on the basis that the porous structure of FSM-16 and MCM-41 is not visible, while for SBA-15, the hexagonal array structure is well maintained after Co-B loading. The Co-B particles are well confined in the pores of SBA-15 acquiring the size of pores (6 nm) (fig 3.5b). Along the channel, the size of Co-B slightly increases to around 10 nm (fig 3.5d).

SAED pattern for Co-B@SBA-15 (inset of fig. 3.5b) diffuse diffraction rings thereby confirming the amorphous nature of Co-B particle as observed in the XRD pattern. The morphological analysis clearly shows that the Co-B particles do not directly acquire the size of the support pores and depending on the texture of the mesopores the Co-B particles are positioned in or on the pores. The different morphologies obtained on different mesoporous silica are attributed to the impregnation–reduction process.

During impregnation, $CoCl_2$ solution fills most of the pores by capillary action and additionally it is adsorbed on the surface of the supports, but less as compared to NPSs. Generally, during the reduction process by $NaBH_4$, the Co-B particles are formed by release of H_2 gas. Thus, in case of SBA-15, due to the interconnected pore assembly H_2 can leave the interior of the SBA-15 easily. In FSM-16 and MCM-41, the pores are not interconnected and thus, in this case, H_2 can be released only from the pore face which is blocked by the Co-B particles. Thus, due to the pressure exerted by the H_2 gas, the Co-B particles are pushed out on the external surface of MCM-41 and FSM-16. The other possibility is that due to the limitation of the preparation method, Co-B particle size cannot be reduced lower than the size of mesopores of MCM-41 and FSM-16 to accommodate it. However, the average size of Co-B particles is around 10–12 nm for MCM-41 and FSM-16 silica with a size distribution from 3 to 30 nm.

In summary, when $CoCl_2$ in the pores is reduced by $NaBH_4$ solution, it forms Co-B particles with size as of the pores. For Co-B particles formed on the support surface the agglomeration of the particles is avoided as compared to the bare and Co-B @NSPs. High degree of dispersion of these nanoparticles is obtained due to the large number of nucleation sites in form of mesopores in the MCM-41 and FSM-16. Large pore size, more spacing between the two regular arrays of pore channels (table. 3.1 and 3.2), interconnectivity of the pores facilitated more confinement and dispersion of Co-B nano particles in the SBA-15 (fig. 3.5d) than the MCM-41 (fig. 3.3b) and FSM-16 (fig. 3.4b). Elemental analysis performed by EDS also confirms that mesopores permit high Co loading of 10~20 wt. % in the MSPs as compared to NSPs which accommodate only ~7 wt. % of Co.

The structural nature of the Co-B, MCM-41, FSM-16 and SBA-15 with and without support of Co-B and surface area, pore size and pore wall thick parameters of the MSPs are further studied by XRD, SAXRD and BET surface area measurements. The analysis was done to make solid understanding for the physic-chemical properties of the Co-B loading in the MSPs and effect on the hydrogen production enhancement.

3.3.2 Structural characterization

Wide angle X-Ray diffraction (XRD) pattern in wide-range for bare Co-B catalyst and Co-B@NPSs, MCM-41, FSM-16 and SBA-15 silica particles are reported in fig 3.6. The broad peak at around 2θ = 45° assigned to the amorphous state of Co-B alloy is observed for bare and Co-B@NPSs. On the contrary, no peak of Co-B is observed for the Co-B supported over all the three MSPs, thus indicating that the catalyst species were highly dispersed in the pores of the support material. The diffraction pattern clearly indicates short-range order and of Co-B alloy and these features are highly appropriate to enhance the catalytic activity [65].

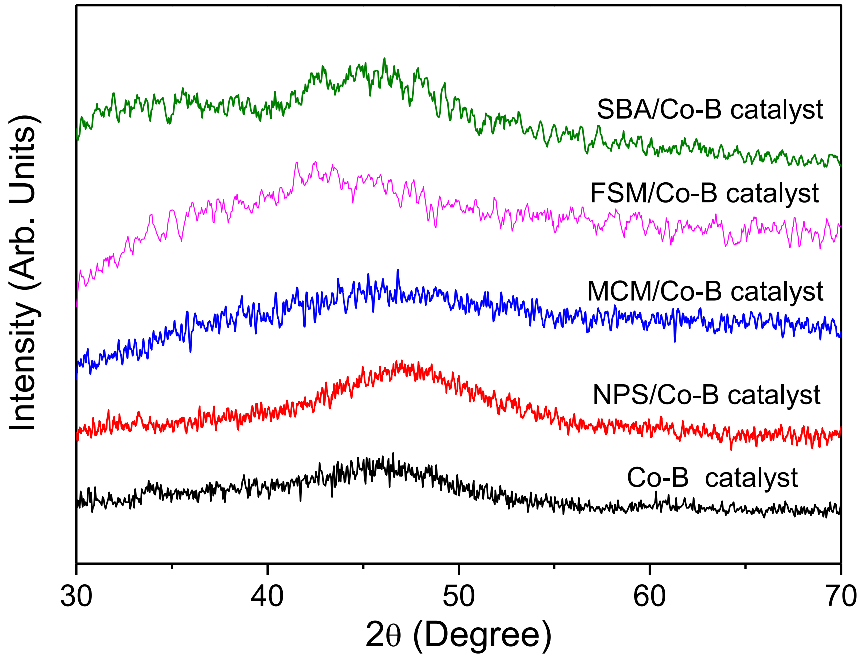

Figure 3.6- Wide-angle XRD pattern of bare Co-B powder, Co-B@ NPS, MCM-41, FSM-16, and SBA-15.

SAXRD patterns of NPSs, MCM-41, FSM-16 and SBA-15 is shown in fig.3.7. No evidence of any peak in the pattern of NPSs clearly indicates the absence of porosity. While a single peak is observed at 2θ values of 2.23° and 2.61° for MCM-41 and FSM-16, respectively, which is indexed as (100) reflection. On the other hand, SBA-15 diffraction peaks at 1.05°, 1.68°, and 1.92° which can be indexed as (100), (110) and (200) reflections associated with *p6mm* hexagonal symmetry [80]. All these peaks in the

SBA-15 are assigned to the regular array of hexagonal pore structure. The presence of higher order reflections demonstrate that SBA-15 silica acquire highly ordered hexagonal array of pores with uniform pore size as compared to MCM-41 and FSM-16, which is also confirmed by TEM results (as described above).

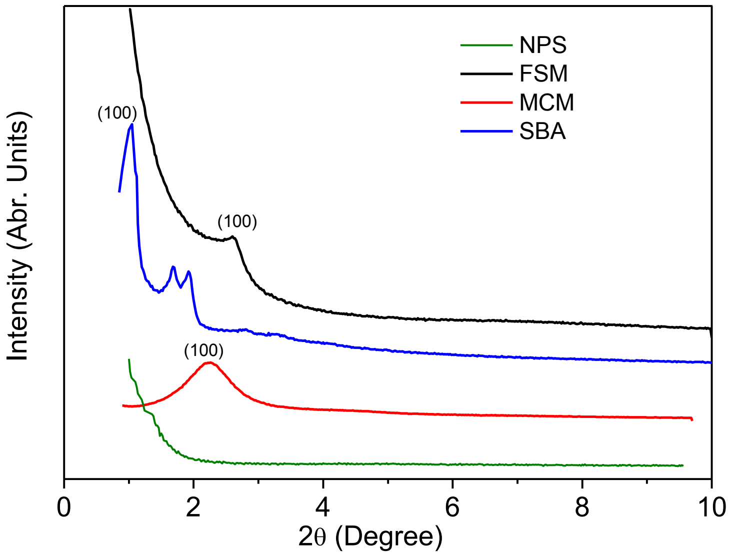

Figure 3.7- Small-angle XRD pattern of NPS, MCM-41, FSM-16 and SBA

The intensity of the characteristic reflection peaks decreases in XRD patterns after Co-B loading. Thus catalyst introduction probably plugs the pores and disturbs the local symmetry of the channel packing. In addition, X-ray mass absorption coefficient of cobalt is much higher than those of silicon and oxygen constituting the SiO_2 structure as reported in the literature [81].

3.3.3 Surface area measurements

Nitrogen adsorption–desorption isotherms of all the three MSPs before and after Co-B loading are presented in fig.3.8 (for MCM-41), fig. 3.9 (for FSM-16) and fig. 3.10 (for SBA-15) respectively. The inset of these figures shows the pore size distributions of the MSPs calculated using (Barret-Joyner-Halenda) BJH method.

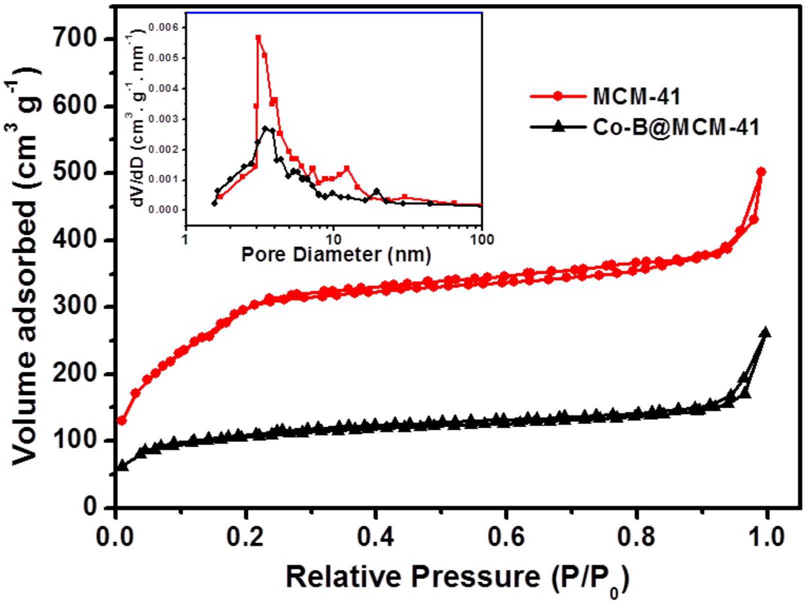

Figure 3.8- Nitrogen adsorption–desorption isotherms of MCM-41 before and after Co-B loading and Inset of the figure shows the pore size distribution curves

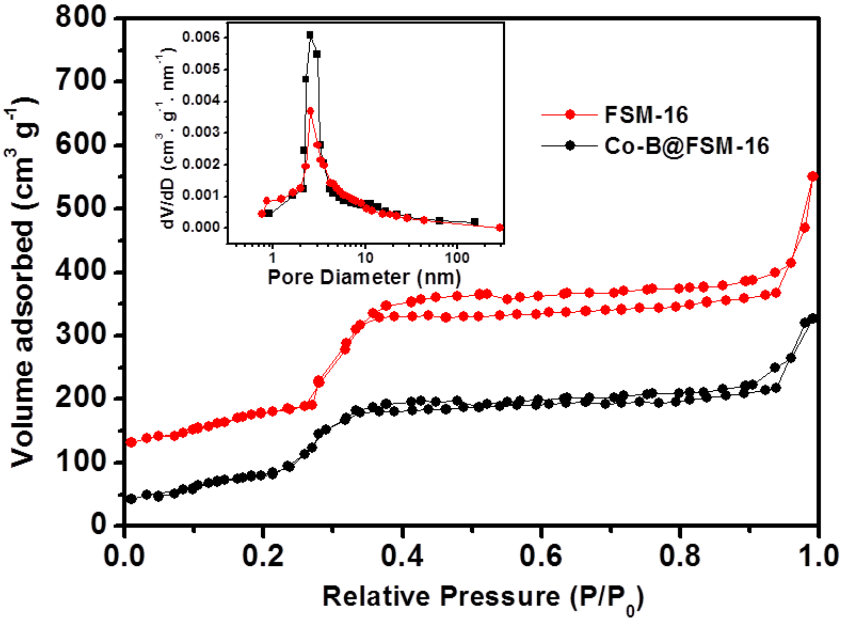

Figure 3.9- Nitrogen adsorption–desorption isotherms of FSM-16 before and after Co-B loading and Inset of the figure shows the pore size distribution curves

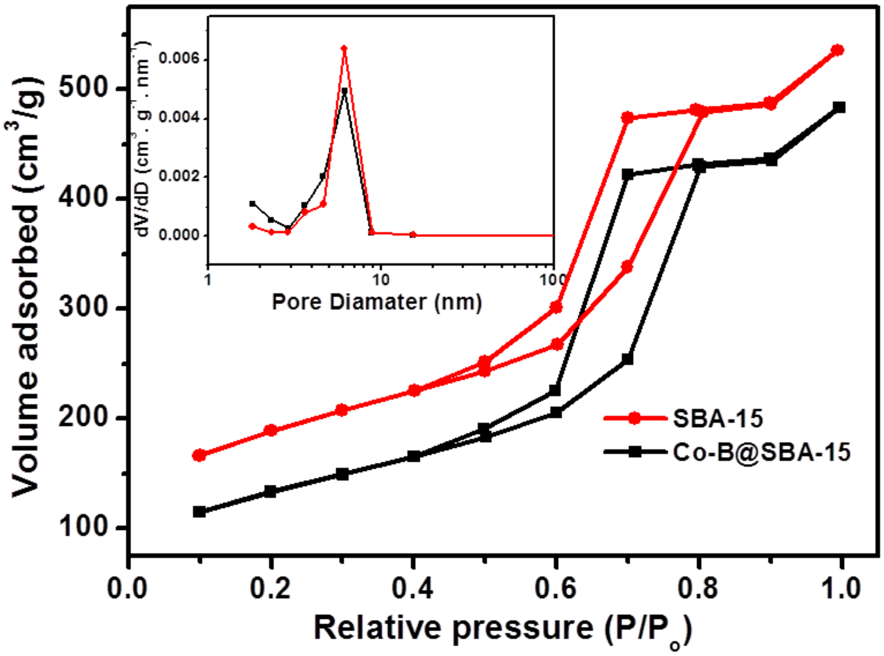

Figure 3.10- Nitrogen adsorption–desorption isotherms of SBA-15 before and after Co-B loading (Inset of the figure shows the pore size distribution curves)

All these MSPs (MCM-41: fig 3.8, FSM-16: fig3.9 and SBA-15: fig 3.10) showed type IV adsorption–desorption isotherm according to the IUPAC classification [82]. This kind of shape is typical characteristic of mesoporous material with tubular pores [83].

The type IV isotherm generally signals three regions. Initially at low P/P_0, the flat region is related to the monolayer formation on the silica outer surface and on the pore walls. As the P/P_0 increases, due to the spontaneous filling of the mesopores by the capillary condensation a certain step or inflection is observed in the volume of gas adsorbed. Later volume increases gradually with the P/P_0 and is mainly attributed to the multilayer adsorption on the outer surface of the particle. Finally, significant rise in N_2 adsorption at $P/P_0 > 0.9$ is caused by the filling of macropores formed by the gaps between the silica particles. The sharpness of the inflection indicates the uniformity of the mesopores size distribution. Thus, the fig. 3.9 and 3.10 shows that the mesopores of FSM-16 and SBA-15 attain narrow size distribution as compared to MCM-41 (fig. 3.8). The inflection region is extended in P/P_0 range from 0.05 to 0.30 (fig. 3.8) for MCM-41 with the pore size distribution in the range of 2–8 nm (inset of fig. 3.8).

Another important characteristic of the mesopores can be obtained from the shape of adsorption–desorption hysteresis loop of the isotherm which are correlated with the texture of the adsorbent. SBA-15 (fig. 3.10) showed H1 type hysteresis loop corresponding to ordered porous material with cylindrical pores open at both ends and interconnected pore structure [36]. H4 type hysteresis loop is observed for the FSM-16 (fig. 3.9) indicating the mixture of micro porous (pore size less than 2 nm) and mesoporous structure [82]. On the contrary, distinct hysteresis loop is not observed in case of MCM-41 (fig. 3.8).

The physic-chemical parameters such as BET surface area, average pore diameter, and pore volume obtained from the isotherms are summarized in table 3.2. Though the pore volume of all the MSPs is nearly same, the average pore size decreases in order of SBA-15 (6.1 nm) > MCM-41 (3.4 nm) > FSM-16 (2.5 nm).

Pore wall thickness (table 3.3) was calculated by subtracting the pore diameter from the spacing between the regular array of pores (a_o) (obtained from the formula {$a_o = 1.154 \times d_{100}$}, where d_{100} is estimated from the first peak in SAXRD (fig. 3.7). The wall thickness of SBA-15 is two times thicker than that of MCM-41 and FSM-16, thus showing the strength and the robustness of pore structure of SBA-15.

Table 3.1: Physico-chemical properties of Co-B NPs and the three different MSPs supports (MCM-41, FSM-16, and SBA-15) with and without Co-B catalyst loading

Samples	***BET surface area (m^2/g)***	***Pore Diameter (nm)***	***Pore Volume (cm^3/g)***
Co-B powder	20	--	--
NPS	31.5	--	--
Co-B@NPS	11	--	--
MCM-41	970	3.4	0.86
Co-B@MCM-41	335	3.1	0.35
FSM-16	958	2.52	0.85
CoB@FSM-16	630	2.50	0.62
SBA-15	627	6.15	0.83
CoB@SBA-15	455	6.14	0.64

Table 3.2: Pore wall thickness and spacing between the two regular arrays of pore channel of mesoporous silica supports calculated from the SAXRD and N_2 absorption-desorption isotherms.

Samples	***$d_{(100)}$ (nm)***	***a_o (nm)***	***Pore Wall Thickness(nm)***
MCM-41	4.03	4.65	1.25
FSM-16	3.38	3.91	1.40
SBA-15	8.40	9.70	3.55

The BET surface area of SBA-15 is lower than that of MCM-41 and FSM-16 type due to larger pore size and pore wall thickness (table 3.2). Incorporation of Co-B catalyst to

SBA-15 (fig. 3.10) did not influence the shape of the isotherm. In contrast, incorporation of Co-B into MCM-41(fig. 3.8) caused significant variation in the isotherms, where inflection characteristic completely disappeared. While in case of FSM-16 (fig. 3.9), the inflection is still present after loading Co-B but the sharpness of the step is decreased along with fading of hysteresis loop. The average pore diameter remains more or less intact for all the three mesoporous materials even after incorporation of Co-B (table 3.2). However, the pore volume and BET surface area decreases on Co-B loading with more prominent effect in MCM-41 as compared to SBA-15 and FSM-16 (table 3.2).

The above results clearly suggests that Co-B particles are located inside the pores of SBA-15 silica by keeping the pore structure intact while for MCM-41 Co-B particles either completely fill the pores or lie outside on the face of pores thus making the pores inaccessible to nitrogen. In case of FSM-16, the micro pores are completely blocked by the Co-B as indicated by the disappearance of the hysteresis loop.

3.3.4 Co-B supported over MCM-41, FSM-16 and SBA-15 for hydrolysis

Hydrogen generation yield was measured as a function of time as described in experimental techniques of the chapter 2. Hydrolysis of AB solution (0.025 M) in presence of Co-B catalyst loaded on MCM 41, FSM-16, SBA-15, NPSs, and bare Co-B powder at 298 K (fig. 3.11) was done. The amount of Co (10 mg) was kept same in all forms of catalyst during each experiment. Active nature of all the catalyst powders was confirmed by the fact that H_2 is instantaneously produced as soon as they come in contact with the AB solution. Among all the mesoporous materials, Co-B @SBA-15 type silica (15 min, fig. 3.11) was the fastest to complete the reaction: the time taken was two times lesser than that observed for Co-B@MCM-41 (29 min) and Co-B@FSM-16 (30 min) supported Co-B catalyst, while 5 times lesser than Co-B@NSPs (73 min) and bare Co-B catalyst (75 min). Co-B catalyst supported on the various MSPs was able to produce expected amount of H_2 ($H_2/NH_3BH_3 = 3.0$) by hydrolysis of AB. On the contrary, bare Co-B catalyst and that supported on NSPs were able to produce only ~85 % of H_2 yield ($H_2/NH_3BH_3 = 2.55$).

The H_2 generation yield values for the bare and Co-B @NPSs catalyst powders reported in fig. 3.12 were perfectly fitted by using a single exponential function [84] indicating that hydrolysis reaction is first order reaction (eq. 3.4) with respect to AB concentration.

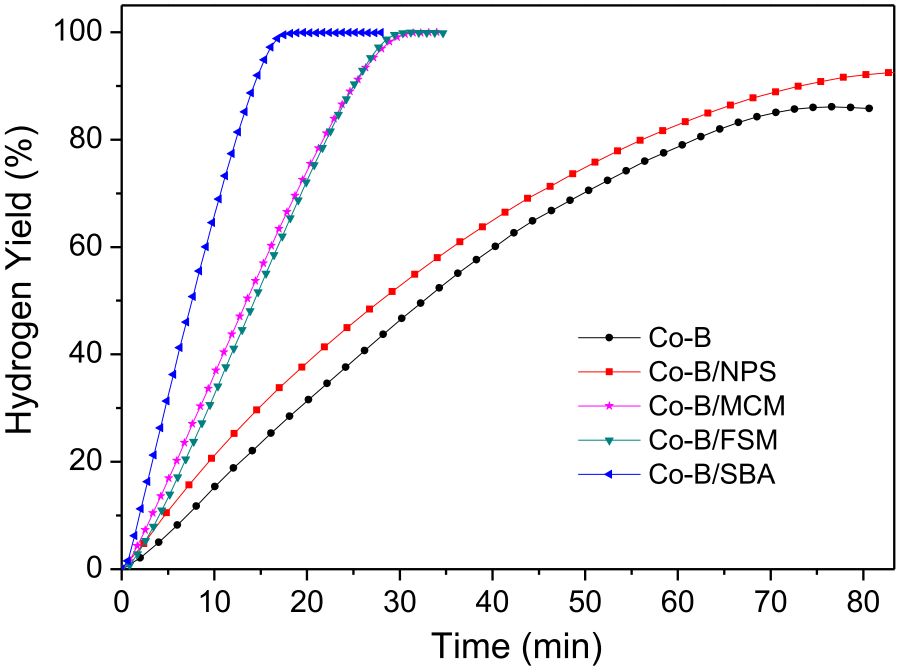

Figure 3.11- H_2 generation yield as a function of reaction time obtained by hydrolysis of AB (0.025 M) with bare Co-B catalyst and Co-B/NPS, MCM-41, FSM-16, SBA-15.

On the contrary, the H_2 generation data produced by the Co-B catalyst supported on the MSPs was fitted with a linear function thus proving zero order reaction (eq. 3.3) with respect to AB concentration. The maximum value of H_2 generation rate (R_{max}) (table 3.3) achieved by the Co-B@SBA-15, ~1900 ml/min/g Co-B metal, is about 5 times higher than that obtained with bare Co-B powder catalyst (~360 ml/min/g Co-B metal). The obtained H_2 generation rate value with SBA-15 supported Co-B catalyst is definitely better than that of Co-B nanospindles (1293 ml/min/g of catalyst) [85], and amorphous Co-B catalyst used under ultrasonic hydrolysis reaction (395 ml/min/g of catalyst)[86], and comparable to transition metal doped Co-B [67].

The kinetic models for NH_3BH_3 hydrolysis reaction are briefly described here below [87-89]. Zero order kinetic reaction is independent of any reactant concentration (eq. 3.3), and H_2 generation rate increases initially to a maximum value, and then decreases with time as the NH_3BH_3 concentration decreases this suggests the first order of the reaction kinetics (eq. 3.4).

$$-\frac{dC_{NH_3BH_3}}{dt} = r_0 C_{NH_3BH_3} = k_0 \qquad 3.3$$

Where $C_{NH_3BH_3}$ is the concentration of NH_3BH_3, r_0 is the rate of reaction, and k_0 is the reaction rate constant for zero order reaction

$$-\frac{dC_{NH_3BH_3}}{dt} = r_1 C_{NH_3BH_3} = k_1 . C_{NH_3BH_3} \qquad 3.4$$

Where $C_{NH_3BH_3}$the concentration of NH_3BH_3 is, r_1 is the rate of reaction, and k_1 is the reaction rate constant for first order reaction.

Since every mole of NH_3BH_3 produces 3 mol of H_2 (eq. 3.1), the rate of H_2 production is thus given for modified zero order reaction (eq. 3.5) and for first order reaction (eq. 3.6) as shown below:

$$\frac{d[H_2]}{dt} = 3k_0 \qquad 3.5$$

$$\frac{d[C_{NH_3BH_3}]}{dt} = 3k_1 . C_{NH_3BH_3} \qquad 3.6$$

By fitting the curve of H_2 production yield as a function of time by using eq. 3.5 or eq. 3.6 both reaction order and rate constant can be evaluated.

The table 3.3 clearly shows that the catalytic performance of Co-B@NPSs is almost similar to that of bare Co-B catalyst. This is attributed to the similar kind of morphology obtained for Co-B catalyst in both the cases.

Table 3.3 H_2 generation rate of bare Co-B, supported over NPSs and MSPs.

Samples	***H_2 generation rate (ml/min/g of Co-B)***
Co-B powder	~ 360
Co-B@NPSs	~ 450
Co-B@MCM-41	~ 1150
Co-B@FSM-16	~1200
Co-B@SBA-15	~1900

Co-B@SBA-15 showed the best catalytic activity, which is mainly attributed to the Co-B particle confinement in the mesopores. Due to the confinement, Co-B particles acquires the size of the pores (~6 nm) which is smaller than the size of Co-B particles supported over MCM-41 (~10 nm) and FSM-16 (~12 nm) silica. As observed from the TEM image (described below), the pore size of SBA-15 is highly uniform. Thus, the Co-B particles also acquire a very narrow size distribution, unlike MCM-41 and FSM-16 supported Co-B particles having size distribution in the range of 3–30 nm. The pores in SBA-15 are open from both ends with internal interconnectivity to provide easy passage for reactant and product solutions as well as for the produced H_2 gas. Confinement of Co-B particle in the pores also eliminates any possibility of agglomeration during the reaction course. This shows that not only the size of the pores but also its texturing affects the location, size and dispersion of the Co-B catalyst particle. The H_2 production rate obtained with the catalyst supported over MCM-41 and FSM-16 is same, mostly due to the similar size (~10 to 12 nm) and location of the Co-B particles on support surface anchored with the pores.

In the MSPs-supported catalyst, Co-B particles are much smaller in size (less than 10 nm) and well dispersed in the pores and on the surface, providing large number of under-coordinated Co active atoms for the interaction with the reactant to produce expected amount of H_2 with high generation rate. Zero order reaction (eq. 3.4) with respect to AB concentration is obtained with the Co-B supported-MSPs catalyst and it is attributed to the high available effective surface area that permits immediate H_2 generation through surface reaction. In addition, the H_2 generation rate is constant throughout the reaction course which can be explained by the fact that mesopores anchor the Co-B particle on the MSPs surface to avoid agglomeration during reaction. On the contrary, first order reaction (eq. 3.5) kinetics involving diffusion of BH_3^- on the catalyst is observed in the case of unsupported and the Co-B supported-NSPs.

Effect of AB solution temperature (Activation energy barrier): In order to confirm the effectiveness of Co-B@SBA-15, *activation energy barrier* was evaluated by varying AB solution temperature. The H_2 generation yield, as a function of time, was measured at different solution temperatures by hydrolysis of AB (0.025 M) solution using Co-B@MCM-41, FSM-16 and SBA-15 as reported in fig. 3.12.

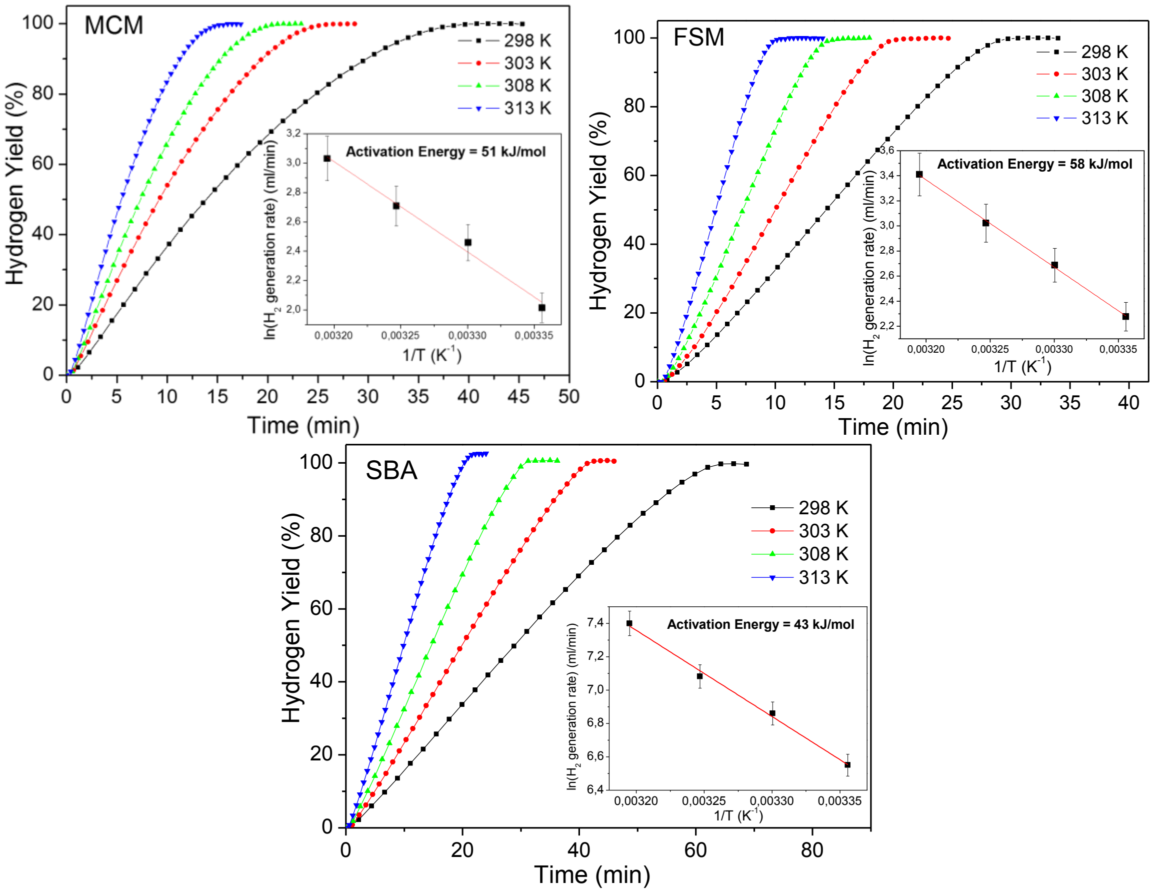

Figure 3.12- H_2 generation yield, as a function of reaction time, by hydrolysis of AB (0.025 M) at 4 different solution temperatures in the presence of Co-B@ MCM-41, FSM-16, and SBA-15. Inset shows the Arrhenius plot of the H_2 generation rates for each support.

The evaluation of activation energies (eq. 3.6) of rate limiting step is carried out from Arrhenius plot (insets of fig. 3.12) of the H_2 generation rate. Co-B@SBA-15 (43 ± 2 kJmol^{-1}) displays significantly lower energy barrier value in comparison to Co-B@MCM-41 (51 ± 3 kJmol^{-1}) and Co-B@FSM-16 (58 ± 3 kJmol^{-1}). The activation energy is calculated from Arrhenius plot as shown below:

$$lnk = lnk_0 - \frac{E_a}{RT} \qquad 3.6$$

Where k is the hydrogen generation rate and k_0 is the reaction rate constant, R is the gas constant (8.314Jmol^{-1}K^{-1}) and T (K) is the temperature of the NH_3BH_3 solution.

The favorable activation energy value again provides evidence that confinement of Co-B NPs in the pores with interconnectivity is well suited for the catalytic hydrolysis reaction. In general, the obtained activation energies are lower than that obtained with Rh (67 kJmol^{-1}) nanoclusters [90, 91], Ru/C(76 kJmol^{-1}) [92], K_2PtCl_6 (86 kJ mol^{-1}) [93], Ni-Ag (51.5 kJmol^{-1}) [94], Co/α-Al_2O_3 (62 kJmol^{-1}) [63], and comparable to Pd metal (44 kJmol^{-1}) [95], Co-Mo-B/Ni foam (44 kJmol^{-1}) [96], Ru (47 kJmol^{-1}) [97], and Co (0) nanoclusters (46 kJmol^{-1}) [63].

Annealing effect over Co-B@SBA-15 for H_2 production: Generally, bare Co-B particles agglomerate when heated at elevated temperatures in anaerobic conditions to form big crystallites [98]. This agglomeration initiates above the treatment temperature of 473 K and the related kinetics reach maximum at 773 K to form micron sized crystals of metallic Co [99]. This modification strongly hinders the catalytic activity of the Co-B catalyst. The heat treatment at 873 K completely deteriorates the catalytic efficiency of the Co-B catalyst [68].

The stability of Co-B particles confined in the pores and robustness of the pore structure was tested by heat treating the Co-B @SBA-15 at elevated temperatures (673, 773, and 873 K) in Ar atmosphere for 2 hours. The H_2 generation yield, as a function of time, obtained by hydrolysis of AB (0.025 M) solution using these heat treated Co-B@SBA-15 catalysts are reported in fig. 3.13.

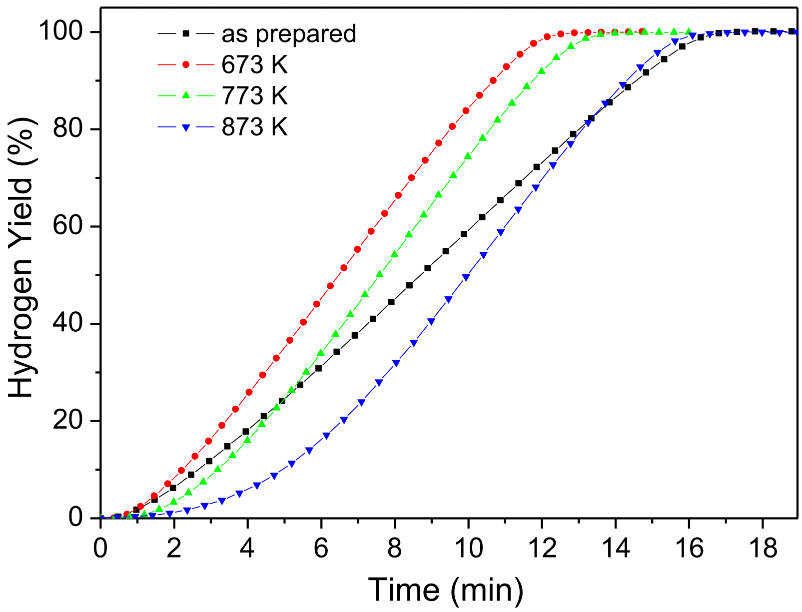

Figure 3.13- H_2 generation yield, as a function of reaction time, obtained by hydrolysis of AB (0.025 M) in the presence of untreated Co-B@SBA-15 and that heat treated in Ar atmosphere for 2 h at 673, 773, and 873 K.

It can be seen that H_2 generation rate increased when SBA-15 supported catalyst was treated at 673 K and only 10 minutes are required to complete the reaction. However, further increase in temperature to 773 K causes a slight decrement in the catalytic activity but it is still higher than the untreated catalyst. At 873 K, the initial induction time was increased slightly to 2 min but later, the H_2 generation rate increases and the reaction is completed in same time as that of untreated sample.

This result indicates that, while bare Co-B NPs get completely deteriorated by heat treating at 873 K, when confined in the pores of SBA-15 they maintain their catalytic activity similar to that of untreated catalyst.

Bare amorphous Co-B powder undergoes crystallization when heated above 473 K in anaerobic condition to form Co_2B phase which is very active phase for hydrolysis of chemical hydrides [94]. But above 673 K the agglomeration of Co-B particles increases to form big clusters which decompose to form metallic Co crystallites of micron size. This process, especially the decomposition of Co-B to Co metal crystallite, mainly due to the high degree of agglomeration, strongly decreases the catalytic activity of the Co-B alloy catalyst. For SBA-15 supported Co-B, the particles lie within the pores where Co_2B active phase is formed in the temperature range of 473–673 K which is responsible for the improvement of the catalytic performance. At higher temperatures the confinement of Co-B particles in the pores possibly avoids the agglomeration of the neighboring particles thus hindering the decomposition of Co_2B phase to form inactive metallic Co phase. Thus, even at 873 K, high H_2 generation rate is maintained with very slight induction time (2 min). This is clearly demonstrating the effect of the porous substrate physico-chemical properties on the enhancement of H_2 production from hydrolysis of AB. The confirmation of the supported Co-B NPs on the various MSPs was analyzed by SEM and TEM analysis.

3.4 Catalysts Hydrolysis of Sodium Borohydride ($NaBH_4$, SBH)

High catalytic activity of cobalt oxide (Co_3O_4) [100], Cobalt borate (Co-O-B [101], lithium cobalt oxide ($LiCoO_2$), Pt-Ru-CoO_2[102]) for $NaBH_4$ hydrolysis were studied. It was also reported that Co_3O_4 could hydrolyze the NH_3BH_3 and $NaBH_4$ [103], and effect of crystallinity and morphology of Co_3O_4 was reported by Pfeil. et al[104] with a maximum H_2 generation rate of about 1240 ml $min^{-}1g_{cat}^{-1}$. The superior H_2 generation rate obtained by Co_3O_4 was explained due to the formation of active Co-B phase from the Co_3O_4 precursor in presence of $NaBH_4$ or NH_3BH_3.

All the reported catalysts were in the form of powder phase, since exothermic nature of the hydrolysis reaction, agglomeration and deactivation of the catalysts was reported [71, 105]. Capping agents were employed to avoid these problems however the presence of capping agents resulted blocking of some of the active sites responsible for the catalytic activity [105]. Mostly the active Co-B phase was synthesized by reduction of cobalt chlorides by reduction process in presence of $NaBH_4$. Reduction of Co_3O_4 to the active Co-B phase does not need any chemical processes, just by simply reducing the Co_3O_4 to $NaBH_4$ solution results formation of the active Co-B phase.

The catalyst in the form nanoparticles (NPs) assembled coatings on a substrate has considered as most efficient and active way to avoid the mentioned drawbacks [106-109]. Catalyst in the form of NPs assembled coatings will serve as an environmentally friendly *"green catalyst"* for easy recovery, reuse, and could be a suitable tool for ON/OFF switch applications. Catalytic activity is mainly a surface phenomenon and forming a catalyst with high surface area and stability is a critical step for most of the applications. Among various synthesis techniques Pulsed laser deposition (PLD) has emerged as viable method for the production of NPs assembled coatings with desired properties [49, 108, 110]. By simply altering the deposition parameters in PLD can lead to tune the surface of the catalyst coating.

The present work is mainly focused on synthesis of inexpensive Co_3O_4 catalyst powders and NPs assembled coatings on glass substrates by using chemical and PLD technique respectively. The Co_3O_4 NPs assembled coatings were studied for hydrolysis of $NaBH_4$ and compared with bulk Co_3O_4 powder. The possible reasons for improved catalytic activity were discussed on the bases of the characterization results.

3.4.1 Structural and morphological analysis

Surface morphology obtained by SEM of Co_3O_4 coating deposited by PLD using laser fluence of $3 J/cm^2$ and Co_3O_4 powder catalyst (see chapter 2, section 2.2.3 and 2.3.4) obtained my co-precipitation method are reported in fig 3.14. The SEM image of Co_3O_4

powder (fig.3.14a) shows particle like morphology with irregular shape and estimated average particle size of about 45 nm along with very high degree of agglomeration. However, PLD deposited Co_3O_4 NPs assembled coating (fig. 3.14b) is composed of well arranged spherical particles with narrow size distribution (5-10nm) and the average particle size is less than 10 nm.

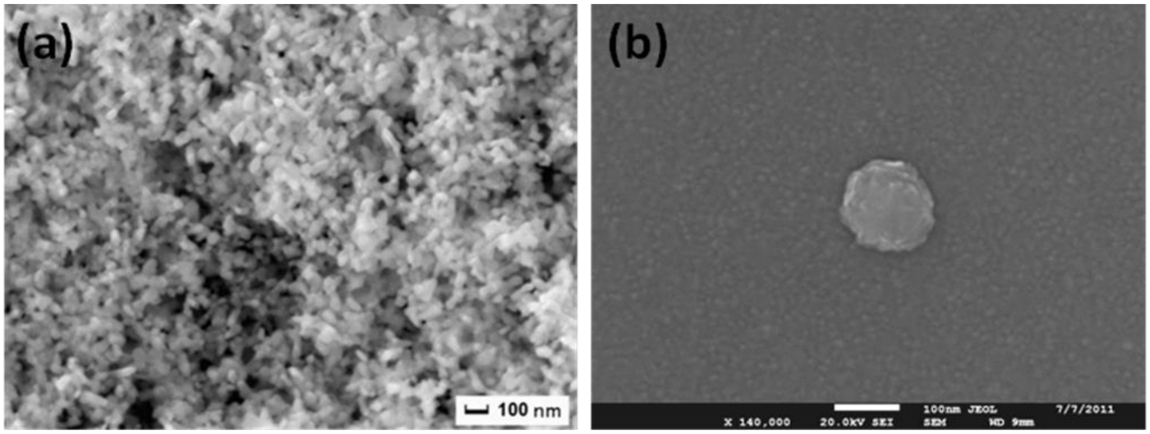

Figure 3.14- SEM micrographs of the Co_3O_4 catalyst in form of: (a) powder synthesized by chemical method, and (b) NPs assembled coating synthesized by PLD with laser fluence of $3J/cm^2$.

These particles are well distributed and densely arranged on the substrate surface with very low degree of agglomeration. These NPs are formed by high laser fluence induced phase explosion phenomena [29]. Here, the irradiated target material reaches temperature of ~0.9Tc (Tc is thermodynamic critical temperature) causing a very high homogeneous nucleation of vapor bubbles below the target surface. The target surface then makes a rapid transition from superheated liquid to a matrix of vapor and liquid nano-droplets, which leave the target surface. Later these liquid nano-droplets collide with oxygen atoms and oxidation occurs along with re-solidification during the flight to form solid NPs [33] onto the substrate. In case of big droplets, only a few top layers get oxidized during the flight to form core–shell structure with Co_3O_4 as shell and Co as core as confirmed by TEM analysis [33].

Figure 3.15 represents the HR-TEM image of the PLD deposited Co_3O_4 coating with size distribution analysis. From the fig. 3.15 it is clearly visible that the coating with the presence of small NPs of Co_3O_4, uniformly dispersed and having a mean diameter of about 6 nm with standard deviation value of 1.6 nm. The spacing between the lattice planes confirms that NPs are composed of Co_3O_4 phase.

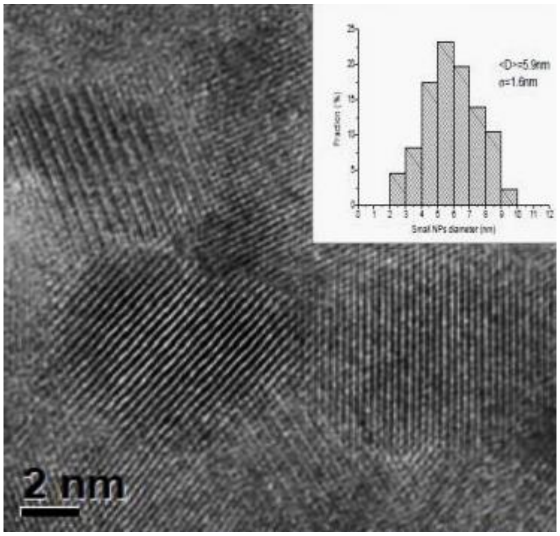

Figure 3.15- HR-TEM image of Co_3O_4 NPs assembled coating prepared by PLD with laser fluence of $3 J/cm^2$.

Raman spectra are presented in fig. 3.16 for the Co_3O_4 catalysts prepared by co-precipitation method and PLD. Powder Co_3O_4 catalyst (fig. 3.16b) clearly display the five Raman bands of A_{1g} at 693 cm^{-1}, E_g at 485 cm^{-1}, $3F_{2g}$ at 195, 522, and 620 cm^{-1}.

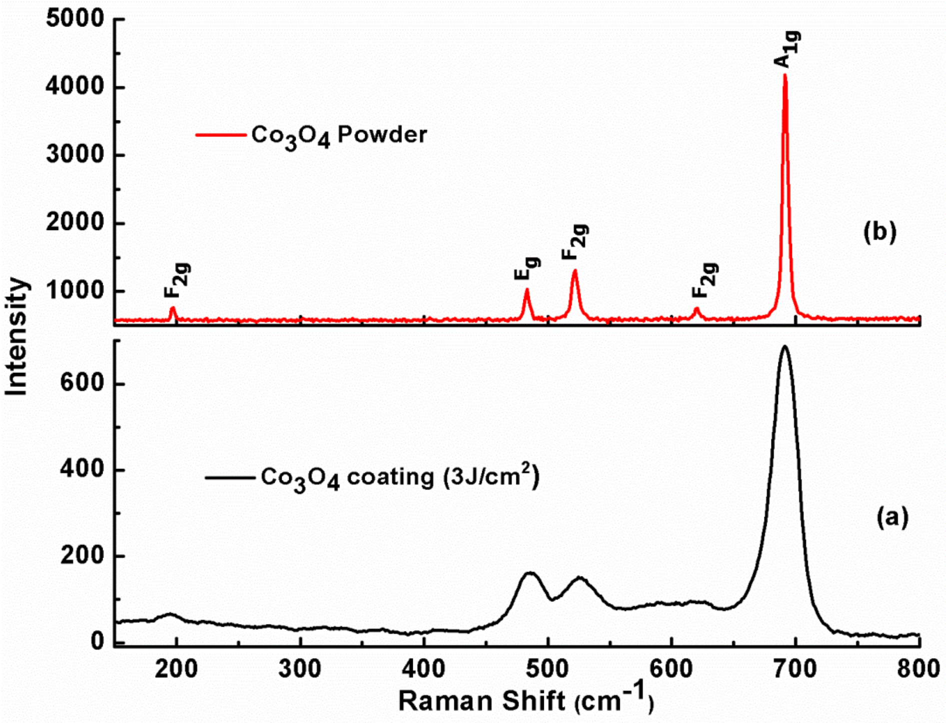

Figure 3.16- Raman spectra of (a) Co_3O_4 NPs assembled coating prepared by PLD with laser fluence of $3J/cm^2$, and (b) Co_3O_4 powder prepared by chemical method

The band at the position 693 cm^{-1} (A_{1g}) signals the octahedral site and the band at 195 cm^{-1} signals the tetrahedral site [34, 35]. This suggests complete crystallization of the Co_3O_4 phase. The physically deposited Co_3O_4 coating by PLD (fig. 3.16a) shows only three bands at 485, 525, and 694 cm^{-1} with low intensity and broad feature as compared to chemically prepared Co_3O_4 powder catalyst. This shows that Co_3O_4 coating prepared by PLD is nanocrystalline in nature, and due to small particle size only few Raman bands with broad nature are visible. No vibrational modes of any other impurities were detected in the Co_3O_4 coating and powder catalyst.

Figure 3.17 represents XRD patterns of the Co_3O_4 NPs assembled coating prepared by PLD and Co_3O_4 powder obtained by co-precipitation method. The XRD pattern of Co_3O_4

coating prepared by PLD (fig. 3.17a) with laser fluence 3J/cm^2 shows most intense diffraction peak at 36.5° with broad nature indicating prevailing nanocrystalline nature. The XRD pattern of Co_3O_4 powder (fig. 3.17b) prepared by co-precipitation method shows diffraction peaks at 19.0°, 31.2°, 36.5°, 38.4°, 44.8°, 55.6°, 59.0° and 65.2°, these are perfectly assigned to the spinel type cubic structure of Co_3O_4 with Fd3m space group [30]. These diffraction peaks correspond to the reflections (111), (200), (311), (222), (400), (422), (511) and (440), respectively. The crystallite size of the Co_3O_4 powder catalyst is around 45 nm as depicted from Scherrer equation from the most intense (311) peak. This value is in perfect agreement with that observed by SEM.

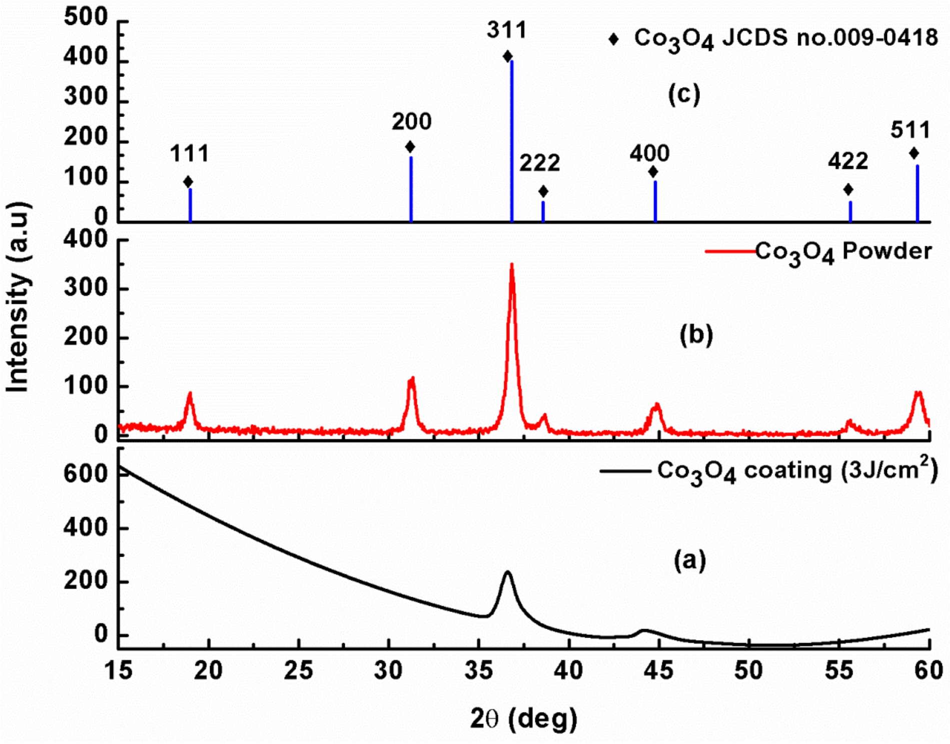

Figure 3.17- XRD patter of (a) Co_3O_4 NPs assembled coating prepared by PLD with laser fluence of 3J/cm^2, and (b) Co_3O_4 powder prepared by chemical method, and (c) represents slandered JCPDS pattern of Co_3O_4

Figure 3.18 represents the XPS spectra of the Co_3O_4 NPs assembled coating prepared by PLD with 3J/cm^2 and Co_3O_4 powder obtained by co-precipitation method. In Co_{2p} core level (fig. 3.18a), two distinct peaks assigned to cobalt oxide of $Co_{2p3/2}$ and $Co_{2p1/2}$ state are clearly visible in both powder and NPs assembled coating synthesized by chemical route and PLD respectively. The prominent peak of $Co_{2p3/2}$ level is de-convoluted into two peaks centered at 779.4 and 780.9eV attributed to Co^{3+}-$2p_{3/2}$ and Co^{2+}-$p_{3/2}$ configurations. This confirms the presence of Co_3O_4 spinel structure in both the samples. Shake-up peaks of Co_3O_4 phase are also observed at 789 eV and 804 eV.

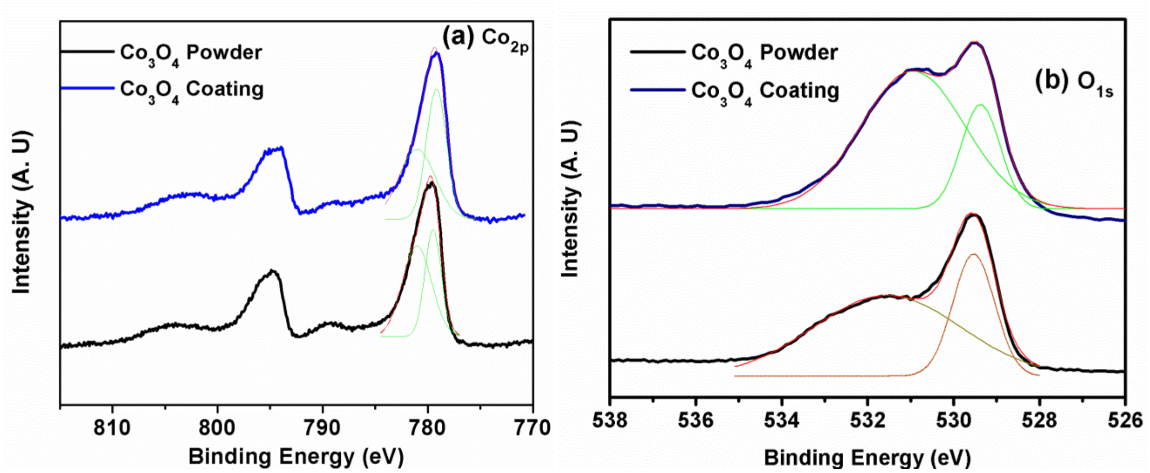

Figure 3.18- XPS spectra of: (a) Co_{2p} and (b) O_{1s} core levels of Co_3O_4 powder catalyst (black line) prepared by chemical method and NPs assembled coating (blue line) synthesized by PLD with laser fluence of 3J/cm^2

However, the amount of Co^{3+} is higher than Co^{2+} species for the NPs assembled coating as compared to chemically prepared powder where both the species are present in equal amount. In O_{1s} core level (fig. 3.18b), the peak at about 529.4 eV with a shoulder close to 531.5 eV corresponds to oxygen in the Co_3O_4 crystal lattice and to OH (hydroxyl) group attached to Co, respectively. These peak positions are in well agreement with that reported for Co_3O_4 network. The presence of hydroxyl group on the catalyst surface is due to our ex situ experimental conditions and its content is higher for film than powder.

3.4.2 Co_3O_4 NPs assembled coatings for hydrolysis

Prior to the hydrolysis measurements, the Co_3O_4 NPs assembled coatings deposited by PLD and Co_3O_4 powder prepared by chemical method were activated in presence of $NaBH_4$. In this process, catalysts were kept in the $NaBH_4$ aqueous solution (1M) for 15 min and later after removing form the solution all samples were washed with distilled water and ethanol several times before dying in vacuum condition.

For catalytic activity measurements, a solution of $NaBH_4$ (0.025 ± 0.001 M) (Sigma Aldrich) was prepared. Gas volumetric method (as described chapter 2, section 2.4) was used to measure H_2 volume generated by hydrolysis reaction. In the present experiment, 150 ml of the above $NaBH_4$ solution was used at the desired temperature and then catalyst was added to this solution. H_2 production rate was calculated by measuring the weight of the water displaced, which can be easily converted into cumulative H_2 production yield (%) and plotted against the reaction time.

Activated Co_3O_4 coating prepared by PLD was able to produce hydrogen instantaneously as soon as come in contact with the $NaBH_4$ solution as shown in fig. 3.19a, while the activated powder displayed small induction period to initiate hydrolysis reaction. However, the Co_3O_4 coating prepared by PLD exhibits much higher catalytic activity as compared to the Co_3O_4 powder and it is able to complete the reaction within 210 min while the Co_3O_4 powder catalyst was able to produce only 30 % of H_2.

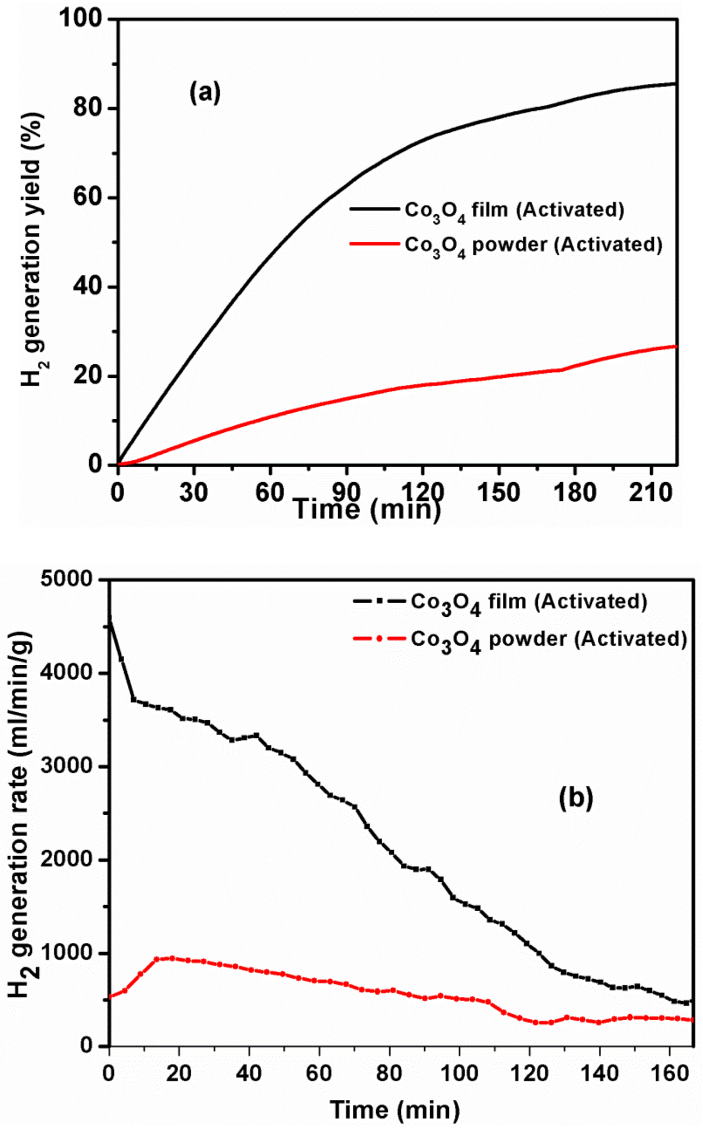

Figure 3.19- (a) Hydrogen yield measurements as function of reaction time of by the activated NPs assembled coating Co_3O_4 coating (black line) and Co_3O_4 powder (red line) prepared by PLD with laser fluence of 3J/cm^2, chemical method respectively, and (b) H_2 generation rate (ml/min/g$_{cat}$) between the activated NPs assembled Co_3O_4 coating (black line) and Co_3O_4 powder (red line).

A number of films synthesized by using the same parameters of PLD showed almost identical (±5%) hydrogen generation rate in all experiments, thus establishing the reproducibility of the Co_3O_4 coatings by PLD technique. During the reaction, the catalyst films were quite stable in terms of hydrogen production. The H_2 generation rate values of both the Co_3O_4 coating and powder with time are shown in the fig. 3.19b. Maximum H_2 generation rate obtained by PLD Co_3O_4 coating is 4840 ml min^{-1} g_{cat}^{-1}, which is 4.8 times higher than obtained by Co_3O_4 powder (1000 ml min^{-1} g_{cat}^{-1}). The generation rate with time as expected for a first order reaction (eq. 3.4) with respect to $NaBH_4$ concentration [26] which decreases with the reaction time. The H_2 generation rate reported here is incredibly higher than the reported values of other catalysts in the literature. Ru on IRA (378 $min^{-1}g_{cat}^{-1}$) [8], Ni–B (233 $min^{-1}g_{cat}^{-1}$) [36], Pt-$LiCoO_2$ (1387 $min^{-1}g_{cat}^{-1}$) [37]. Co_3O_4 nano foam powder with was able to produce 1240 ml min^{-1} g_{cat}^{-1} and 430 ml min^{-1} g_{cat}^{-1} for commercially available Co_3O_4 [22]. Co-B NPs assembled coatings prepared by PLD showed H_2 generation rate of about 3500 ml$min^{-1}g_{cat}^{-1}$[26].

The achieved high H_2 generation rate could be explained in terms of the existing surface morphology and importantly the NPs size distribution (5-10 nm) in coating (fig. 3.16 and fig. 3.21). NPs with small size and narrow size distribution provide high surface area. These oxides NPs transforms into active Co-B phase in presence of $NaBH_4$ for the NPs assembled coatings and they are thought to be highly active sites for the hydrolysis reaction. In case of the Co_3O_4 powder the active phase Co-B formation could be less favorable due to bigger particle size and due to the powder form the agglomeration of the catalyst NPs at the time of hydrolysis reaction was observed. So, thereby it is clearly revealing that catalyst NPs as coating form offers a finest solution in increasing the activity and stability.

Further H_2 generation rate was measured for the coatings deposited by PLD using different laser fluencies (5-13J/cm^2) to study the effect of surface features such as particle size and number density of the particles. The H_2 generation profiles for the Co_3O_4 coatings obtained with various laser fluences are shown in fig. 3.20a.

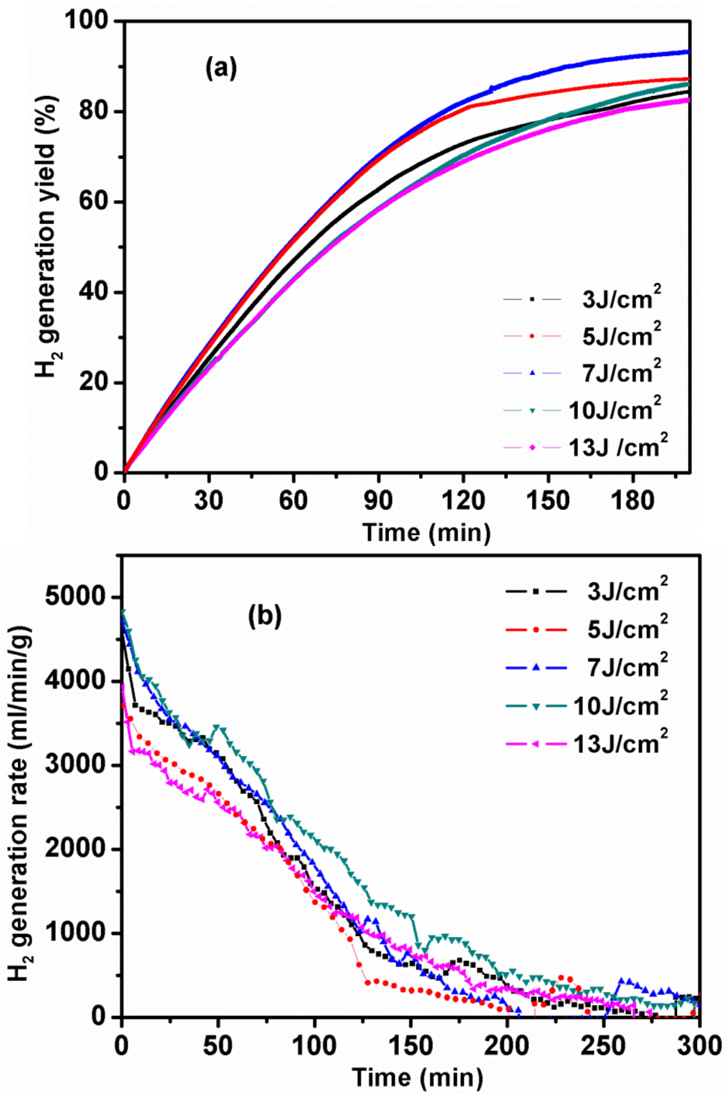

Figure 3.20- (a) Hydrogen generation yield as a function of reaction time by hydrolysis of NH_3BH_3 (0.025 M) solution, with activated NPs assembled Co_3O_4 coatings prepared with different laser fluencies, and (b) H_2 generation rate (ml/[min/g_{cat}) of the activated NPs assembled Co_3O_4 coatings prepared with different laser fluencies

The coatings deposited with 5 and 7J/cm^2 fluences [26] showed little improvement in the H_2 generation, but at higher laser fluencies of 10 and 13J/cm^2 the H_2 generation rate is similar to that observed with for the Co_3O_4 coating prepared with 3J/cm^2 laser fluence. The observed increments in H_2 generation rates are small with increasing laser fluence and on average within the error range (±5%) all the coatings are with similar H_2 generation rate. The corresponding H_2 generation rate profiles for the Co_3O_4 coatings prepared with different laser fluencies are shown in fig.320b. To understand underlying reasons for similar H_2 generation values for all the PLD deposited Co_3O_4 coatings SEM and micro-raman analysis was carried out.

From the SEM images (fig. 3.21) it is clearly observed that with increasing laser fluences there is not major change in size of NPs was observed and it was identified that for all the coatings the particle size distribution is around 5-10 nm. However, increment in particle packing density was observed with increasing laser fluence (fig.3.21a-fig.21d). With increase in laser fluence, appearance of big droplets on the surface of the coatings was also observed which could be possibly explained by the target stress confinement [28]. From the micro-raman measurements (fig. 3.22) no appreciable changes were seen in the Raman bands for the coatings deposited with laser fluences from 5 to 13J/cm^2. This is clearly indicating that the surface morphology, particle size distribution and Co_3O_4 phase in all the coatings are with more or less same analogous characteristics. These characteristics reflect for the same H_2 generation rate for all the coatings prepared by PLD. In future a specific work is being considered to gain more insights into the PLD deposited Co_3O_4 coatings.

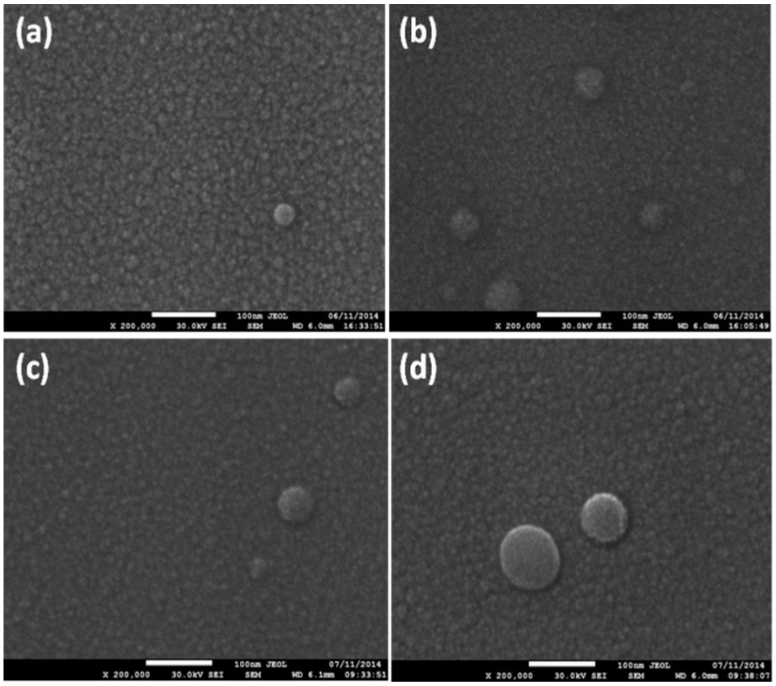

Figure 3.21- SEM images of NPs assembled Co_3O_4 coatings prepared by PLD with laser fluences of (a) $5J/cm^2$, (b) $7J/cm^2$, (c) $10J/cm^2$, and (d) $13J/cm^2$

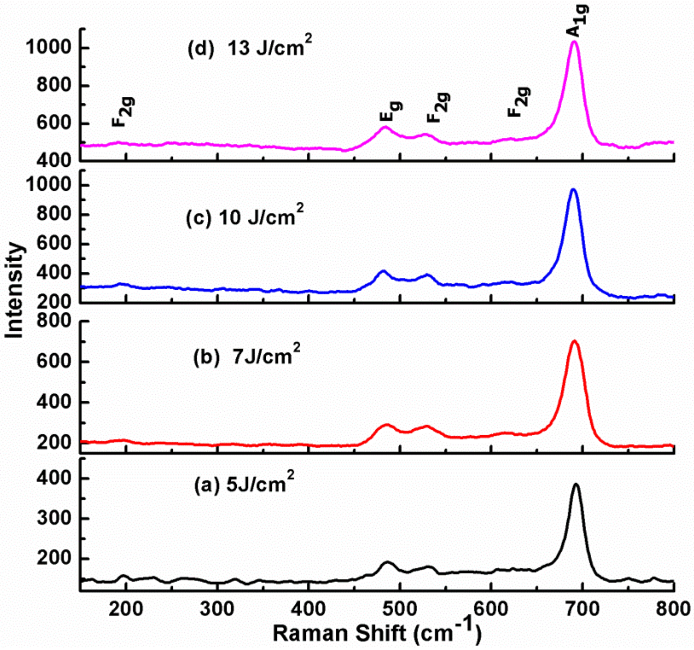

Figure 3.22- Raman spectra of NPs assembled Co_3O_4 coatings prepared by PLD with laser fluencies of (a) 5 J/cm^2, (b) 7 J/cm^2, (c) 10 J/cm^2, and (d) 13 J/cm^2

3.5 Conclusions

The H_2 production by hydrolysis of AB was studied by using Co-B NPs catalyst supported by impregnation–reduction method over the three kinds of MSPs (MCM-41, FSM-16, and SBA-15) of different pore size and texture. XRD data, TEM images and N_2 adsorption–desorption isotherm revealed the structural properties, size, dispersion degree, and location of Co-B NPs, and are affected by the pore texturing of the support. Co-B@SBA-15 silica was found to be most active catalyst that produces the expected amount of H_2 gas (1900 ml/min/g of Co-B catalyst), a value that is higher than that measured with Co-B@MCM-41 (~1150 ml/min/g of Co-B catalyst) and Co-B@FSM-16 (~1200 ml/min/g of Co-B catalyst). The higher efficiency of Co-B@SBA-15 is explained on the basis of the geometrical confinement of Co-B particles within the pores with the Co-B NPs have average size of about 6 nm and uniform size distribution while exhibiting higher degree of dispersion. The effective activation energy by Co-B@SBA-15 results lower than that established with Co-B@MCM-41 and Co-B@FSM-16. Finally, the thicker pore walls of SBA-15 avoids agglomeration of the Co-B NPs thus providing high stability at elevated temperatures (873 K) as opposed to what occurs with bare Co-B NPs catalyst.

Co_3O_4 NPs assembled coatings on a glass substrate were deposited using PLD by taking an advantage of phase explosion process. These coatings were prepared using different laser fluencies (3-13 J/cm^2) in order to tune the size of the NPs. Further the coatings were chemically reduced in $NaBH_4$ solution to obtain active Co-B alloy and then tested for the hydrolysis of $NaBH_4$. The activity measured by using the activated NPs assembled coating (H_2 generation rate 4800ml min^{-1}g$_{cat}^{-1}$) was significantly higher than activated powder Co_3O_4 catalyst (1000 ml min^{-1}g$_{cat}^{-1}$). The achieved high H_2 generation rate could be explained in terms of the existing surface morphology and importantly the NPs size distribution (5-10 nm) in coating and NPs with small size and narrow size distribution provide high surface area. These oxide NPs transform into active Co-B phase in presence of $NaBH_4$ for the NPs assembled coatings prepared by PLD and they are thought to be highly active sites for the hydrolysis reaction. In case of the Co_3O_4 powder the active Co-B phase formation could be less favorable due to bigger particle size and also agglomeration of the powder catalyst during hydrolysis.

Chapter 4:

Methylene Blue Dye degradation by Nano Particles Assembled Co_3O_4 coatings and 3-D hierarchical urchin like Co_3O_4 coatings

"Man is a complex thing: He makes desert bloom and- lakes die"

4.1 Introduction

4.1.1 Water pollution

The growth of the world's population and industry has increased the demand for water supply. At the same time the domestic use and industrial activity all over the world produces large amount of wastewater which leads to a high pollution risk to society. Water activities:

- Water can dissolve many chemicals.
- Water can leach out toxic materials.
- Water can transport pesticides, fungicides.
- Water takes mud with all its materials.
- Water can erode creek and river beds.

Water pollution today is a big issue. The cause of water pollution is vast and the penalty to the life on the earth is uncountable.

4.1.2 Evolution of dyes and consequences

Since the dawn of civilization, humans have been fascinated by color. In the primitive era, humans explored the natural resources of dyes available in flora and fauna for the coloration of textile fibers, marking the beginning of colorful life style and what followed next was the invention of the first synthetic dye Mauve (Mauveine) by Perkin in

1856[111]. This event created renaissance and is often associated with the pioneering times of the British chemical industry. As a consequence of all the developments, at present, there are more than 100,000 dyes available commercially (of which azo dyes represent about 70% on weight basis), and over 1 million tons dyes are produced per year, of which 50% are textile dyes[112]. In India alone, dyestuff industry produces around 60,000 metric tons of dyes, which is approximately 6.6% of total colorants used worldwide. The largest consumer of the dyes is the textile industry accounting for two third of the total production of dyes[113]

Among them, textile dyes, being constituents of the wastewaters from textile, pharmaceutical, food-stuff, cosmetic, paper, leather industries, etc., should be outlined. Most of the dyes cause water colorization at very low concentrations (even at 1mgL^{-1}), and as a result, their uncontrolled discharge in the natural water resources creates serious ecological problems. In addition, the textile dyes negatively affect the development of aqueous organisms as well as the photosynthesis activity of the marine flora [114]. Their high chemical and photo resistance creates potential risk of bioaccumulation for human health through the food chain transport. For those reasons, the treatment of wastewaters containing dyes prior their disposal in the water resources is obligatory, but at the same time a complicated process.

4.1.3 Technical solutions to neutralize the dyes

A wide range of physical, chemical and biological methods[115] have been developed for the purification of wastewater containing dyes. Adsorption is regarded as one of the most effective and relatively low-cost process, which has found practical application for removal of textile dyes from wastewaters. Active carbon [116, 117], clays [118-120], bio-sorbents [121], zeolites[122], and many others[113, 123] adsorbents are used for water treatment. However, it should be noted that adsorption methods lead only to the accumulation of the dyes on the adsorbents surfaces, not their neutralization, which in turn requires their further degradation to non-toxic products by means of effective degradation methods. Chemical oxidation methods using chlorine, hydrogen and ozone as oxidants can overcome these disadvantages. However, the chemical methods do not result in the complete mineralization of the organic pollutants[124]. Catalytic wet air oxidation processes with the usage of air or pure oxygen as oxidants have been used for removal of dissolved toxic organic pollutants from wastewaters. However, high pressures (20–200 bar) and temperatures (200– 320 ^oC) are needed, thus increasing the treatment cost [125]. An effective and economically feasible process for the destruction of a variety of hazardous pollutants in wastewater is based on *heterogeneous photocatalytic reactions* providing complete oxidation. Using suitable catalytic systems and reaction conditions, a high selectivity towards environmentally harmless end products (such as CO_2, H_2O, etc) can be achieved at mild conditions (room temperature and atmospheric pressure).

4.2 Heterogeneous photocatalysis (HPC)

Oxidation is defined as the transfer of one or more electrons from an electron donor (reductant) to an electron acceptor (oxidant), which has a higher affinity for electrons. These electron transfers result in the chemical transformation of both the oxidant and the reductant, in some cases producing chemical species with an odd number of valence electrons. These species, known as radicals, tend to be highly unstable and, therefore, highly reactive because one of their electrons is unpaired. Oxidation reactions that produce radicals tend to be followed by additional oxidation reactions between the radical oxidants and other reactants (both organic and inorganic) until thermodynamically stable oxidation products are formed. The ability of an oxidant to initiate chemical reactions is measured in terms of its oxidation potential. The most powerful oxidants are fluorine, hydroxyl radicals ($OH^{\bullet}$), ozone, and chlorine with oxidation potentials of 2.85, 2.70, 2.07 and 1.49V, respectively [126, 127]. The end products of complete oxidation (i.e., mineralization) of organic compounds such as dyes are generally carbon dioxide (CO_2) and water (H_2O) as shown in fig 4.1. The process which involves the generation of highly active radicals or species ($OH^{\bullet}$) is termed as advanced oxidation process (AOP) [127].

Heterogeneous photocatalysis (HPC) is a discipline which includes a large variety of reactions: mild or total oxidations of reactants, dehydrogenation, hydrogen transfer, metal deposition, *water detoxification*, gaseous pollutants removal, etc.

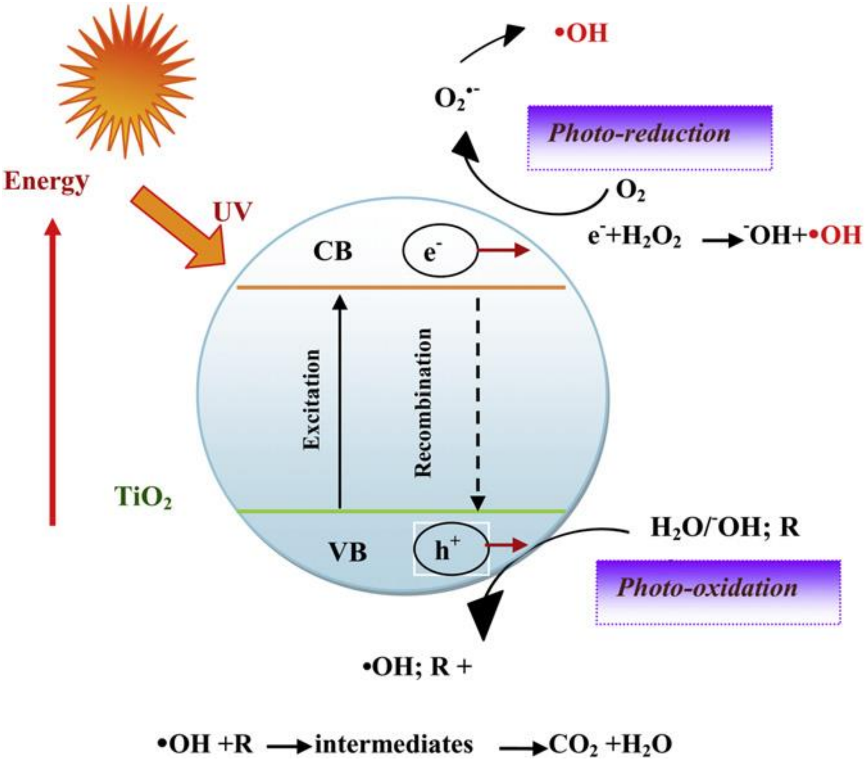

Figure 4.1- Schematic diagram illustrating the principle of heterogeneous photocatalysis [126].

HPC can be carried out in various media: gas phase, pure organic liquid phases or aqueous solutions in presence of a solid catalyst as powder form or an immobilized coating form.

As for heterogeneous catalysis, the overall process can be decomposed into five independent steps:

1. Transfer of the reactants in the fluid phase to the surface
2. Adsorption of the reactants
3. Reaction in the adsorbed phase
4. Desorption of the product(s)
5. Removal of the products from the interface region

The highly active $OH^{\bullet}$ generation in the AOP technology occurs by processes such as direct photolysis of H_2O_2, photo-excitation of TiO_2 and *Photo-Fenton reaction* in presence of H_2O_2 with metal cations [128, 129]. However, the first two methods require high intensity UV light, while the Photo-Fenton reaction proceeds by absorption of visible light hence showing significantly higher efficiency. Photo-Fenton reaction is very complex type of photocatalytic reaction which employs a mixture of H_2O_2 and ferrous ions (Fe^{2+} and Fe^{3+}) in acidic medium to generate the $OH^{\bullet}$ in presence of light [130]. Due to the requirement of acidic medium with low pH (pH 3) the process results in large sludge residues. Other transition metal ions like Co^{2+} ions are found to be active even in neutral pH for generating hydroxyl radicals via Photo-Fenton process and this is a clear advantage over Fe^{2+} [131].

Among various metal oxides, the cobalt oxide (Co_3O_4) based materials are of great interest as a Photo-Fenton catalyst due to their low cost, natural abundance, operating in visible light region and most importantly works at neutral pH to efficiently degrade the organic compounds [110, 129]. *Homogeneous catalyst* in form of cobalt salt solution along with an oxidant is generally used [45] . However, during homogeneous reaction the dissolved cobalt in the water can create further health concerns such as asthma, pneumonia and other lung problems and has been recognized as a priority pollutant in water with the highest allowable concentration of 1 mg L^{-1} in the potable water. It is anticipated to decrease the use of dissolved Co^{2+} by developing *heterogeneous catalysts*.

In heterogeneous route of this reaction, spinel Co_3O_4 containing Co^{2+} and Co^{3+} ions, has been used in AOP as photocatalyst for dye degradation through photo-Fenton reaction. Co_3O_4 [132](nanoparticles, nanorods, nanowires, etc.) displays outstanding activity and selectivity during the catalytic processes as compared to the corresponding bulk counterpart. The enhanced performance is mainly due to their large surface-to-volume atomic number ratio, size- and shape-dependent properties, and high concentration of low-coordinated active surface sites [133, 134]. In past, Co_3O_4 nanoparticles (NPs) have been synthesized primarily in powder form for the catalysis reactions. However, in this case the major drawbacks of the catalyst are the separation after catalytic reaction, NPs aggregation, and inability to use continuous flow processes. The separation of powder NPs catalyst from the reaction solution is so difficult that even by centrifugation these particles remain in the solution in form of colloids. Also, an excessive amount of cobalt leaching as high as 0.73 mg L^{-1} was still observed in such systems[135].

To enhance the catalytic performance and reduce cobalt leaching in Co_3O_4, it was immobilized on various metal oxide supports such as TiO_2, SiO_2, MgO, zeolite, activated carbon and carbon aerogel. It was also reported that mixed metal oxide as $CoFe_2O_4$ was able to reduce the leaching of cobalt [135]. Development of a catalyst with desirable morphology, dimensions and stability is becoming more interesting and challenging owing to their improved catalytic activity and increasing applications in various fields[110]. Thus, Co_3O_4 NPs deposited on suitable substrates as fully immobilized photo catalyst (IPC) on glass substrates are the best solution as green catalyst.

IPC in the form of coating with desired properties supported over substrate is of great interest in avoiding the above mentioned problems with cobalt. There are many methods by which IPC can be produced like electron-beam deposition (EBD), atomic layer deposition (ALD), plasma-enhanced chemical vapor deposition (PECVD), and sol–gel method by dip coating [45, 136-140]. Among the various techniques Pulsed Laser Deposition (PLD) technique has gained more attention in the last decade as a viable means of producing high-quality and highly stable coatings [107]. It is ideally suited for the deposition of wide variety of materials in minute amounts on various substrates and laser process allows the production of NPs with desired morphology with particle size as small as 10 nm in the form of NPs-assembled coatings by just tuning the experimental parameters with high stability due to the high energetic processes involved in the coating formation[141].

4.3 Co_3O_4 nano structures for Photocatalysis

The aim of the current section involves the study of NPs assembled coatings of Co_3O_4 catalyst synthesized by PLD (as in chapter 2, section 2.3.4) at various laser fluencies for photo catalysis. The effect of size distribution of NPs (effect of laser fluence) was studied by examining the degradation of Methylene blue (MB) dye in presence of photo-Fenton reaction.

4.3.1 Structural and Morphological analysis

To understand the obtained catalytic activity of the Co_3O_4 coatings, analysis was done in terms of morphological and structural variations of NPs with change in laser fluence. SEM images of the Co_3O_4 NPs assembled coatings prepared at different laser fluences (3, 5, and 7J/cm^2) are shown in fig 4.2. The surface of the Co_3O_4 coating deposited at 3J/cm^2 is composed of well circular shaped NPs with an average size of 10 nm and narrow size distribution (fig 4.3b). These particles are well distributed and densely arranged on the substrate surface with a very low degree of agglomeration (fig 4.2a).

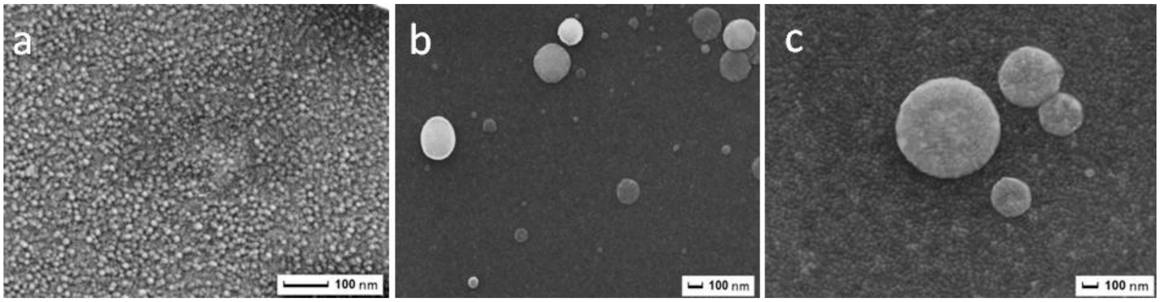

Figure 4.2- SEM micrographs of Co_3O_4 NPs assembled coatings prepared by PLD at substrate temperature of 150 °C with different laser fluences (a) 3J/cm^2, (b) 5J/cm^2, and (c) 7J/cm^2.

But, with increasing the laser fluence, particle size of the Co_3O_4 (above ~ 30nm) increases with the occurrence of big droplets with size in the range of 200-500 nm as seen in the fig 4.2b and c. No major differences in morphology were observed for the coatings with higher laser fluence of 5 and 7J/cm^2. The NPs are formed by high laser fluence induced phase explosion phenomena [49]. Here, the irradiated material target reaches to a temperature of ~ $0.9T_c$ (T_c is critical temperature) causing a very high homogeneous nucleation of vapor bubbles below the target surface. The target surface then makes a rapid transition from superheated liquid to a matrix of vapor and liquid nano-droplets, which leave the target surface. Later these liquid nano-droplets collide with oxygen atoms and oxidation occurs along with re-solidification during the flight to form solid NPs onto the substrate. In case of big droplets, only a few top layers get oxidized during the flight to form core-shell structure with Co_3O_4 as shell and Co as core, and these feature were confirmed by TEM analysis [142]. At high laser fluencies (small laser beam spot) the number of NPs decreases, while large droplets formation increases. This could be possibly explained by the target stress confinement at these high laser fluencies [143, 144].

To understand the phase of the Co_3O_4 coatings HR-TEM and micro-raman analysis was carried out. Fig 4.3a and b shows the HR-TEM image and particle size distribution respectively, of the Co_3O_4 NPs prepared by using fluence of 3 J/cm^2. It reveals the presence of small NPs of Co_3O_4, uniformly dispersed and having a mean diameter of about 6 nm with standard deviation values of 1.5 nm. The spacing between the lattice planes confirms that NPs are composed of Co_3O_4 phase only.

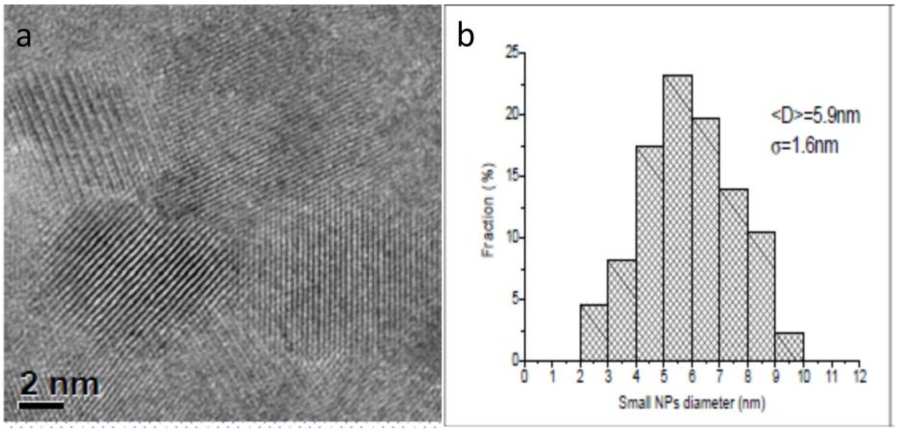

Figure 4.3- (a) HR-TEM images, (b) particles size distribution of Co_3O_4 NPs assembled coating prepared by PLD at substrate temperature of 150 °C with laser fluences of 3J/cm^2.

Fig 4.4 shows the micro-Raman spectra of the Co_3O_4 coatings deposited at 150 °C with different laser fluences (3, 5, and 7J/cm^2). The acquired spectra show the appearance of the respective modes as predicted by group theory for (space group (*F3dm*)) Co_3O_4. It is clearly seen that the active 5 Raman modes of A_{1g} at 665 cm^{-1}, E_g at 466 cm^{-1}, $3F_{2g}$ at 190, 507, and 602 cm^{-1} are present.

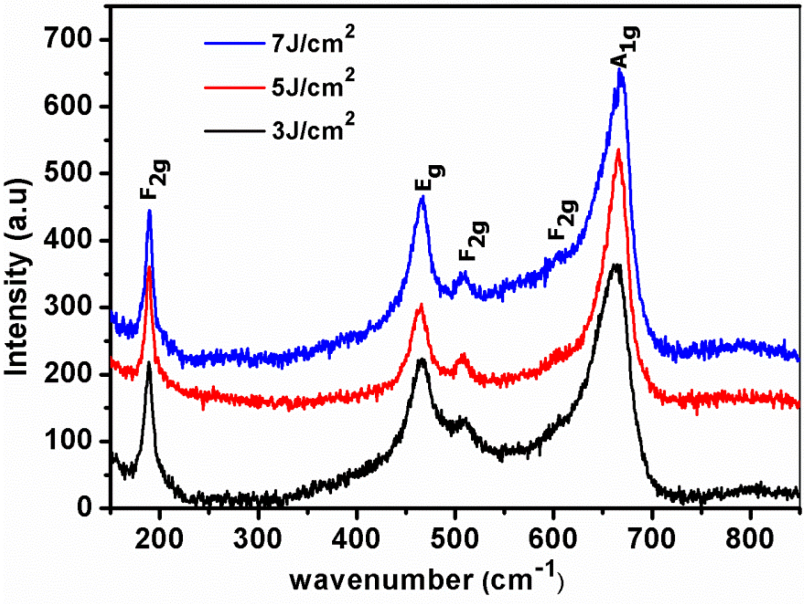

Figure 4.4- Raman spectra of Co_3O_4 NPs assembled coatings prepared by PLD at substrate temperature of 150 °C with different laser fluences (a) 3J/cm^2, (b) 5J/cm^2, and (c) 7J/cm^2.

The band at the position 665 cm^{-1} (A_{1g}) signals the octahedral site and the band at 190 cm^{-1} signals the tetrahedral site [142, 145, 146]. Broad nature of the peaks with low intensity indicates the formation of mixed phase with nanocrystalline Co_3O_4.

4.3.2 NPs assembled Co_3O_4 coating for photocatalysis

The photo catalytic activity of the Co_3O_4 NPs assembled coatings deposited at various laser fluences (3, 5, and 7J/cm^2) was tested by examining the degradation of MB dye (2 ppm, 50ml solution) as a function of time. The decrease in relative concentration of the

MB dye was estimated by measuring the relative intensity of the peak at 664 nm from the optical absorbance spectra. The degree of discoloration was expressed in the form of degradation ratio (1 − [A/A_0]) where A_0 is the absorbance at $t = 0$ and A is the absorbance at given reaction time.

Fig 4.5 shows the percentage degradation of MB dye in presence of visible light and 1ml of 100 mM H_2O_2 solution using the Co_3O_4 coating with weight of 1.2 mg in all experiments. The photocatalytic reaction of MB dye with light and H_2O_2, without catalyst was also tested as presented in fig 4.5.

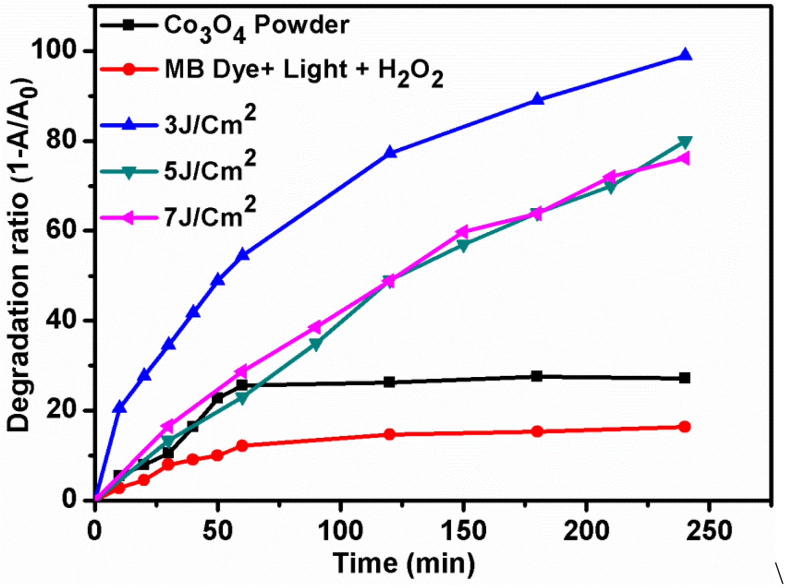

\

Figure 4.5- Time dependant photocatalytic activity of Co_3O_4 NPs assembled coatings synthesized by PLD using different laser fluences and powder in presence of H_2O_2 and visible light for degradation of MB Dye (2 ppm, 50ml solution).

Co_3O_4 NPs catalyst synthesized at 3 J/cm^2 shows 100% degradation after 4 h, but the coatings deposited at higher fluences, 5 J/cm^2 and 7 J/cm^2, display reduction in amount of degradation of MB dye to 80% and 75% respectively. There was no significant change in the discoloration of MB dye for the powder Co_3O_4 catalyst after reaching 24% in 1h. This behavior is mainly attributed to the Co_3O_4 NPs agglomeration during the reaction course for the powder form, which further reduces the number of $OH^•$ radical generation needed for the degradation of the dye. The high activity for the PLD coatings is mainly attributed to the presence of spherical NPs on the catalyst surface which are well dispersed with size distribution in a narrow range. Due to the small average size (6 nm: fig. 4.3), the assembled NPs provide large number of under-coordinated catalytically active sites on the surface. In addition, nanocrystalline nature of the catalyst offers high amount of grain boundaries which are linear defects with highly active sites with basic, acidic or redox functionality for catalysis. Most importantly, the NPs are partially embedded on the coating surface thus avoiding the particle agglomeration during the reaction time.

All these reasons are mainly responsible to produce higher catalytic activity in MB dye degradation, for the Co_3O_4 coatings as compared to the powder. The decrease in catalytic activity with coatings synthesized at higher laser fluence is mainly attributed to the presence of bigger NPs (above 30 nm size) and large droplets (200–500 nm), which decrease the surface area to volume ratio thus reducing the number of catalytic active sites on the surface of these coatings. The almost same values of catalytic activity produced by catalyst coatings deposited at laser fluence of 5 and 7J/cm^2 is mainly assigned to analogous morphology obtained at these high fluences. The IPC form of Co_3O_4 on the glass substrate is clearly demonstrating the advantage over the powder Co_3O_4 catalyst in terms of stability and activity.

4.3.3 3-D Hierarchical urchin Co_3O_4 micro/nanostructures

3-D Hierarchical urchin-like nanostructures are becoming more promising because these structures establish high surface area to facilitate catalysis reaction by providing a larger solid–liquid reaction interface area. Hierarchical flower-like $Co_{3x}Fe_xO_4$ structures [147], hierarchical assemblies of Au and AgI nano-crystals in the Fe_3O_4–SiO_2–Au–Ag–AgI composite particles [148] and three-dimensional semiconductor nano networks of TiO_2 and ZnO with controlled band gap energies are highly efficient in degrading the MB dye[149]. Urchin-shaped Fe_3O_4@Bi_2S_3 core-shell hierarchical structure with enhanced photo catalytic efficiency for degradation of Rhoda mine B (RhB) dye [150] was studied recently. In addition urchin-like iron oxyhydroxide (α-FeOOH) and (α-Fe_2O_3) oxide nanostructures exhibit very good ability to remove organic pollutants [151]. Finally 3D hierarchical rose-like $Bi_2O_2CO_3$ microspheres show an enhanced photo catalytic activity toward the degradation of RhB dye, MB dye and Methyl Orange (MO) dye mixed solutions [152] under visible light conditions.

Recently there has been a great interest towards the synthesis of the Co_3O_4 based hierarchical 3D nano structures by chemical methods and application of them in the field of energy and environment. It was reported that Co_3O_4 hierarchical urchins structure were highly efficient in degrading reactive black dye [153]. The enhanced photocatalytic activity was explained on the basis of the higher crystallinity, increased surface area, specific surface exposed planes and much enhanced solid-liquid interaction of the nano structures for adsorption and further catalytic reaction in presence of light. However, all these catalysts are produced primarily in form of powders, which have problems for sustainable photocatalytic process as we discussed in the previous section.

Here we developed the Co_3O_4 urchin like structures as coating form on glass substrates by thermal oxidation of the Co-B NPs assembled coatings prepared in vacuum and O_2 atmosphere by PLD (chapter 2, section 2.3.2). Thermal oxidation of all the Co-B coatings were carried out in air at three different temperatures (400, 500, and 600 ^oC) for 4 hrs in order to obtain the urchin structures. The Co-B coatings prepared in vacuum only shows *urchin Co_3O_4 structure* and the one prepared in O_2 atmosphere shows *porous urchin Co_3O_4 structure* after thermal annealing. The same kind of structures was also produced by chemical synthesis with optimized conditions through hydrothermal method (chapter 2, section 2.2.3). Photocatalytic activity of these structures was systematically investigated in presence of MB dye by varying experimental parameters with detailed mechanism.

4.3.4 Morphological and structural analysis

SEM image of as-deposited Co-B coating deposited in vacuum and O_2 atmosphere is presented in fig. 4.6a and fig 4.6b. Spherical particles with wide size distribution in the range of few nanometers to 1-3 micrometers were observed on the coating surface. Such morphology can be explained by the laser-induced phase explosion process as previously discussed (fig. 4.3).

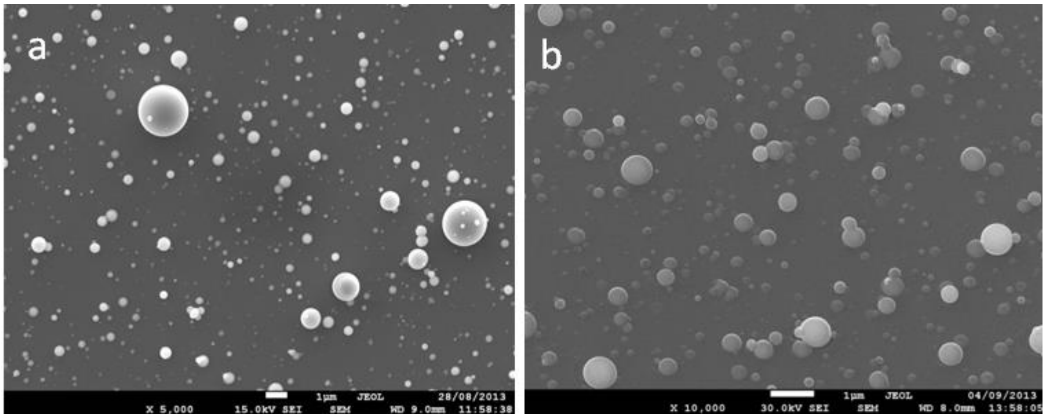

Figure 4.6- SEM images of (a) as-deposited Co-B coating prepared in O_2 atmosphere and (b) as-deposited Co-B coating prepared in vacuum by PLD.

SEM-EDS analysis confirmed the presence of cobalt and boron atoms along with oxygen on the spherical particulates in the Co-B coating deposited in O_2 atmosphere (fig 4.7a).

The Co-B coating deposited in vacuum (fig 4.7b) showed mainly the presence of cobalt and boron and with very low oxygen content due to the native oxide.

Bright field TEM image (fig. 4.7a) reveal that each particle attained a core-shell type of structure, where core is composed of heavy element while shell with lighter element as suggested by the color contrast. For elemental composition EDS spectra were acquired by focusing the electron beam (with diameter of about 5nm) on different parts of the sample (fig. 4.7a). The EDS analysis performed on shell and core, signifies that mostly cobalt metal forms the core (red circle 2) while the shell (red circle 3) is a mixture of Co, B and O with last two in the dominating amounts. The background (red circle 1) shows that more than 50% is boron and remaining are cobalt and oxygen

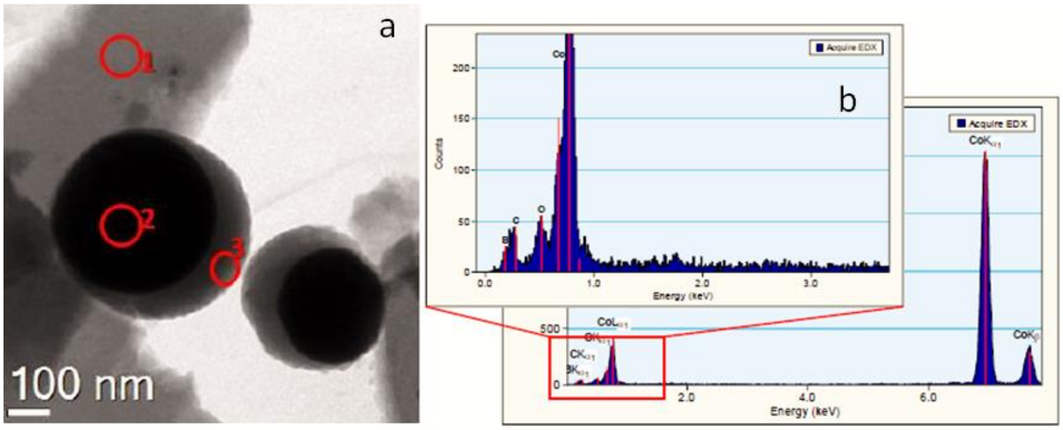

Region	**B (at %)**	**O (at%)**	**Co (at%)**
Cirlce 1 (background)	65±10	25±5	10±2
Cirlce 2 (core)	35±7	6±1	59±7
Circle 3 (shell)	40±7	34±5	26±5

Figure 4.7- Bright field TEM images of (a) as-deposited Co-B coating prepared in O_2 atmosphere and (b) EDS spectra acquired on the core, with quantification of elements (in at %).

As an example, the EDS spectra of the core (red circle 2) are shown in fig 4.7b and the representative figures of elements content is also shown (Note: EDS quantitative analysis of light elements (Boron and Oxygen) is very difficult and error-prone due to the selective absorption of their emitted X-rays by Cu grid on which the carbon film is deposited). In the shell an atomic ratio of O/Co is 1.3±0.5 and is compatible with the presence of Co_3O_4 phase. Annealing in air at 600 ^{o}C for 4 hrs induces structural/morphological alteration in both the coatings (Co-B deposited in vacuum and Co-B deposited in O_2 atmosphere) forming Urchin-like structures with growth of nanowires from the surface of the Co-B particles (fig.4.8).

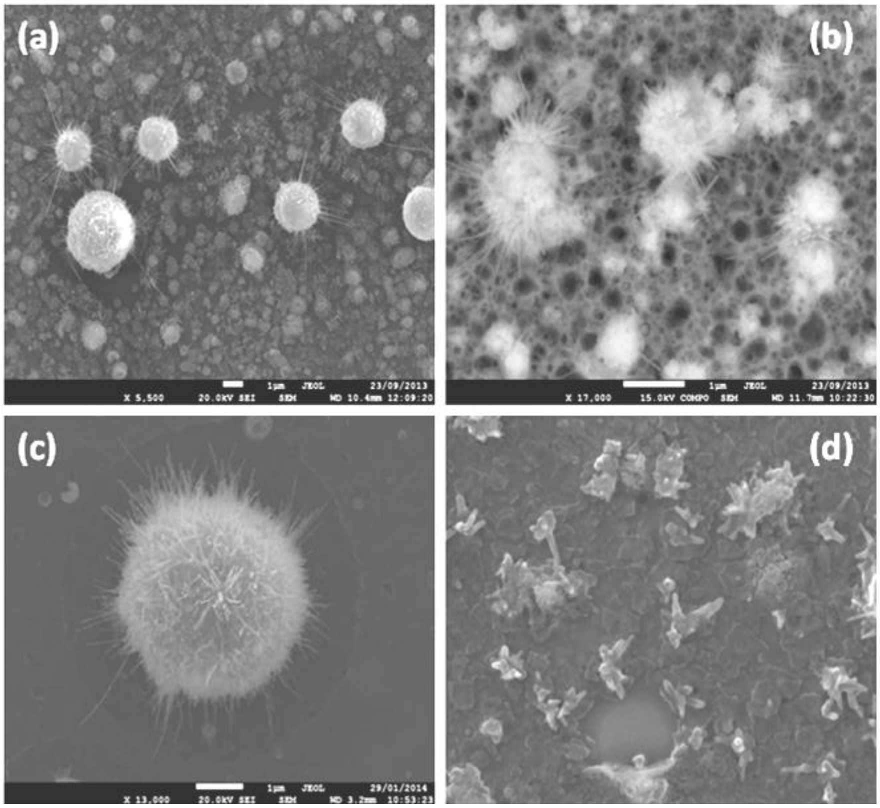

Figure 4.8- SEM images of (a) Co-B coating deposited in vacuum and (b) Co-B coating deposited in O_2 atmosphere, (c) single particle with well defined urchin structure, and (d) transformation of smaller particle into bunch of nano wires: after annealing at 600 °C for 4hr.

In addition to urchin, porous structure is also formed in the Co-B coating deposited in the oxygen atmosphere (fig. 4.8b), while vacuum deposited Co-B coating only shows urchin-like particles (fig 4.8a). Well-defined sea-like urchin structure comprise of spherical core with radially grown nanowires (NWs) on the surface (fig. 4.8c) are found on larger particulates of size above 500 nm while smaller particles transform into the bunch of small NWs (fig. 4.8d).

Higher magnification image of the NWs shows the extrusion marks on the surface suggesting the stress induced growth of the NWs (fig. 4.9a and fig. 4.9b). The proposed mechanism of the growth of these structures is explained later (section 4.3.5).

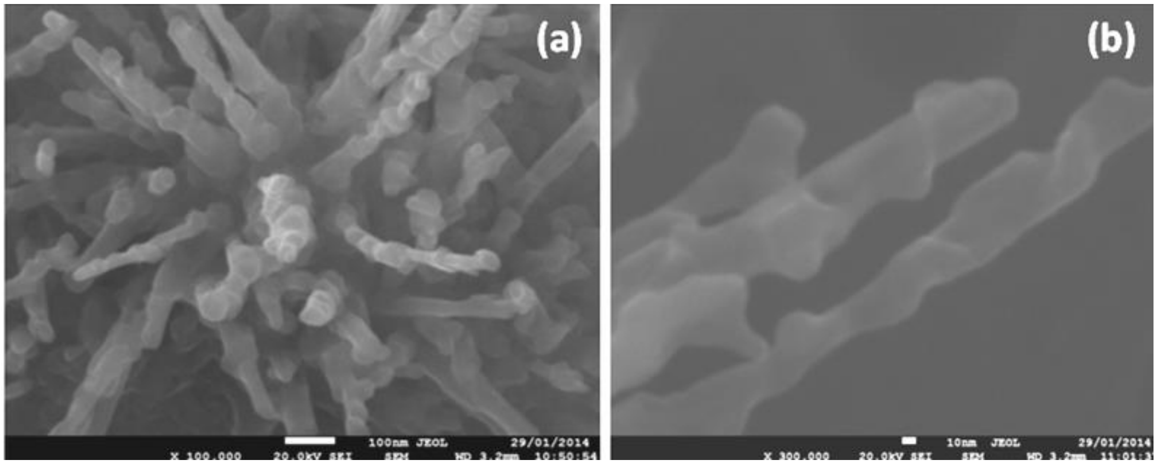

Figure 4.9- SEM images of (a) Nanowires with extrusion marks over urchin, (b) High magnification of nanowires showing the clear extrusion marks on the surface.

Further investigation by HR-TEM indicates that the NWs are polycrystalline with Co_3O_4 phase as shown in the fig 4.10. Fast Fourier transform (FFT) pattern (fig. 410a) of the indicated region (red color square) consists of bright spots due to the crystalline structure and the values of inter-planar spacing obtained by FFT of the HR-TEM image are in good agreement with the values of Co_3O_4 phase (*fcc-phase Fd3m* a=8.085Å)) as identified with the d-spacing and corresponding planes (table 4.1). Selected area EDS spectra (fig. 410b) establish that only oxygen and cobalt are present on the NW with atomic ratio of O to Co of about 1.4, which is compatible to Co_3O_4 phase. This clearly indicates the formation of Co_3O_4 phase after annealing at 600 °C.

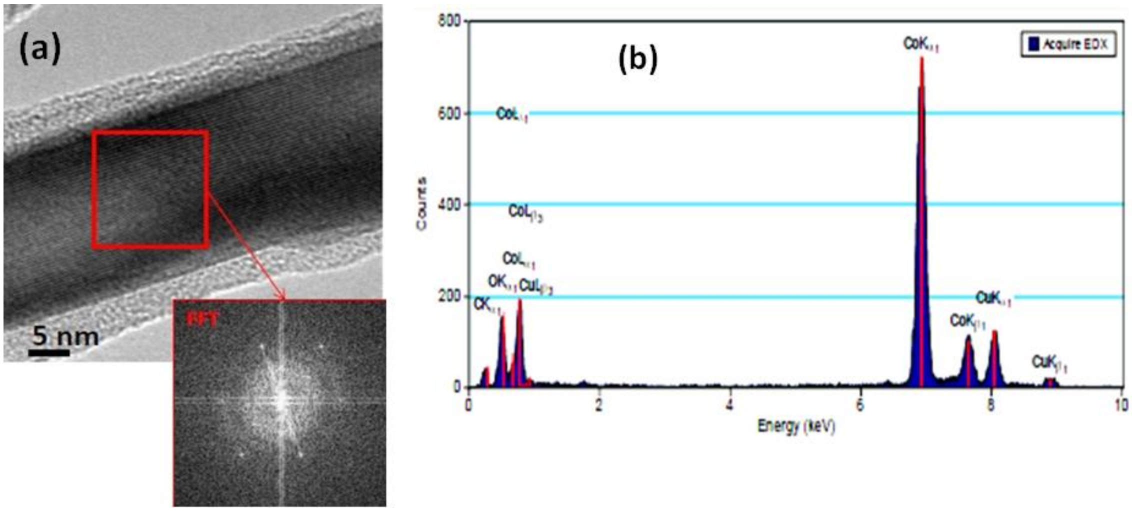

Figure 4.10- (a) HR-TEM image of NW and corresponding Fast Fourier transform (FFT)) and (b) the corresponding EDS of the NW.

Table 4.1. Inter-planar spacing values obtained by FFT from HRTEM image of NWs in urchin-like structure synthesized by PLD.

FFT-HR-TEM d(Å)	***Co_3O_4 d(Å) (hkl)***	***CoO d(Å) (hkl)***	***Co_2O_3 d(Å) (hkl)***
4.65±0.07	4.668 (111)		
2.83±0.05	2.858 (220)		2.870 (002)
2.44±0.05	2.438 (311)	2.461 (111)	

Co_3O_4 phase formation is further confirmed by analyzing the micro-raman and XRD spectra with respect to the temperature. Micro-raman spectra of these samples are presented in fig. 4.11. The Co-B coating deposited in vacuum shows only two Raman bands at 192 cm^{-1} and 485 cm^{-1} (fig. 4.11a) due to surface oxidation of Cobalt. After annealing in air, the distinct peaks at 192, 485, 525, 626 and 694 cm^{-1} corresponding to F_{2g}, E_g, F_{2g}, F_{2g} and A_{1g} modes of vibration respectively (fig. 4.11b, fig. 4.11c and fig. 4.11d) [145, 146], signal crystalline Co_3O_4 phase. These raman bands appear to be broad for Co-B annealed at 400 °C (fig 4.11b) and 500 °C (fig 4.11c) indicating partial crystallization of Co_3O_4 which is completed after heat treatment at 600 °C (fig 4.11d) as indicated by the sharp peaks with shift in peaks.

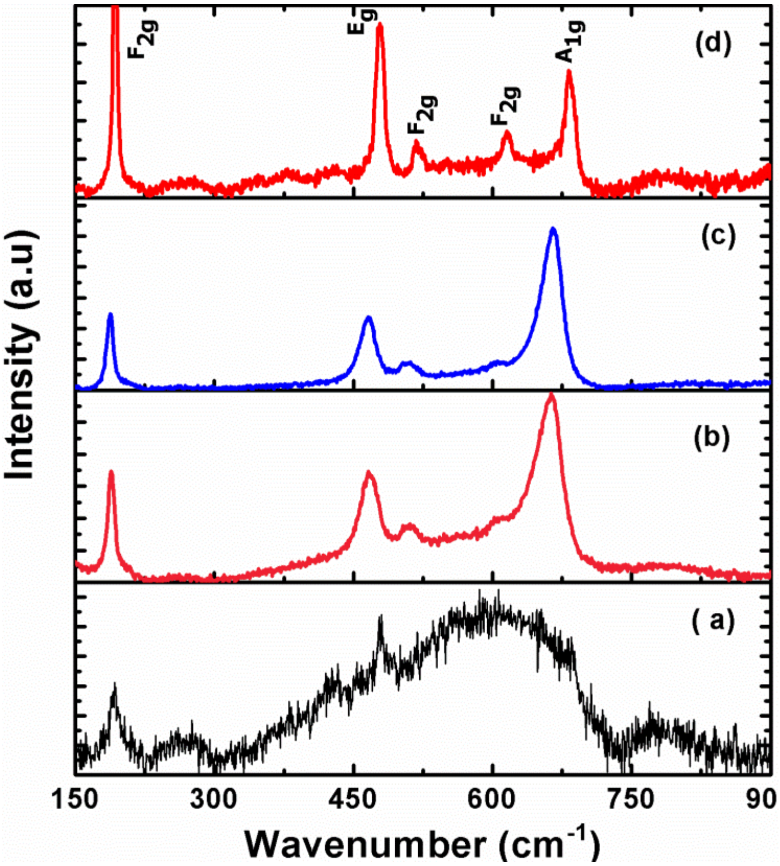

Figure 4.11- Raman Spectra of Co-B coating deposited by PLD under (a) vacuum condition and heat treated in air for 4 hrs at three different temperatures of (b) 400 °C, (c) 500 °C and (d) 600 °C.

The broadening and peak shift in the spectra indicate nano crystalline behavior (phonon confinement) along with presence of large defects and induced stresses (growth of NWs) due to high temperature oxidation [145, 154-156]. The signal in Raman spectroscopy is basically acquired from the surface or just below the surface by the inelastic scattering thus providing information only from the surface. Thus it is necessary to obtain the structural information of bulk by XRD that was carried out for all the coatings and reported in fig 4.12.

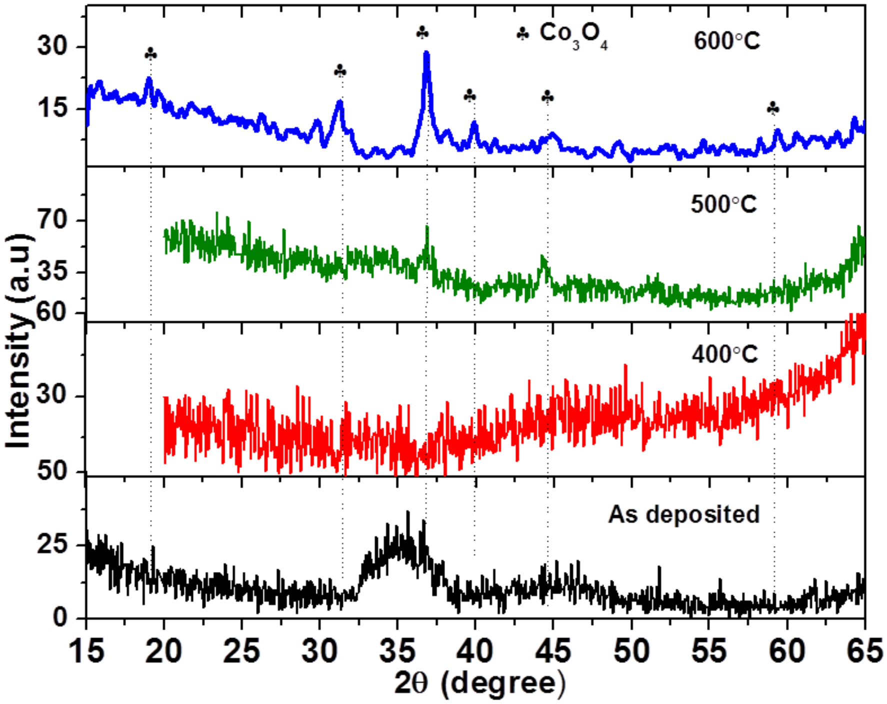

Figure 4.12- XRD pattern of Co-B coating deposited by PLD under vacuum condition and heat treated in air for 4 hrs at three different temperatures of 400 °C, 500 °C and 600 °C.

It is clearly seen from the fig 4.12 that, as deposited as well as Co-B coating heat treated at 400 °C display complete amorphous nature. XRD peaks centered at 19.0°, 31.2°, 36.9°, 38.6°, 44.8°, 54.5°, 59.4° and 65.2° assigned to face-centered spinel type cubic structure of Co_3O_4 are observed for the Co-B coating annealed at 600 ^oC [157, 158]. These diffraction peaks correspond to the reflections (111), (200), (311), (222), (400), (422), (511) and (440) respectively as acquired from JCPDS data file 009-0418. Calculated crystal size, of 18 ± 5 nm, is smaller than the average diameter (45 nm) of NWs measured by SEM and TEM indicating that the NWs are composed of several grains with average size of 18 nm. Among the measured peaks very few diffraction peaks are observed for Co-B coating annealed at 500 ^oC indicating that complete crystallization of 3D urchin-like nanostructures occurs after heat treatment at 600 ^oC. No diffraction peaks due to metallic cobalt, other cobalt oxides and boron oxides phase are detected in XRD pattern.

4.3.5 Understanding the formation mechanism of the 3-D urchin structures

In general, the growth of 1D nano structures like nanorods, nanoneedles etc, involves a catalytic-assisted vapor-liquid-solid (VLS) mechanism or vapor-solid (VS) mechanism [159]. For VLS growth, the growth temperature has to be higher than the eutectic temperature of two elements so that these elements form an alloy as liquid droplet. From the phase diagram of Cobalt and Boron, the eutectic temperature of Co and Boron is around 1100 °C. In our work, annealing temperature was well below 1100 °C and the melting points of Co (1495 °C), B (2076 °C), and Co_3O_4 (900°C). Thus VLS and VS mechanisms are not responsible for the growth of the urchin nano structures.

Very recently Hsu et al. [160] developed α-Fe_2O_3 urchin-like structures by thermal oxidation of Fe powder in air in temperature range of 300-400 °C. Here the growth mechanism of nanoflakes is suggested to be selective directional growth via inter-diffusion of oxygen and iron atoms.

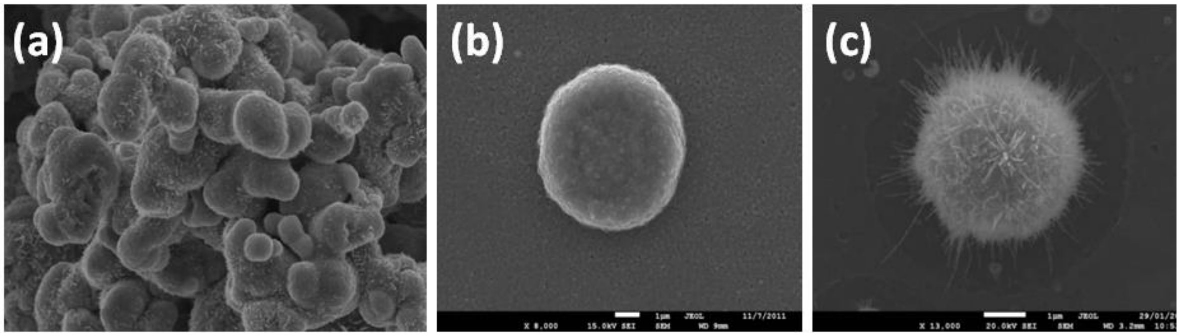

Figure 4.13- SEM image of annealed, (a) commercial Co powder, and (b) Co coating and (c) Co-B coating synthesized by PLD, in air at 600 ^{o}C for 4 hrs

In order to verify this type of growth mechanism, Co powder with particle size of 10 µm and Co coatings prepared by PLD, having morphology like Co-B coating, were annealed in air under similar condition (600 °C for 4hrs). The respective SEM images after annealing in air are shown in fig.4.13a (Co powder), fig. 4.13b (Co coating) and fig. 4.13c (Co-B coating). No sign of urchin or NWs was observed (fig 4.13a and b) thus discarding the mechanism reported by Hsu. et al [151]. This shows that boron certainly plays a huge role in the urchin formation. To investigate the growth mechanism of urchin structure formation, annealing of the Co-B coating deposited in vacuum was done at various temperatures. SEM images of the Co-B coatings annealed at 400, 500 and 600 ^{o}C for 4 hrs and the Co-B coating as deposited in vacuum are shown in fig. 4.14 respectively.

Co-B particles obtained by PLD are in perfect spherical shape with smooth surface (fig. 4.14a). After annealing at 400 ^{o}C the particulates appear to disintegrate to form small nanoparticles of size 30-60 nm on the surface (fig. 4.14b). Further increase in temperature at 500 ^{o}C initiates the evolution of NWs from the surface of the particulates (fig. 4.14c).

However, complete urchin-like structure with well-developed NWs is obtained only after heat treatment at 600 ^{o}C (fig. 4.14d).

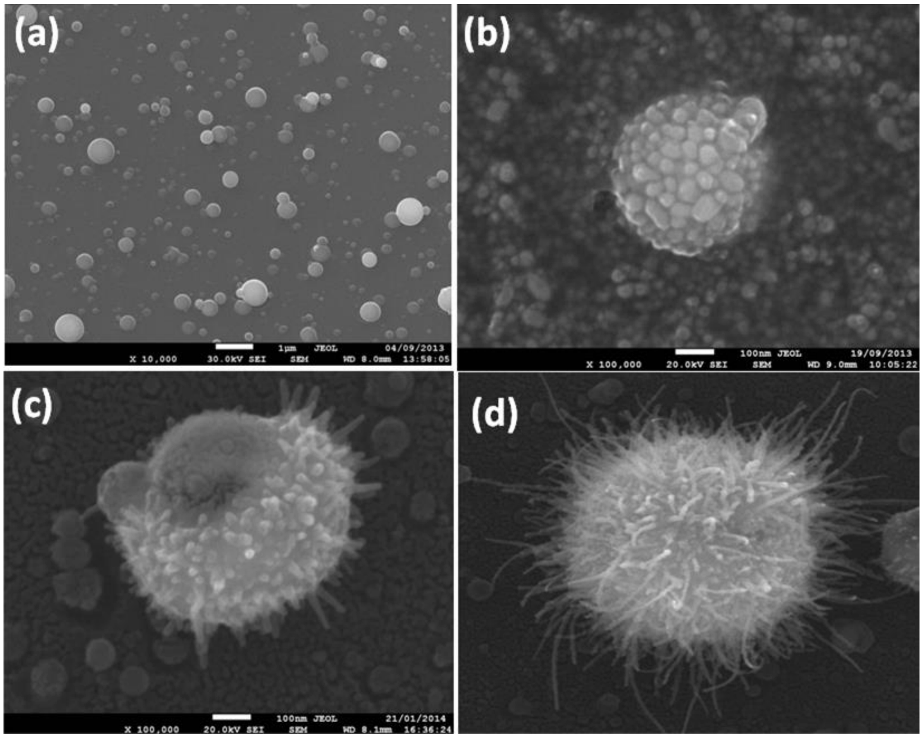

Figure 4.14- SEM images of Co-B coating deposited by PLD (a) under vacuum condition and heat treated in air for 4 hrs at three different temperatures of (b) 400 ^{o}C, (c) 500 ^{o}C and (d) 600 ^{o}C.

On the basis of obtained results a plausible mechanism is proposed here. In as deposited Co-B coating the particulates are of core-shell structure, where cobalt core is covered with the shell composed of Co, B and O (as evidenced from HR-TEM; fig. 4.7). Thus during oxidation at 400 ^{o}C the phase separation might occur in the shell between boron oxide and cobalt oxide forming nanoparticles (NPs) of later. These NPs are under stress condition, created by large difference in the thermal expansion coefficients of boron oxide (0.5×10^{-6} K^{-1}) and cobalt oxide (13×10^{-6} K^{-1}). Increasing temperature (500 to

600 °C) will further increase the stress level which is released by forming NWs. The NPs found in the initial stage act as the nucleating sites for the growth of NWs. Cobalt is provided from the core for further growth of NWs by diffusing toward outward direction. The stress induced growth of NWs is completely evident from the extrusion marks on the surface of the NWs (fig. 4.9). Further extensive studies are under way to exactly understand the mechanism of the NWs growth in the forthcoming work.

4.3.6 3-D urchin like Co_3O_4 structures for photocatalysis

Photocatalytic activity of the urchin structures prepared from both thermal oxidation of the Co-B coatings and the chemical method was carried out as for the NPs assembled Co_3O_4 coatings. Here, the effects of MB dye concentration (2 ppm, 5ppm and 10 ppm), H_2O_2 concentration as well as re-usability test for longer times were also studied. Since it is known that adsorption of dye (solid-liquid interaction) on the catalyst is a major prerequisite condition for any heterogeneous catalytic reaction. The catalyst coatings were kept in the dye solution in dark for 30 min and adsorption of dye was seen to be 3-5% for the urchin and porous/urchin Co_3O_4. Co_3O_4 NPs assembled coating was able to adsorb only 1-2 % revealing higher solid-liquid interaction between the catalyst and dye molecules for porous urchin structure. The better adsorption of dye on the urchin catalyst is due to high surface area provided by 3-D urchin structure in presence of the porous structure in background. Initially the degradation of the MB dye was investigated under different conditions such as presence of only a*)* light, b*)* H_2O_2 with light, and c*)* Co_3O_4 catalyst coating in presence of light. In all these cases maximum degradation of 10-15 % (fig. 4.5) was measured even after prolonged period of 6-8 hrs. The dye was completely degraded only when *catalyst* is exposed to *visible light* in presence H_2O_2 (as external oxidant), thus indicating that dye is decolorized by Photo-Fenton reaction mechanism only. This mechanism is further established in later section (fig. 4.24).

Fig. 4.15 represents the rate of degradation of MB dye (10 ppm, 30ml) in presence of light and H_2O_2 (0.5 M, 1ml) using Co_3O_4 NPs assembled coating, urchin Co_3O_4 coating and porous urchin Co_3O_4 coatings. In all experiments the weight of the catalyst and projected area was maintained around 1mg and 2.5 × 7.5 cm^2 (glass slide) respectively.

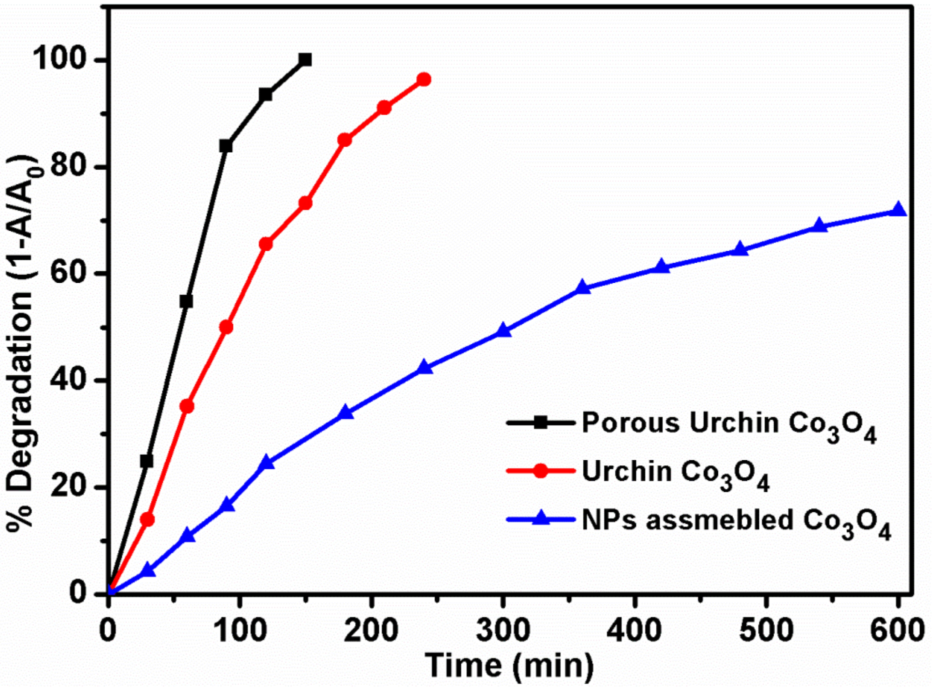

Figure 4.15- Time dependent photocatalytic degradation ratio of MB solution (10 ppm, 30 ml) in presence of 1 ml of H_2O_2 (0.5 M) and visible light using different nanostructures (NPs assembled, Urchin and porous urchin) of Co_3O_4 catalyst coatings.

Even after 10 hrs the NPs assembled coating was not able to completely degrade MB dye while porous urchin structure required only 2.5 hrs to reach 100 % degradation. On other hand, coating with only Co_3O_4 urchin structure produces colorless solution after 4.5 hrs. These results show that the urchins with porous structure are more effective than only urchin Co_3O_4, but the difference is small so the presence of urchin structure is mainly responsible for the high photocatalytic activity.

To better understanding this point, Co-B coating deposited in vacuum atmosphere was annealed at different temperatures and photocatalyst activity was tested. Degradation of MB dye solution (10 ppm) using Co-B coating annealed at 400, 500 and 600 °C, in presence of H_2O_2 (0.5 M, 1 ml) and visible light is presented in fig. 4.16. No change in degradation rate was observed for the samples annealed at 400 and 500 °C in comparison to as-deposited Co-B coating. All three samples degrade only 40 % of the dye in 4 hrs while complete colorless solution is achieved in 4.5 hrs for urchin Co_3O_4 structure obtained at 600 °C annealing (urchin fully crystallized).

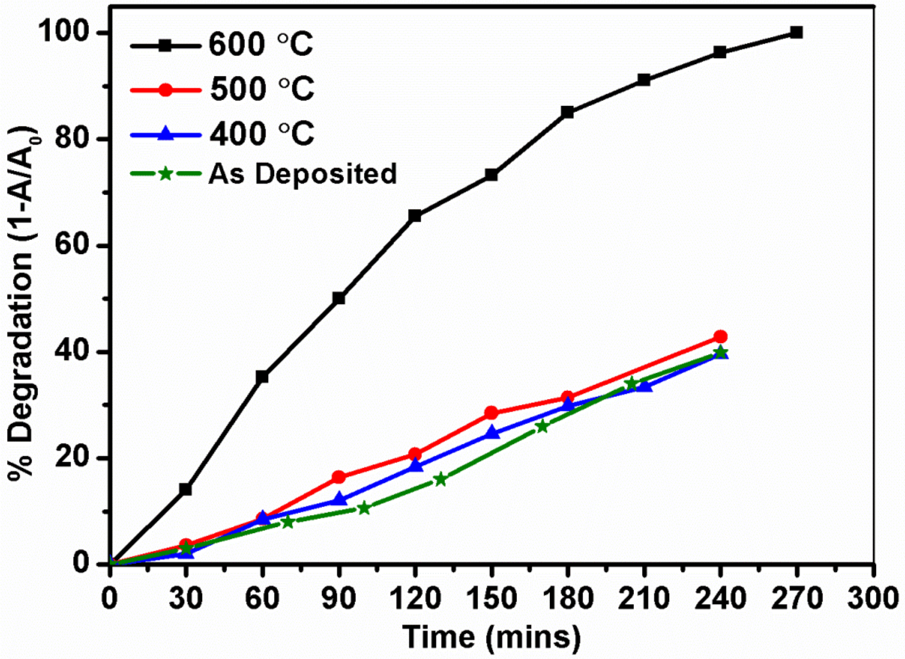

Figure 4.16- Time dependent photocatalytic degradation ratio of MB solution (10 ppm, 30 ml) in presence of 1 ml of H_2O_2 (0.5 M) and visible light using Co-B coating deposited by PLD under vacuum condition and heat treated in air for 4 hrs at three different temperatures of 400 °C, 500 °C and 600 °C.

It is clearly noticeable that urchin Co_3O_4 is highly active for the degradation of dye. The presence of porous structure is also showing a positive effect by facilitating more adsorption of dye molecules on the catalyst.

4.3.7 Chemical Co_3O_4 3-D urchin structures

In past, urchin structure of Co_3O_4 was mainly prepared by the hydrothermal method or other chemical techniques [153]. To best of our knowledge, the Co_3O_4 urchin structure developed by physical technique such as PLD and successive thermal oxidation was reported here for the first time. Thus it is necessary to have a comparison of the photocatalytic performance of the urchin structures prepared by both methods (physical and chemical) for future applications. Chemical Co_3O_4 urchin in form of coating over glass substrate and powder was synthesized by hydrothermal method (chapter 2, section 2.2.3) and tested for MB dye (10 ppm) degradation in presence of H_2O_2 (0.5 M, 1 ml) and visible light. Catalyst amount of 5 mg was required to completely cover the glass slide (2.5×7.5 cm^2) and thus the amount of Co_3O_4 urchin powder used for degradation test was also kept about 5 mg.

4.3.8 Morphological and structural analysis

Surface morphology of the chemical Co_3O_4 urchin coating was investigated to see the difference between the PLD urchin and chemically prepared urchins. Uniformly distributed 3-D urchin-like spheres with size in the range of 8-12 µm were evidently visible in SEM image of as prepared samples (fig. 4.17a). High magnification SEM suggest that NWs are tapered with length around 4-6 µm and width at bottom around 150-200 nm and at the tip of about 50-80 nm (fig. 4.17b). The surface of NWs is highly smooth without any major defects. Heat treatment at 600 ^{o}C in air for 4hrs did not cause any change in the primary urchin-like structure, but the shape and surface of NWs completely changed as in fig 4.17c. The length of NWs is not affected but the shape has transformed from tapered to uniform rod-like having nearly uniform width from top to bottom. The diameter of these nano-rods varied from 40 to 150 nm as examined through SEM image (fig. 4.17c).

The building blocks of NWs are now collection of irregular shaped nanoparticles of size 10-30 nm as confirmed by HR-TEM (fig. 4.17d). Set of crystalline planes in each NPs are clearly distinguished in HR-TEM image (fig. 4.17e). The distance between the lattice fringes was measured by FFT of HR-TEM image and it matches well with the Co_3O_4 phase (as indicated by arrow in the fig 4.17e).

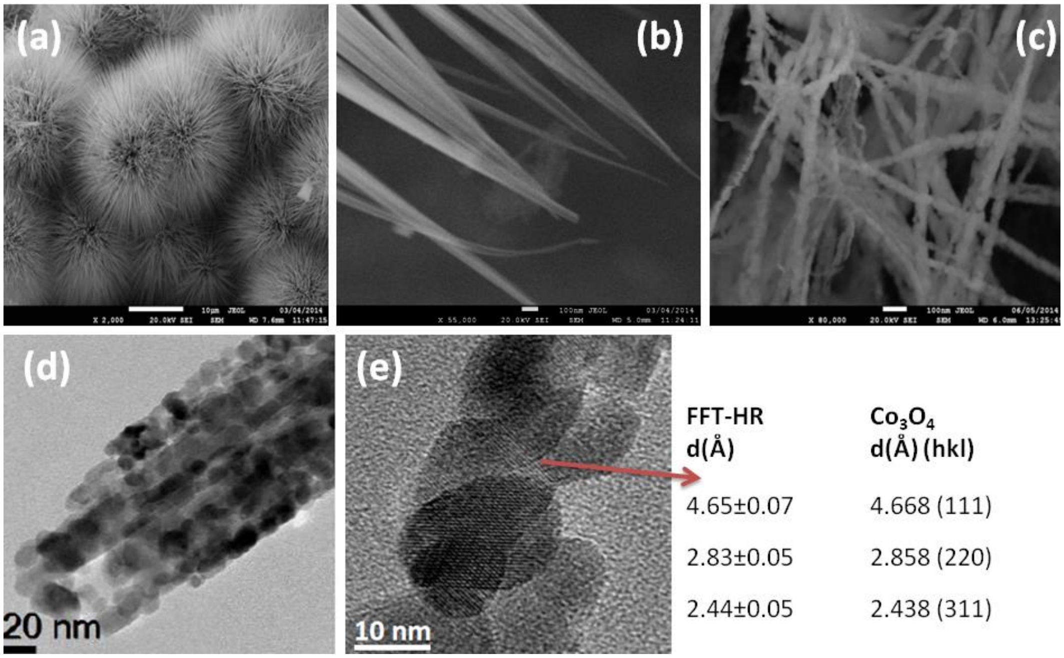

FFT-HR d(Å)	Co_3O_4 d(Å) (hkl)
4.65±0.07	4.668 (111)
2.83±0.05	2.858 (220)
2.44±0.05	2.438 (311)

Figure 4.17- SEM images of chemically (a) as prepared 3-D Urchin-like particles by hydrothermal method, (b) magnified image of (a): showing tapered NWs and (c) NWs obtained after heat treatment of the chemical urchin at 600 ^{o}C for 4 hrs in air. (d) Bright field TEM image showing NWs obtained after heat treatment is composed of NPs, (e) HR-TEM of these corresponding NPs with the corresponding d spacing vales.

However, core in this chemical urchin-like structure is hollow thus the complete structure assembly is held by the radially oriented NWs (fig. 4.18a). This is clearly indicating that the chemical urchins are of free standing NWs arranged in 3-D manner, while the urchins obtained by PLD are strongly supported by the core (fig. 4.18b).

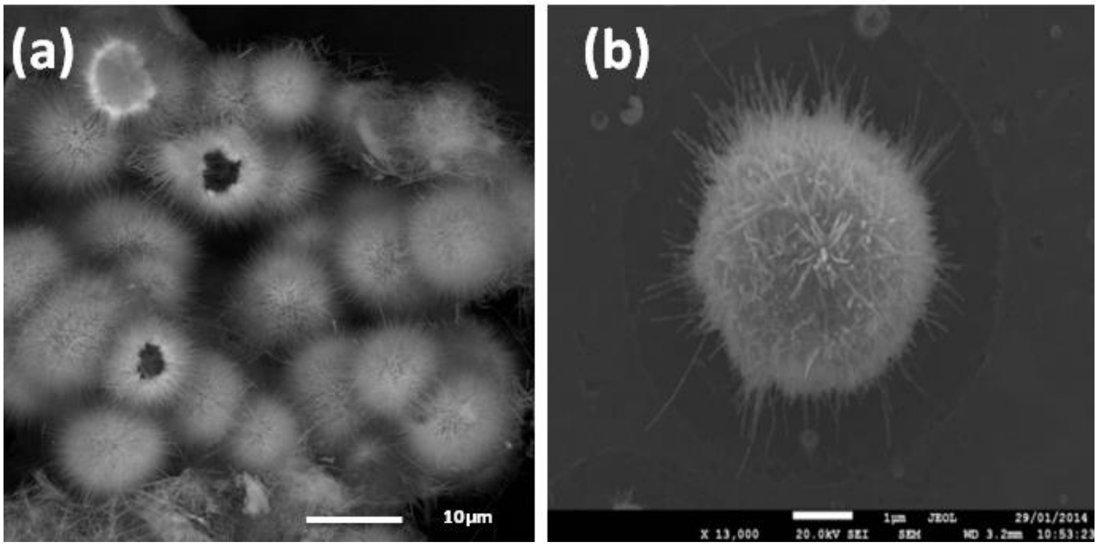

Figure 4.18- SEM images of (a) Chemical urchin with hollow structure, (b) PLD urchin with solid core.

SEM and HR-TEM results provided the morphological and structural information of the chemical urchins. To gain more evidence on the chemical urchins, XRD and micro-Raman analysis were carried out. XRD pattern (fig. 4.19a) of as deposited chemical urchin indicates orthorhombic cobalt hydroxide carbonate hydrate $(Co\ (CO_3)_{0.5}\ (OH)_{0.11}\ H_2O$ phase and after annealing at 600 ^{o}C in air these are peaks corresponding to spinel type cubic structure of Co_3O_4 with the *Fd3m* space group (fig. 4.19b). The crystal size of 24 ± 4 nm is in good agreement with the size of nanoparticles in the nano-rod as observed by TEM (fig 4.17e).

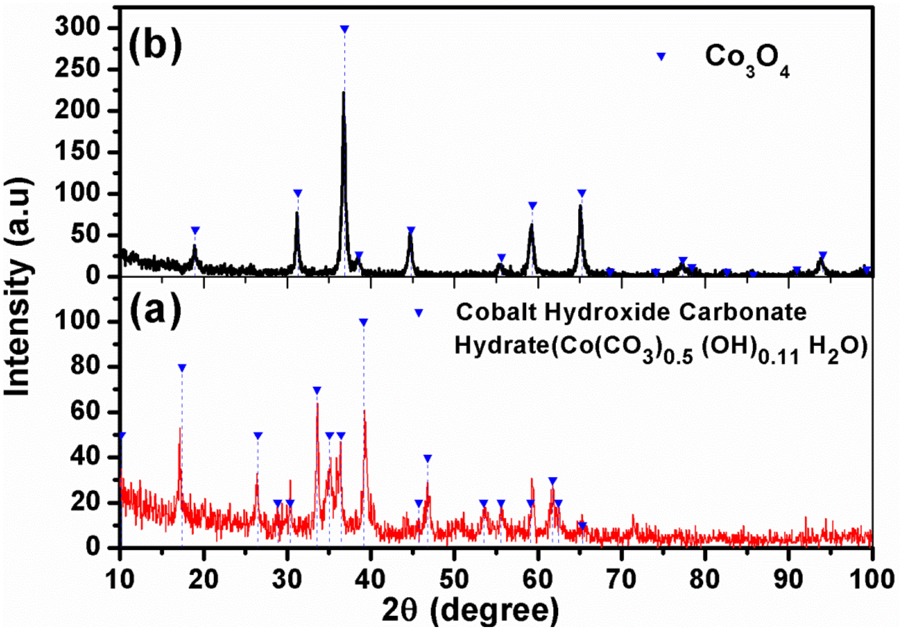

Figure 4.19- XRD pattern of (a) as-prepared chemical urchin coating and (b) after heat treatment at 600 °C for 4 hrs in air.

Additionally, micro-Raman measurements for the chemical urchin structures after annealing represent only Co_3O_4 phase as shown in fig. 4.20. The similar results were also observed for urchins prepared by PLD after thermal oxidation (fig 4.11).

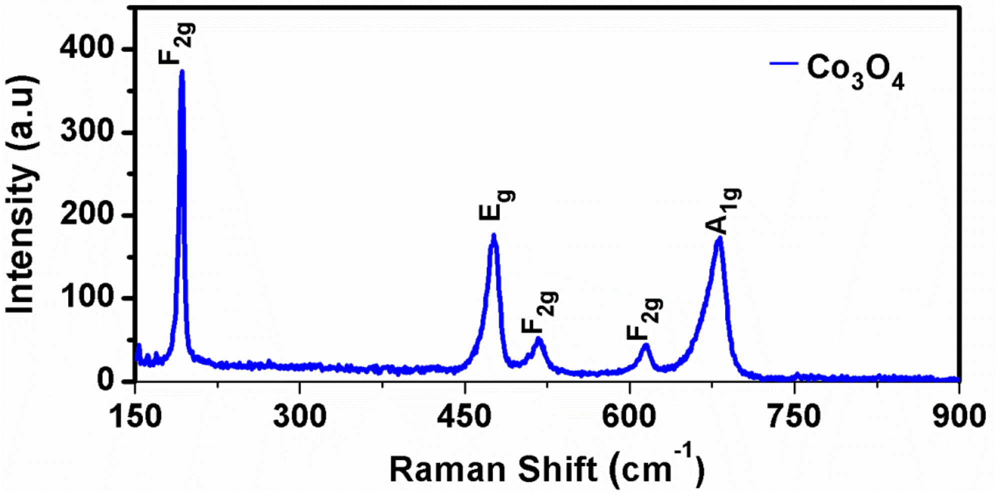

Figure 4.20- Raman spectra of heat treated chemical urchin Co_3O_4 catalyst at 600 °C for 4 hrs in air.

The mechanism involved in formation of this urchin was well explained by Riu et al. [46] on the bases of experimental evidence. In brief, the process involves formation of micro particles over which one dimensional NWs grown by dissolution of cores through Ostwald ripening. These NWs at high temperatures disintegrate forming nano-rods assembled with nanoparticles.

4.3.9 Chemical Co_3O_4 urchins for photocatalysis

The degradation activity of the chemical urchin coatings and powder of the same are shown in fig 4.21, and compared to the PLD porous urchin Co_3O_4 coating (1 mg),

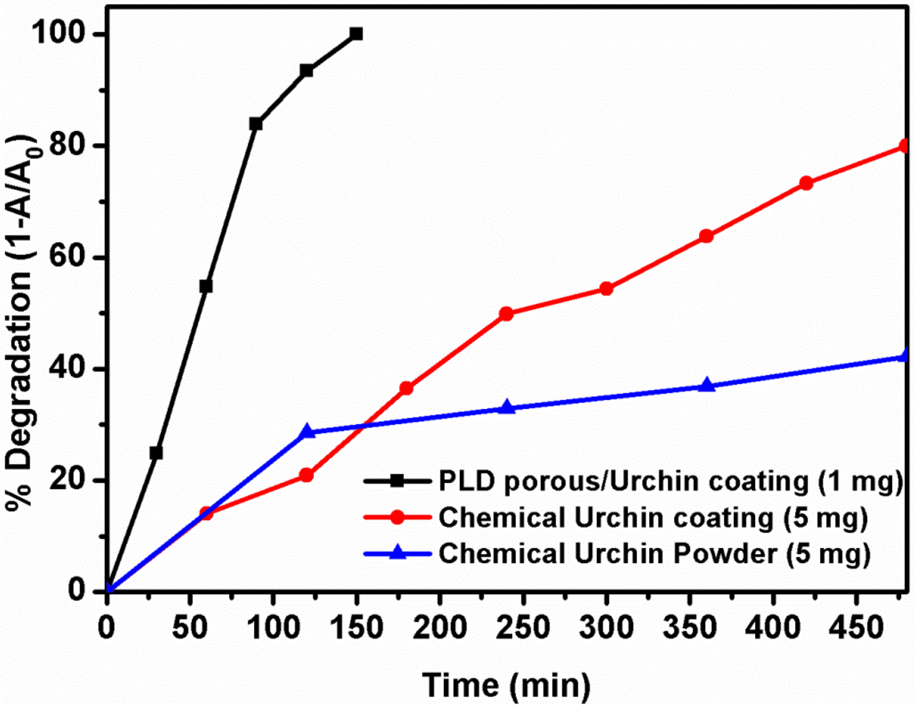

Figure 4.21- Time dependent photocatalytic degradation ratio of MB solution (10 ppm, 30 ml) in presence of 1 ml of H_2O_2 (0.5 M) and visible light using urchin Co_3O_4 coatings prepared by PLD and chemical urchin coating over glass substrate and urchin powder prepared by hydrothermal method.

The chemical Co_3O_4 urchin coating display nearly five times lower degradation rate for MB dye and was able to degrade only 80 % in 8 hrs. However, the chemical urchin in form of coating was better than in powder form where later degrads only 57 % in 8 hrs (fig 4.21). Agglomeration of urchin like particles in the dye solution during the reaction course may be the prime reason for reduced catalytic activity because for first 2 hrs the degradation rate for coating and powder of chemical Co_3O_4 urchin was similar but with time the rate falls drastically due to agglomeration in powder catalyst.

In order to understand the obtained lower catalytic activity, SEM analysis of the urchins prepared by PLD and chemical method after the degradation experiments is shown in figure 4.22. SEM image in fig 4.22a shows that urchin structure completely collapsed and the broken NWs aggregate to form large particles of size 8-10 µm. Since the urchin structure was held by the NWs without core particle thus during the constant stirring the friction caused by the aqueous dye solution can disintegrate the urchin structure. Another important factor is that the NWs are built by the NPs which are loosely bound to each other as observed in TEM images (fig. 4.17). These NPs can be easily separated to cause fragmentation of NWs in urchin structure, while in case of PLD prepared Co_3O_4 urchin the structure is well maintained even after the reaction cycle shown in fig. 4.22b. Thus the stability of urchin structure is established by the core from which NWs not only grows but are also strongly held over by their surface to keep the original structure intact even after reaction cycle.

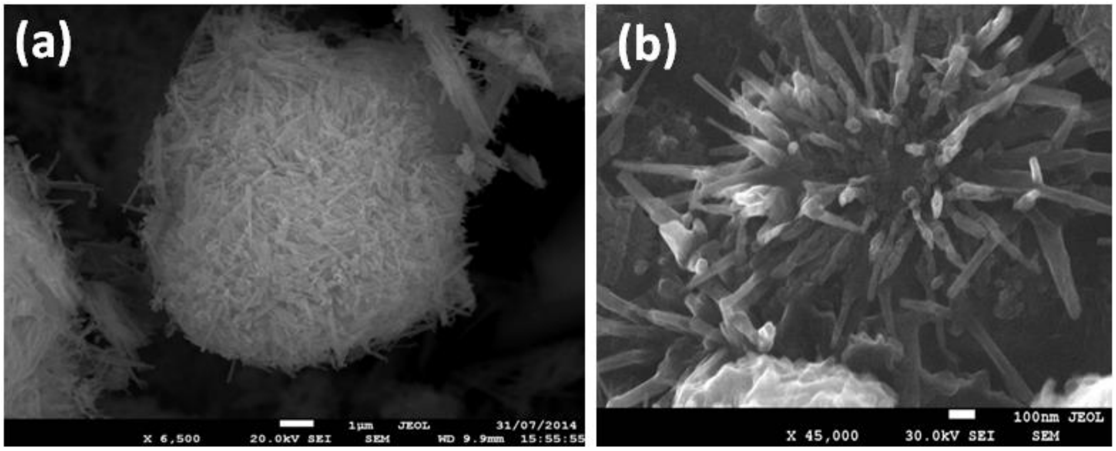

Figure 4.22- Morphology obtained by SEM of (a) chemical Co_3O_4 urchin and (b) PLD synthesized Co_3O_4 porous/urchin coatings after MB dye degradation reaction.

Now, it is highly desirable to look at the re-usability test of the urchins by PLD. The stability of the PLD prepared Co_3O_4 urchin structure was investigated by recycling the coating 5 times for degradation of MB dye (10 ppm) in presence of H_2O_2 (0.5M, 1 ml) and visible light. After 5th cycles (fig. 4.23a), 90 % degradation was achieved after 2.5 hrs by PLD synthesized porous/urchin Co_3O_4 coating. This shows that urchin structure is highly stable on the surface of the coating and strongly attached to the substrate. The minor decrease in the activity is explained in terms of negligible loss of catalyst (0.1 mg) during constant stirring and washing after each run. On the other hand, for NPs assembled Co_3O_4 coating prepared by PLD the degradation decreases to 63 % after 5th cycle because of the mechanical detachment of the NPs (fig 4.23b). Chemical Co_3O_4 urchin coating cannot be reused again for dye degradation due to major loss of the catalyst from the substrate.

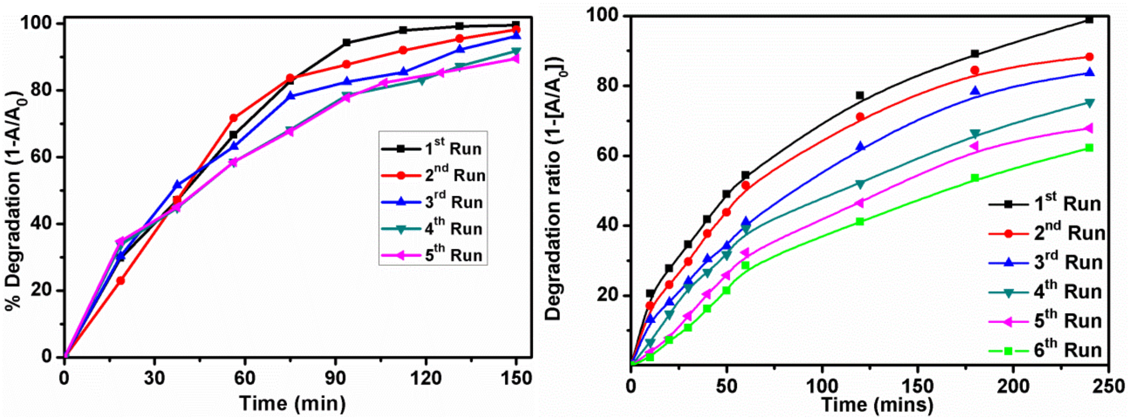

Figure 4.23- (a) Recycling behavior of porous/urchin Co_3O_4 coating prepared by PLD and thermal oxidation in air for 4 hrs at 600 °C, (b), Recycling behavior of Co_3O_4 NPs assembled coating, prepared by PLD, for MB dye degradation.

Finally the enhanced catalytic activity of Co_3O_4 urchin synthesized by PLD and thermal oxidation treatment is mainly attributed to the following features established from the above results:

- Urchin-like structure with NWs in narrow range of 30-60 nm and length of 1-2 µm provides very high surface area for interaction with dye molecules
- The core in urchin structure strongly held the NWs on the surface to provide high stability against agglomeration of the NWs during reaction course not like as in case of chemically prepared urchin coating.
- NWs are polycrystalline in nature possessing large amount of grain boundaries with width 0.5-1 nm on the surface which can be considered as linear defect containing atoms with low coordination number as compared to atoms in the ideal bulk crystallites. Thus, these grain boundaries regions are highly catalytic active sites with basic, acidic or redox functionality.

- Porous structure formed on the coating surface not only improve the surface area but also allow the dye molecule to penetrate to the inner surface of the coating to offer higher absorption and degradation of dye molecules.
- Good adhesion property of urchin does not cause any aggregation during the reaction course and remain attached to the surface for further reuse.
- In addition to these promoting features, the catalyst coating may be easily recovered and reused, thus can be used as ON/OFF switch for photocatalysis reaction as well as in continuous flow reactor.

4.4 Mechanism for MB Dye degradation

The degradation of MB dye can occur through mechanisms depending on the route of OH° radical generation,

1. OH° generation by direct photolysis of H_2O_2: this happens only in presence of UV light,
2. OH° generation by photo excitation of the Co_3O_4: this cannot be seen here because the standard redox potential of Co^{+3}/Co^{+2} (+1.82 V) is lower than that of OH°/OH^{-} (+1.99 V),
3. OH° generation by Photo-Fenton reaction: the Co^{+2} ions on the surface of the catalyst react with H_2O_2 and generate OH° radicals (eq. 4.1) to degrade the dye [128, 129]

$$Co^{+2} + H_2O_2 \rightarrow Co^{+3} + OH^{-} + OH^{\circ} \qquad 4.1$$

$$Co^{+3} - L + hv => [Co^{+3} - L]^{*} \rightarrow Co^{+2} + L\cdot \qquad 4.2$$

4. Excited Co^{+3} complex ($Co^{+3} - L$) undergo ligand-to-metal charge transfer in presence of light (eq. 4.2). The by Co^{2+} ions are regenerated by reduction of the

Co^{3+} with the ligands present in the solution (possible ligands are: OH^-, HO_2^-, carboxylates, etc.).

To prove the Photo-Fenton reaction the effect of H_2O_2 concentration was studied on the dye degradation and the respective results are shown in fig 4.24.

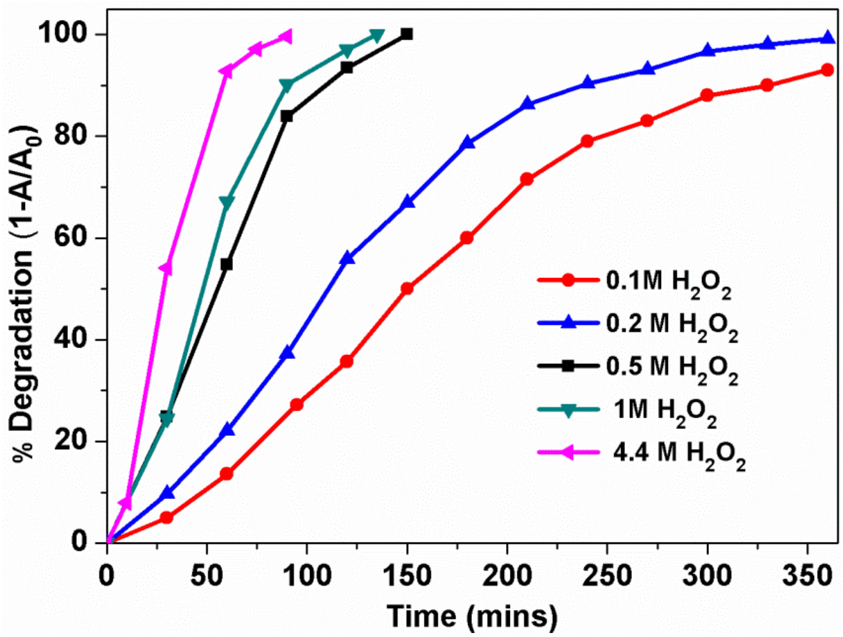

Figure 4.24- Effect of H_2O_2 concentration on the time dependant MB dye degradation

The degradation efficiency of MB Dye (10 ppm, 30ml) is enhanced with increase in the H_2O_2 concentration as seen in the fig 4.24, at 0.5 M H_2O_2 100% degradation was seen after 2.5 hrs. In Photo-Fenton reaction, the oxidant concentration is directly proportional to the number of hydroxyl radicals generated and thus increase with the H_2O_2 concentration. Saturation was attained at 1M H_2O_2: this proves that present urchin coating follows Photo-Fenton reaction for dye degradation.

4.5 Conclusion

Hierarchical 3D Co_3O_4 urchin-like particles have been synthesized in two ways: 1) PLD followed by thermal oxidation, and 2) wet-chemistry hydrothermal procedure.

XRD, Raman, and HR-TEM analysis show that PLD urchin-like particles are developed by NWs (diameter: 30-60 nm and length 1-3 μm) growing radially from the surface of as deposited particulates, after heat treatment at 600 ^oC in air. These NWs are composed of pure Co_3O_4 phase. Mechanisms governing PLD urchin are tentatively attributed to stress induced growth process caused by difference in the thermal expansion coefficient in the core-shell structure of the particulates. NPs of cobalt oxide formed during initial stage of phase separation act as nucleating sites for the NWs growth and Co provided by the core sustains growth of NWs by outward diffusion-oxidation process. The stress induced growth of NWs is evident from the extrusion marks on the surface of the NW. In case of wet-chemistry hydrothermal synthesis, the urchin-like particles are hollow and the structure is held together by the radially oriented nanorods (40-150 nm, made by assembled Co_3O_4 NPs of size 10-30 nm). The efficiency of these urchin-like nanostructures in photocatalysis was examined and compared by degradation of methylene blue dye via a photo-Fenton reaction in presence of H_2O_2 and visible light. PLD nanostructures displayed significantly higher (~5 times) degradation rates when compared to chemically synthesized urchins: the former requires only 2.5 hrs for complete dye degradation as compared to the latter degrading 80 % of dye in 8 hrs. High surface area, enhanced stability against agglomeration, polycrystalline nature of the NWs, porous surface, and superior adhesion, are responsible for the enhanced photocatalytic activity of Co_3O_4 PLD urchins. Reusability tests also proved the robust nature of the PLD urchins.

Chapter 5

Carbon Monoxide (CO) Oxidation by Co_3O_4 Nano Particles Assembled Thin films prepared by Pulsed Laser Deposition

> *“No problem can be solved from the same level of consciousness that created it.”*
> *"Technological progress is like an axe in the hands of a pathological criminal."*
> *Albert Einstein…*

5.1 Introduction

Air pollution occurs in many forms but can generally be thought of as gaseous and particulate contaminants that are present in the earth's atmosphere. *Gaseous pollutants* include sulfur dioxide (SO_2), nitrogen oxides (NO_x), ozone (O_3), carbon monoxide (CO), volatile organic compounds (VOC), hydrogen sulfide (H_2S), hydrogen fluoride (HF), and various gaseous forms of metals. These pollutants are emitted from large stationary sources such as fossil fuel fired power plants, smelters, industrial boilers, petroleum refineries, and manufacturing facilities. They are corrosive to various materials which causes damage to cultural resources, can cause injury to ecosystems and organisms, aggravate respiratory diseases, and reduce visibility. In this chapter we will discuss about one of the pollutants “CO”.

Toxic character of CO, which is produced in large amounts from various sources, prompted early research into strategies to oxidize it at low temperatures with reactive forms of oxygen. The development of catalytic converters led to an extraordinary high number of publications on metal catalysts during the last fifty years. Due to the increasing price of noble metals and to remarkable progresses in oxide catalyst syntheses, catalytic oxidation of CO over the oxide catalysts has recently gained an interest, and some oxides are known to present remarkable catalytic activity in comparison with noble metal catalysts. The present chapter covers the basic introduction of CO, properties, oxidation mechanisms of CO and literature over heterogeneous catalyst materials regarding noble metals and oxides. We stated here use of Cobalt oxide (Co_3O_4) nano particles (NPs) assembled coatings prepared by Pulsed laser deposition (PLD) as economical, efficient and stable heterogeneous catalyst for CO oxidation with an indigenous CO oxidation setup built in our lab.

5.1.1 Carbon Monoxide (CO)

CO is a colorless, odorless gas with a melting point of -205.02 °C and boiling point of -191.5 8 °C[161]. Due to its high affinity with hemoglobin, it becomes a very toxic gas to humans and animals. Long-term exposure should not exceed 25 ppm in 8 h or 50 ppm in 4 h, whereas more and more pronounced detrimental effects are observed above this limit up to the lethal concentration of around 650–700 ppm [162].

Huge amounts of carbon monoxide are emitted in the world (1.09 billion tons in 2000), mainly from transportation, power plants, and industrial and domestic activities [100]. Carbon monoxide is also a precursor of ground-level ozone, which can trigger serious respiratory problems. It is not very soluble in water (23mg $L^{-1}H_2O$), which limits its elimination from air by aqueous treatments. All of these reasons render oxidation into CO_2 is a major solution to CO reduction in air de-pollution treatments.

Carbon monoxide is also a highly flammable gas; its combustion in air can occur between 12 and 75 vol %[163]. However in most cases, CO concentration in polluted air is much lower, typically in the 50–50000ppm range, which means that homogeneous CO combustion is virtually impossible. To achieve CO elimination, it is necessary to catalyze its oxidation. One of the roles of the catalyst is to concentrate the pollutant at its surface, which allows the oxidation reaction to proceed at a sufficient rate.

5.1.2 CO oxidation

The development of catalytic converters in the 1970s in the United States and in the 1990s in Europe highlighted the exceptional activity of noble metals (Pt, Pd, Rh) for CO oxidation[164-167] and the specific role of oxides with a high oxygen storage capacity (OSC) to allow the metal to continue to work in cycled conditions[164, 168]. However, due to the increasing price of noble metals and to remarkable progresses in oxide syntheses, catalytic oxidation of carbon monoxide over oxide catalysts has recently gained in interest. In addition, CO oxidation can be considered an interesting probe reaction for oxide surface characterization.

5.1.3 CO oxidation over Noble metals and Transition Metal oxides

CO is a molecule with three resonance structures that can explain the exceptional adsorption properties and reactivity of this molecule on oxide and metal surfaces:

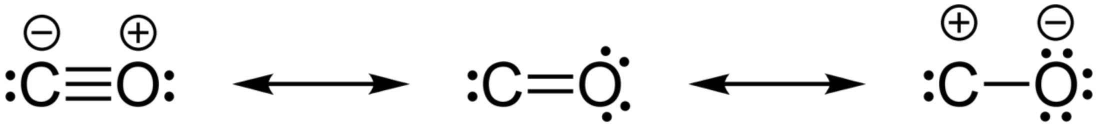

Carbon and oxygen together have a total of 10 valence electrons in carbon monoxide. To satisfy the octet rule for the carbon, the two atoms form a triple bond, with six shared electrons in three bonding molecular orbitals. Since four of the shared electrons come from the oxygen atom and only two from carbon, one bonding orbital is occupied by two electrons from oxygen, forming a dative or dipolar bond. This causes a C←O polarization of the molecule, with a small negative charge on carbon and a small positive charge on oxygen (left). The other two bonding orbitals are each occupied by one electron from carbon and one from oxygen, forming (polar) covalent bonds with a reverse C→O polarization, since oxygen is more electronegative than carbon. If carbon monoxide acts as a ligand, the polarity of the dipole may reverse with a net negative charge on the oxygen end (right) [100, 169].

CO acts as a electron donor, through the 5 s orbital mainly localized on C, and as a π acceptor, through the anti-bonding 2π* orbital. CO can be coordinated to one (linear species) or several metal atoms (bridged species). According to Sheppard and Nguyen, five spectral ranges of CO adsorption bands can be detected[170, 171].

- ν_{CO} =1700–1800 cm_1; CO bonded to 4 metal atoms
- ν_{CO} =1800–1920 cm_1; CO bonded to 3 metal atoms
- ν_{CO} =1860–2000 cm_1; CO bonded to 2 metal atoms
- ν_{CO} =2000–2130 cm_1; linear (or atop) adsorbed species
- ν_{CO} =2130–2200 cm_1; CO bonded to ionic species of metal

For given material, the exact position of the IR bonds depends on the *nature of the metal site and on the particle size and morphology and also on the support* [169, 171].

Catalytic oxidation of carbon monoxide (CO) to carbon dioxide (CO_2) is of great importance in many applications such as air purification, automotive, industrial emission control, close cycle CO_2 lasers and CO gas sensors [172-176]. Removing trace amounts of CO from H_2 powered polymer electrolyte membrane fuel cells (PEMFCs), is of high importance in on-board and portable applications. CO is highly poisonous to Pt anodes and reduces the performance of the PEMFCs [177]. To achieve all these requirements, highly active, stable and low temperature CO oxidation catalyst is an important research topic.

Low-temperature oxidation of CO is perhaps the most extensively studied reaction in the history of heterogeneous catalysis. Hopcalite catalysts (mixtures of manganese and copper oxides) were originally developed for purifying air in submarines, but they were not especially active at ambient temperatures and are also deactivated by the presence of moisture [175, 176]. Noble metal catalysts, on the other hand, are water tolerant but usually require temperatures above 100 °C for efficient operation [178, 179]. Gold exhibits high activity at low temperatures and superior stability under moisture, but only when deposited in nanoparticulate form on base transition-metal oxides[171]. Other precious metals such as Palladium, Ruthenium, Rhodium [180, 181] were also active for CO oxidation. Supported noble metal catalysts on different substrate materials like Au, Pd, and Pt are well known for catalytic CO oxidation with high activity and stability [177, 180-183]. Moreover, high cost and high sensitivity of these materials has provoked researchers to reduce the using of the noble metals or even to replace them by alternative substitutes.

The developments of active and stable catalysts without noble metals for low-temperature CO oxidation under moderate conditions remain a significant challenge. Transition metal oxide catalysts and mixed metal oxides have gained much attention in recent years as good candidates, because these are less expensive and highly active [184-190]. Among all transitional metal oxides, copper oxide (CuO), nickel oxide (NiO) and cobalt oxide (Co_3O_4) catalysts are active for low temperature CO oxidation [191]. Sometimes these materials exhibit relatively low specific activity. In particular Co_3O_4 has received increasing attention towards CO oxidation at low temperatures [171, 187, 191, 192]. Depending on the preparation routes, and reaction conditions, various morphological Co_3O_4 nano structures showed various activities for CO oxidation also [110, 171, 191, 192].

The aim of this chapter involves the synthesis of NPs assembled coatings of Co_3O_4 catalysts by PLD, with detailed characterization and oxidation of CO at various temperatures in an indigenously built apparatus for CO oxidation. First, design, calibration of the CO oxidation set up discussed and then Co_3O_4 catalyst coatings were studied for CO oxidation.

5.1.4 CO oxidation mechanism over Co_3O_4

Co_3O_4 has a spinel structure containing Co^{3+} in an octahedral coordination and Co^{2+} in a tetrahedral coordination (fig 5.1a). The former is regarded as the active site for CO oxidation (fig 5.1 b-d, clearly visible), whereas the latter is almost inactive [171], because CO binds to the Co^{3+} site and then glides toward oxygen forming a surface CO complex with final formation of CO_2 (fig 5.1e). The oxygen vacancy is restored by gas phase oxygen [171] and [193]. The catalytic activity for CO oxidation on Co_3O_4 is related to the number of the active sites on the surface and it was reported that different exposed planes with different shapes show variation in number of active sites and stability conditions for the oxidation [171]. More available active sites, small particle size and the high surface to volume atomic ratio, may be fundamental reasons for the enhanced catalytic activity for CO oxidation.

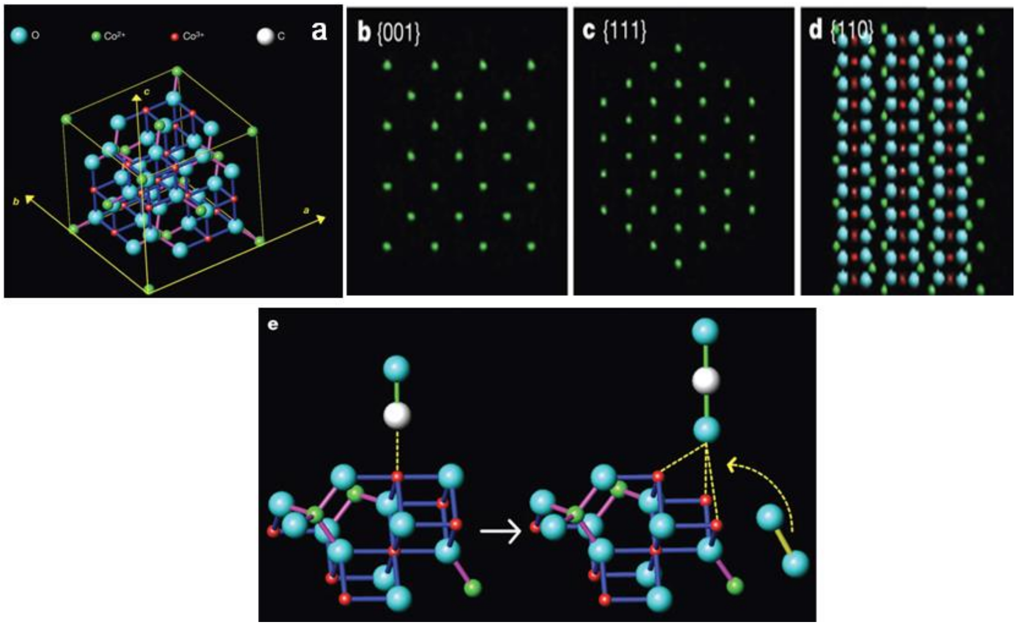

Figure 5.1- (a), Spinel structure of Co_3O_4 crystal, surface atomic configurations in the planes (b), {001}, (c), {111} and (d), {110}, (e), A ball-and-stick model for CO adsorption and oxidation on the active Co^{3+} site[171].

5.2 Co_3O_4 NPs coatings prepared by PLD for CO oxidation

The Co_3O_4 coatings were prepared by PLD using laser fluence $3 J/cm^2$ at substrate temperature of 150 °C as described in the previous chapter (Co_3O_4 NPs assembled coatings used for MB dye degradation).

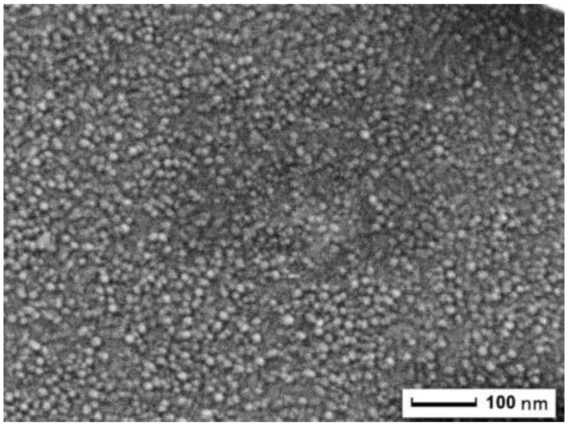

Figure 5.2- SEM micrographs of Co_3O_4 NPs assembled coatings prepared by PLD at substrate temperature of 150 °C with laser fluence of $3 J/cm^2$

The Co_3O_4 coating deposited at 3 J/cm^2 is composed with well circular-shaped NPs with an average size of 10 nm (fig. 5.2). These particles are well distributed and densely arranged on the substrate surface with very low degree of agglomeration. HR-TEM analysis (fig. 4.3) and micron Raman measurements clearly indicated the presence of Co_3O_4 phase (fig. 4.4) as described in the chapter 4.

5.2.1 CO oxidation set up

An experimental apparatus is designed and optimized to study catalytic conversion of CO to CO_2 using thin films of Co_3O_4 coated on glass substrates. In this set-up, an isothermal plug-flow cylindrical reactor was used with a catalyst having ten stainless steel holders to accommodate planar substrates coated with catalyst film. This reactor allows the gas streams to flow perpendicular to the catalyst surface in order to utilize the entire area of the thin film catalyst with minimal pressure drop.

Fig 5.3 a, and b shows the schematic diagram and actual set-up of the CO oxidation apparatus, respectively. The system is mainly made of the stainless steel reaction chamber (reactor) with sample holder, gas cylinders, mass flow controllers, and safety valves for CO gas, tubular furnace, gas chromatographer (GC), on–off valves, stainless steel tubing and a computer to quantify the measured gases.

Gas inlet system: Ar, O_2 and CO gases with specific compositions can be introduced in the reactor by controlling the flow rate of these gases using separate mass flow controllers from MKS. Mass flow controller 1179 B connected to single channel PR 4000B-S read out–set point control with a scale of 200sccm is used for the Ar gas carrier, while two mass flow controllers 1179 B connected to a dual-channel PR 4000B-F read out–set point control with a scale of 20sccm are used for O_2 and CO. Swagelok 6 mm connectors are used at the input and output end of MKS MFC.

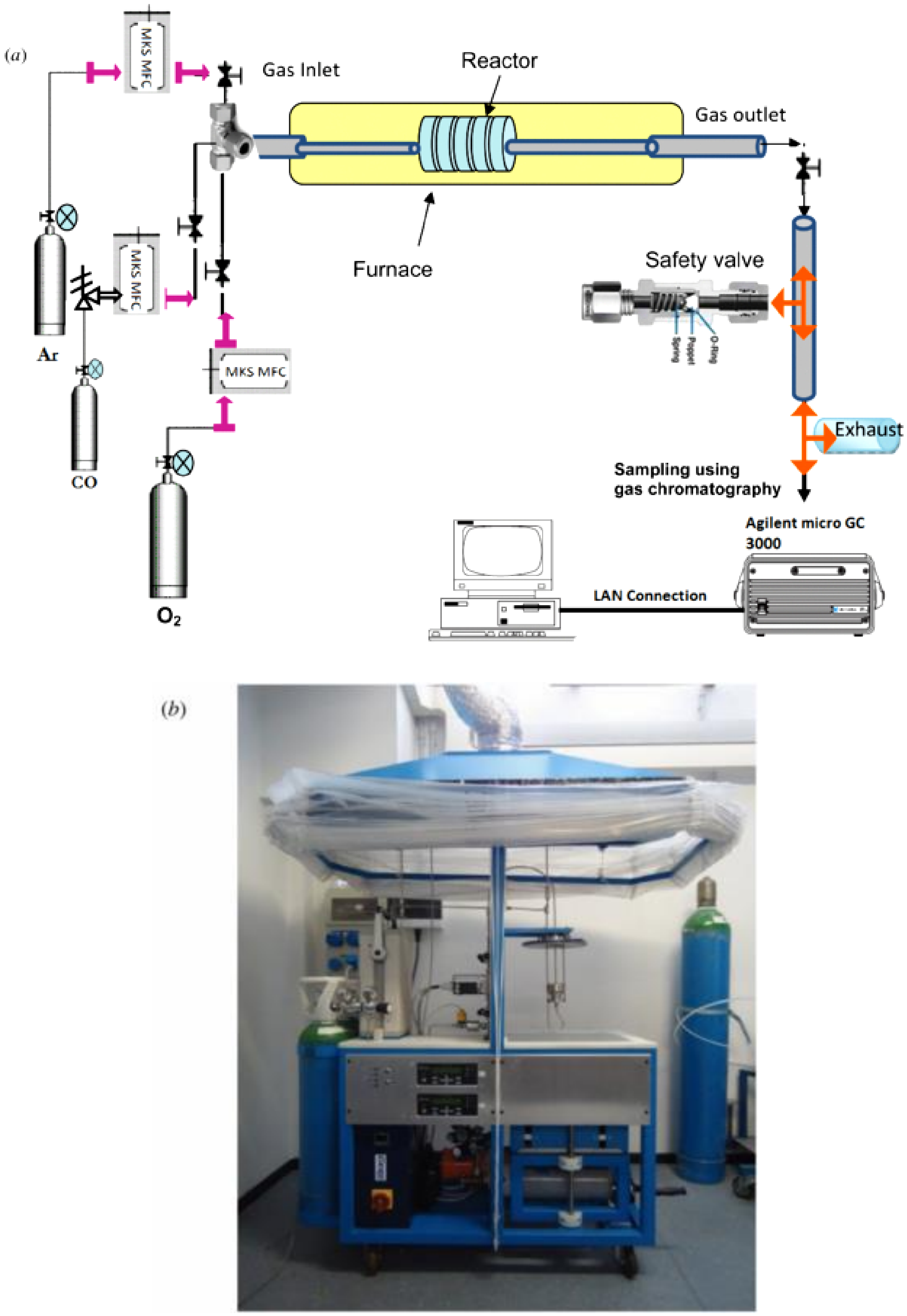

Figure 5.3- (*a*) Schematic diagram and (*b*) actual set-up of the CO oxidation apparatus.

A special safety valve is connected between the principle valve of the CO cylinder and MKS mass flow controller to ensure the safety conditions during the handling of CO. This valve only functions when sufficient argon gas flow is introduced into the reactor. The set gas composition is verified by the GC before introducing in the reactor.

Reaction chamber: The reactor chamber (reactor) was designed and built in a unique way in our laboratory. It is designed in such a way to hold set of some planar samples of size 21 mm × 26 mm. The reactor is cylindrical in shape with a height of 4 cm and a cross-sectional area of 9 cm^2. Within this chamber, a circular sample holder with ten compartments for the samples is stacked one above the other. The glass slides of dimensions 21 mm × 26 mm can be loaded in the reactor as shown in fig 5. 4a, and the gas flow in the reactor is as shown in fig 5.4b. This design of the sample holder and the gas flow mechanism allow the entire surface of the catalyst to be utilized for the CO oxidation reaction. The gas is introduced from the top of the reactor perpendicular to the first glass slide loaded in the reactor. The all-metal sealing of the reaction chamber is ensured by a Cu gasket.

To maintain the temperature during the measurement, the reactor is introduced in the vertically positioned Gerotherm furnace (fig 5.3a) with the help of a pulley system. The heating module consists of oval CrFeAl heating coils which are embedded in a ceramic fiber module. The heating tube of the furnace consists of a 100 mm diameter ceramic tube with a total length of 355 mm with a heating zone 200 mm wide. The temperature program of the furnace is configured using a Eurotherm 3216 temperature controller. A stainless steel plate attached above the reactor is exactly on the top of the furnace to ensure that there is no heat dissipation. This stainless steel plate is constructed with water cooling provision so that there is no heat conduction process in the remaining stainless steel tubing of the system outside the reactor.

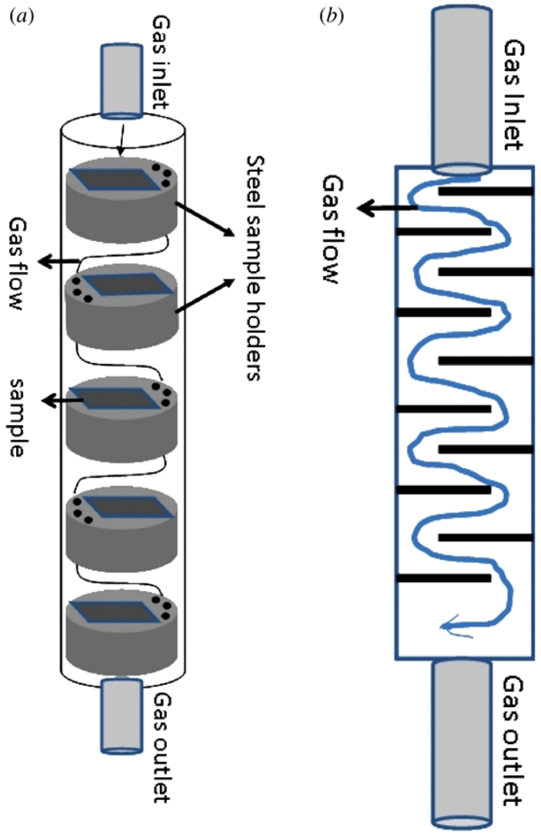

Figure 5.4- (*a*) 3D view and (*b*) side view of the reaction chamber with gaseous flow.

Gas outlet and analysis set-up: The gas coming out of the reactor is connected to the exhaust and micro-GC using a T connector (fig 5.4a). The micro-GC (3000 Agilent) uses self-contained GC modules, each consisting of a heated injector, sample column, reference column, flow control valve and a thermal conductivity detector. The chromatograph equipped with a TDX-01 carbon sieve column, was operated with a column temperature of 110 °C. Gas mixtures are introduced through a 1/16 inch

Swagelok connection to the inlet on the front panel. Ar is used as a carrier gas for micro-GC 3000. A separate Ar cylinder is used in order to connect it as carrier gas to the GC. The instrument is first calibrated for 5% CO, 5% O_2 and 5% CO_2 in Ar. The micro-GC is connected by a standard LAN cable to a computer. The Agilent 3000 control software handles all experimental settings, data collection and data analysis. In order to protect the GC, a safety valve (SS-6C-MM-1/3) is connected between the outlet and the GC with a T connector. This valve opens automatically if the pressure of gas at the outlet increases over 20 mbar above atmospheric pressure. The outlet of this safety valve is directly connected to the exhaust.

The entire system of CO oxidation is enclosed in a hood with appropriate aspiratory conditions. The complete system is interlocked such that all the electrical devices (flow controller, furnace, safety valves, GC etc) will be operational only when the aspiration hood is functioning.

5.2.2 CO oxidation measurements

This apparatus was tested for CO to CO_2 conversion in the presence of Co_3O_4 NPs coating at various temperatures. The Co_3O_4 catalyst was synthesized by PLD (chapter 2, section 2.3.2) in the form of thin films over a glass substrate of size 21 mm × 25 mm. 10 such films were prepared and loaded in the slots of the sample holder in the reactor. The total weight of the catalyst was around 3 mg. After sealing with the Cu gasket, the reactor was lowered in the furnace with the pulley. Ar gas was flushed through the reactor for 1 h to remove ambient gas. This was verified by measuring the O_2 gas signal in the micro-GC. Later, the furnace was heated up to 150 °C with a heating rate of 4 °C min^{-1} and maintained for 30 min in order to remove any moisture adsorbed on the surface and the furnace was cooled to room temperature.

5.2.3 Effect of temperature on CO conversion

A gas mixture of 1 vol. % CO (0.3 ml min^{-1}), 20 vol. % O_2 (6 ml min^{-1}) and 79 vol. % of Ar (27.3 ml min^{-1}) with a total flow rate of 30 ml min^{-1} was introduced into the reactor using the mass flow controllers: the flow rate corresponds to a high gas hourly space velocity of 692 L g^{-1} cat^{-1} h^{-1}. Once the established values of CO and O_2 were reached, the temperature was set to the required value and then catalytic activity was tested by measuring the inlet (CO, O_2) and out let (CO, O_2, and CO_2) with micro-GC. The quantitative analysis is performed by numerically calculating the area under the micro-GC peaks, to determine the concentration of gases with respect to the calibration curve created before the start of the measurement with known concentration gases.

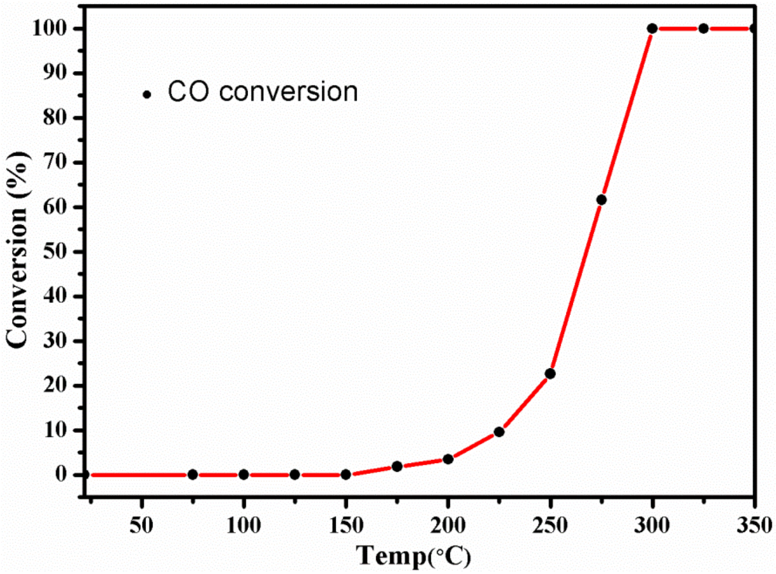

Figure 5.5- Percentage of CO conversion measured at various temperatures for Co_3O_4 thin films prepared by PLD.

The amount of CO conversion was studied by decreasing, step-wise, the isothermal conditions starting from 300 to 75 °C with a step of 25 °C (fig 5.5) and collecting each data 30 min after the set temperature was stabilized. This clearly shows that at 300 °C complete oxidation of CO is obtained on the catalyst thin film. At 250 °C the catalytic activity was tested for longer times of operation and is reported in fig 5.6.

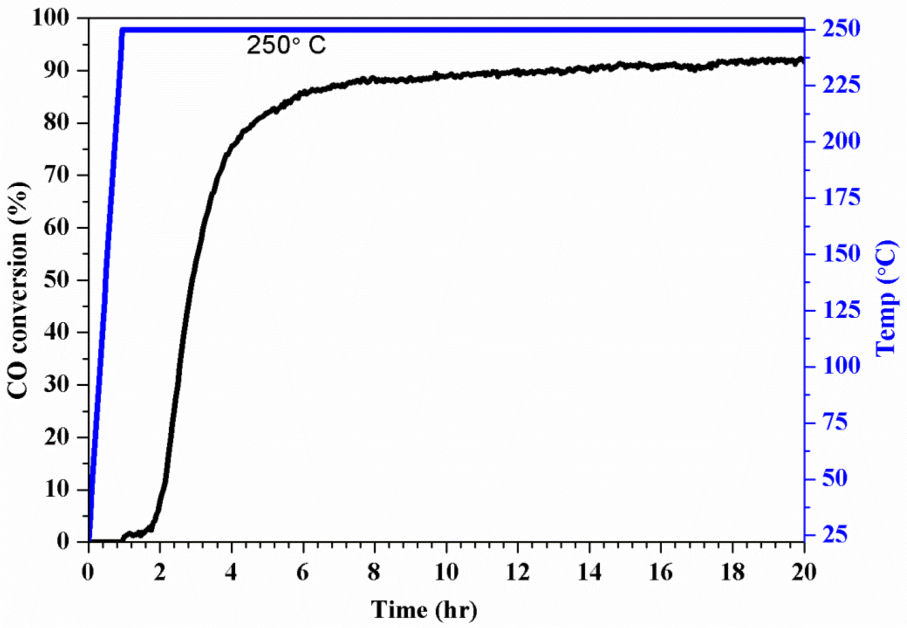

Figure 5.6- CO conversion catalytic activity, at 250 °C, of Co_3O_4 thin films prepared by PLD

It can be seen that at 250 °C, above 90% of CO conversion is achieved and this efficiency is maintained for a long period of time (testing made up to 100 h). This proves a good stability with the present NPs assembled Co_3O_4 coatings. Most importantly, the catalytic activity remains unchanged for three runs of reaction. The effect of decreasing temperature (from 250 °C to 175 °C) on CO conversion was also investigated and the respective percentage conversion values are reported in table 5.1. From the table it is clearly visible that CO conversion is proportional to the temperature. Since it is well known that the experimental parameters, such as pre-heating treatment, amount of catalyst, CO concentration, and flow rate are crucial for CO conversion, thus representing the conversion of CO in terms of specific rate (μmol/s/g_{cat}) [185] and [194] offers a more appropriate means to compare the catalytic activity of different catalysts. It is observed that the specific rate of CO conversion is proportional to temperature of the reaction. At 250 °C, the specific rate of reaction is about 79.83 μmol/g_{cat}/s and the corresponding specific rates for different temperatures are shown in the table 5.1.

Table 5.1- Percentage conversion and specific rates (μmol/g_{cat}/s) for CO oxidation performed at different temperatures in presence of Co_3O_4NPs assembled coating (2.6 mg) prepared by PLD (3 J/cm^2).

S. No.	*Temp. (°C)*	*Conversion (%)*	*Specific rate (μmol/g_{cat}/s)*
1	250	93	79.83
2	225	63	54.08
3	200	30	25.75
4	175	06	5.15

5.3 Conclusions

This PLD coating of Co_3O_4 showed above 90% conversion efficiency of CO to CO_2 at 250 °C with very high specific rate. Small average size (5–20 nm), narrow size distribution, perfect spherical shape, low degree of agglomeration and nanocrystalline phase are the main factors responsible for the enhanced catalytic activity of the Co_3O_4 NPs assembled coating synthesized by PLD. The total conversion of CO to CO_2 occurs in the range of 250-300 °C. In spite of little higher temperature of CO conversion, the proposed PLD coatings shows very high stability towards the activity for very longer times. This is very appreciable and our further immediate step will be to reduce the temperature of CO oxidation maintaining the catalytic for longer times. Finally this will be good step to achieve better designs and materials towards sustainable CO oxidation.

Chapter 6

Conclusion and future work

6.1 Conclusions

H_2 production from NH_3BH_3 and $NaBH_4$ was studied through the hydrolysis reaction. Hydrolysis was carried with the use of highly active, low cost Co–B powder to generate H_2 from NH_3BH_3. With Co-B nanoparticles supported over various mesoporous silica particles MCM-41, FSM-16 and SBA-15, the catalytic activity was highly enhanced with respect to unsupported Co-B. The role of each porous material in the enhanced catalytic activity was investigated with various characterization techniques. After that, Co_3O_4 nano particles assembled coating (NPAC) prepared by pulsed laser deposition (PLD) as immobilized catalyst was tested for hydrolysis of $NaBH_4$. Co-B@SBA-15 silica was found to be most active catalyst that produces the expected amount of H_2 gas (1900 ml/min/g of Co-B catalyst), a value that is higher than that measured with Co-B@MCM-41 (~1150 ml/min/g of Co-B catalyst), Co-B@FSM-16 (~1200 ml/min/g of Co-B catalyst) and bare Co-B powder catalyst (~360 ml/min/g of Co-B catalyst).

Spinel cobalt oxide (Co_3O_4) coatings prepared by PLD were studied for heterogeneous catalysis in organic pollutants degradation and CO oxidation measurements. The Co_3O_4 coatings in the form of NPs with various sizes were tested for methylene blue dye degradation and showed that with smaller NPs the photocatalytic activity is higher. Then we have developed a new morphological coatings like 3-D hierarchical urchin structures by PLD, followed by thermal oxidation. These structures showed a very excellent activity in methylene blue dye degradation as compared to the nano particle assembled coatings (NPACs) and the same kind of structures prepared by chemical method. The photocatalytic activity of the new form of Co_3O_4 is 5-6 times higher than the Co_3O_4 NPACS and chemically prepared structures of the same. Importantly, the new form of Co_3O_4 is highly stable and reusable for at least 10 times.

The Co_3O_4 NPACs were also used to study the CO oxidation reaction. For that, we have developed an indigenous CO oxidation set up in our lab and the set up was calibrated and optimized. The results obtained here are quite impressive in terms of stability and activity as compared to the powder catalyst reported in the literature.

The highlights of the whole activity is as,

1. Power catalysts are less stable, shows deactivation with time and it is not easy to recover or reuse them. To avoid these problems we have chosen PLD as the best technique to prepare the catalysts in the form of coatings and we proved that this method gives relevant results in various applications as compared to other deposition techniques.
2. The catalyst coatings prepared by PLD are very active, stable and, interestingly, by this method we use only very less amounts of catalyst as compared to all other techniques. Here we can modify the catalyst properties as we require and this technique helps to prepare other morphology structures when combined with simple thermal oxidation process.

6.2 Future work

Most of the efforts in the future can be devoted to improvement and development of new catalyst materials. The results in this thesis provide several lines of research which should be pursued.

- 3-D hierarchical urchin structures prepared by PLD and thermal oxidation will be studied by in-situ and ex-situ X-ray absorption spectroscopy (XAS) analysis combined with imaging techniques to understand the growth mechanism.
- 3-D hierarchical structures of other metal oxides will be studied with doping or without doping. Chemical methods will also be used to prepare the urchin structures and simultaneously search for methodologies to make them stable and active for longer times.
- The 3-D hierarchical structures will be studied for hydrolysis reactions of NH_3BH_3 and $NaBH_4$, for organic pollutants degradation and CO oxidation.
- Since we have seen that the Co_3O_4 coatings exhibit efficient results for hydrolysis, water purification and CO oxidation, now look for the Co_3O_4 NPACs and 3-D urchin structures prepared by PLD for stable and efficient water oxidation measurements.

List of Publications

1. Highly photo-catalytically active hierarchical 3D porous/urchin nanostructured Co_3O_4 coating synthesized by Pulsed Laser Deposition
   R. Edla, N. Patel, M. Orlandi, N. Bazzanella, V. Bello, C. Maurizio, G. Mattei, P. Mazzoldi, A. Miotello, submitted in ***App. Cat. B; Environmental.,*** *2014 in press.*

2. Ruthenium nano particles supported over carbon thin film catalyst synthesized by Pulsed Laser Deposition for hydrogen production from Ammonia Borane.
   R. Fernandes, N. Patel, **R. Edla**, N. Bazzanella, D. C. Kothari, Antonio Miotello, ***App. Cat. B; General., (*** *under review).*

3. Pulsed laser deposition of Co_3O_4 nano-catalysts for Dye degradation and CO oxidation.
   R. Edla, N. Patel, Z. El Koura, R. Fernandes, N. Bazzanella, A. Miotello, ***Appl. Surf. Sci.,*** 302(2013), 105-108.

4. Multilayer films of ITO/TiO_2 co-doped with Vanadium and Nitrogen for efficient photo catalytic water splitting.
   Z. El Koura, N. Patel, **R. Edla**, A. Miotello, ***Int. J. Nanosci. Nanotech.,*** 2014

5. A new apparatus for carbon monoxide oxidation studies performed over thin film catalysts. N. Patel, W. Trupti, R. Fernandes, C. Cestari, D. Avi, N. Bazzanella, **R. Edla**, Z. El. Koura, A. Miotello, ***Meas. Sci. Technol.,*** 24(2013), 125901-12906.

6. Co-B catalyst supported over mesoporous silica for hydrogen production by catalytic hydrolysis of Ammonia Borane: A study on influence of pore structure.
   N. Patel, R. Fernandes, S. Gupta, **R. Edla,** D.C. Kothari, A. Miotello, ***Appl. Cat. B;Environmental,*** 140–141 (2013), 125–132.

7. Superior hydrogen production rate by catalytic hydrolysis of ammonia borane using Co-B nano particles supported over mesoporous silica particles.
   N. Patel, R. Fernandes, **R. Edla**, P.B. Lihitkar, D.C. Kothari, A. Miotello**, *Catal. Commun.,*** 23(2012), 39-42.

Conferences/Summer schools:

- *International Euro-Mediterranean Hydrogen Technologies Conference* **(EmHyTeC-2014),** December, Taormina, Italy 2014.
- EMRS (European Materials Research Society-2013) - Spring Meeting, Strasbourg, France, 2013.
- ITPAR (Indo-Trento Programme for Advanced Research-2013), University of Mumbai, Mumbai, India, 2013.
- 11th International Summer School on "Lasers in Materials Science" (SLIMS-2012), Isola di San Servolo, Venice, Italy-2012.

References

[1] wikipedia, http://en.wikipedia.org/wiki/Human_impact_on_the_environment.

[2] U.S.E.I. Administration, International Energy Outlook, 2013.

[3] W.E. Council, World Energy Resources: A Summary, 2013.

[4] IPCC, Fourth Assessment Report: Mitigration of Climate 2007.

[5] J. Hansen, M. Sato, R. Ruedy, K. Lo, D.W. Lea, and M. Medina-Elizade, Global temperature change, Proc. Natl. Acad. Sci.,, 103 (2006) 14288-14293.

[6] F. Petrakopoulou, G. Tsatsaronis, Can Carbon Dioxide Capture and Storage from Power Plants Reduce the Environmental Impact of Electricity Generation?, Energy & Fuels, (2014).

[7] V. Scott, S. Gilfillan, N. Markusson, H. Chalmers, R.S. Haszeldine, Last chance for carbon capture and storage, Nature Clim. Change, 3 (2013) 105-111.

[8] F. Jin, X. Zeng, Z. Jing, H. Enomoto, A Potentially Useful Technology by Mimicking Nature—Rapid Conversion of Biomass and CO_2 into Chemicals and Fuels under Hydrothermal Conditions, Industrial & Engineering Chemistry Research, 51 (2012) 9921-9937.

[9] S.C. Roy, O.K. Varghese, M. Paulose, C.A. Grimes, Toward Solar Fuels: Photocatalytic Conversion of Carbon Dioxide to Hydrocarbons, ACS Nano, 4 (2010) 1259-1278.

[10] H.-J. Freund, G. Meijer, M. Scheffler, R. Schlögl, M. Wolf, CO Oxidation as a Prototypical Reaction for Heterogeneous Processes, Angewandte Chemie International Edition, 50 (2011) 10064-10094.

[11] J.J. West, S.J. Smith, R.A. Silva, V. Naik, Y. Zhang, Z. Adelman, M.M. Fry, S. Anenberg, L.W. Horowitz, J.-F. Lamarque, Co-benefits of mitigating global greenhouse gas emissions for future air quality and human health, Nature Clim. Change, 3 (2013) 885-889.

[12] A. Markandya, B.G. Armstrong, S. Hales, A. Chiabai, P. Criqui, S. Mima, C. Tonne, P. Wilkinson, Public health benefits of strategies to reduce greenhouse-gas emissions: low-carbon electricity generation, The Lancet, 374 2006-2015.

[13] L. Schlapbach, A. Zuttel, Hydrogen-storage materials for mobile applications, Nature, 414 (2001) 353-358.

[14] Y. Song, New perspectives on potential hydrogen storage materials using high pressure, Physical Chemistry Chemical Physics, 15 (2013) 14524-14547.

[15] T.E. Mallouk, Water electrolysis: Divide and conquer, Nat Chem, 5 (2013) 362-363.
[16] M.D. Symes, L. Cronin, Decoupling hydrogen and oxygen evolution during electrolytic water splitting using an electron-coupled-proton buffer, Nat Chem, 5 (2013) 403-409.

[17] E.Y. Marrero-Alfonso, A.M. Beaird, T.A. Davis, M.A. Matthews, Hydrogen Generation from Chemical Hydrides, Industrial & Engineering Chemistry Research, 48 (2009) 3703-3712.

[18] W. Grochala, P.P. Edwards, Thermal Decomposition of the Non-Interstitial Hydrides for the Storage and Production of Hydrogen, Chemical Reviews, 104 (2004) 1283-1316.

[19] M.B. Ley, L.H. Jepsen, Y.-S. Lee, Y.W. Cho, J.M. Bellosta von Colbe, M. Dornheim, M. Rokni, J.O. Jensen, M. Sloth, Y. Filinchuk, J.E. Jørgensen, F. Besenbacher, T.R. Jensen, Complex hydrides for hydrogen storage – new perspectives, Materials Today, 17 (2014) 122-128.

[20] G. Moussa, R. Moury, U.B. Demirci, T. Şener, P. Miele, Boron-based hydrides for chemical hydrogen storage, International Journal of Energy Research, 37 (2013) 825-842.

[21] C.G. Morales-Guio, S.D. Tilley, H. Vrubel, M. Gratzel, X. Hu, Hydrogen evolution from a copper(I) oxide photocathode coated with an amorphous molybdenum sulphide catalyst, Nat Commun, 5 (2014).

[22] L. Liao, Q. Zhang, Z. Su, Z. Zhao, Y. Wang, Y. Li, X. Lu, D. Wei, G. Feng, Q. Yu, X. Cai, J. Zhao, Z. Ren, H. Fang, F. Robles-Hernandez, S. Baldelli, J. Bao, Efficient solar water-splitting using a nanocrystalline CoO photocatalyst, Nat Nano, 9 (2014) 69-73.

[23] S.C. Warren, K. Voïtchovsky, H. Dotan, C.M. Leroy, M. Cornuz, F. Stellacci, C. Hébert, A. Rothschild, M. Grätzel, Identifying champion nanostructures for solar water-splitting, Nat Mater, 12 (2013) 842-849.

[24] P.E. de Jongh, Hydrogen storage: Keeping out the oxygen, Nat Mater, 10 (2011) 265-266.

[25] G.R. B, Hydrogen fuel: Production, transport and storage, CRC Press2008.

[26] N.R.C.a.N.A. E, The Hydrogen Economy: Opportunities, Costs, Barriers, and R&D Needs, The National Academies Press, Washington DC 2004.

[27] C.M. Kalamaras, A.M. Efstathiou, Hydrogen Production Technologies: Current State and Future Developments, Conference Papers in Energy, 2013 (2013) 9.

[28] K. Christopher, R. Dimitrios, A review on exergy comparison of hydrogen production methods from renewable energy sources, Energy & Environmental Science, 5 (2012) 6640-6651.

[29]HydrogenBasics-Production, http://www.fsec.ucf.edu/en/consumer/hydrogen/basics/production.htm.

[30] N.Z. Muradov, T.N. Veziroğlu, From hydrocarbon to hydrogen–carbon to hydrogen economy, International Journal of Hydrogen Energy, 30 (2005) 225-237.

[31] J.D. Holladay, J. Hu, D.L. King, Y. Wang, An overview of hydrogen production technologies, Catalysis Today, 139 (2009) 244-260.

[32] A. T-Raissi, D.L. Block, Hydrogen: automotive fuel of the future, Power and Energy Magazine, IEEE, 2 (2004) 40-45.

[33] U. Sanyal, U.B. Demirci, B.R. Jagirdar, P. Miele, Hydrolysis of Ammonia Borane as a Hydrogen Source: Fundamental Issues and Potential Solutions Towards Implementation, ChemSusChem, 4 (2011) 1731-1739.

[34] U. Eberle, M. Felderhoff, F. Schüth, Chemical and Physical Solutions for Hydrogen Storage, Angewandte Chemie International Edition, 48 (2009) 6608-6630.

[35] B. Sakintuna, F. Lamari-Darkrim, M. Hirscher, Metal hydride materials for solid hydrogen storage: A review, International Journal of Hydrogen Energy, 32 (2007) 1121-1140.

[36] Wikipedia, Fuel cell, http://en.wikipedia.org/wiki/Fuel-cell.

[37] A. Kirubakaran, S. Jain, R.K. Nema, A review on fuel cell technologies and power electronic interface, Renewable and Sustainable Energy Reviews, 13 (2009) 2430-2440.

[38] S. Litster, G. McLean, PEM fuel cell electrodes, Journal of Power Sources, 130 (2004) 61-76.

[39] Y. Wang, K.S. Chen, J. Mishler, S.C. Cho, X.C. Adroher, A review of polymer electrolyte membrane fuel cells: Technology, applications, and needs on fundamental research, Applied Energy, 88 (2011) 981-1007.

[40] M.K. Debe, Electrocatalyst approaches and challenges for automotive fuel cells, Nature, 486 (2012) 43-51.

[41] C.-Y. Lai, B.G. Trewyn, D.M. Jeftinija, K. Jeftinija, S. Xu, S. Jeftinija, V.S.Y. Lin, A Mesoporous Silica Nanosphere-Based Carrier System with Chemically Removable CdS Nanoparticle Caps for Stimuli-Responsive Controlled Release of Neurotransmitters and Drug Molecules, Journal of the American Chemical Society, 125 (2003) 4451-4459.

[42] A. Matsumoto, T. Sasaki, N. Nishimiya, K. Tsutsumi, Thermal stability and hydrophobicity of mesoporous silica FSM-16, Colloids and Surfaces A: Physicochemical and Engineering Aspects, 203 (2002) 185-193.

[43] V. Brahmkhatri, A. Patel, 12-Tungstophosphoric acid anchored to SBA-15: An efficient, environmentally benign reusable catalysts for biodiesel production by esterification of free fatty acids, Applied Catalysis A: General, 403 (2011) 161-172.

[44] W. Stöber, A. Fink, E. Bohn, Controlled growth of monodisperse silica spheres in the micron size range, Journal of Colloid and Interface Science, 26 (1968) 62-69.

[45] T. Warang, N. Patel, R. Fernandes, N. Bazzanella, A. Miotello, Co_3O_4 nanoparticles assembled coatings synthesized by different techniques for photo-degradation of methylene blue dye, Applied Catalysis B: Environmental, 132–133 (2013) 204-211.

[46] X. Rui, H. Tan, D. Sim, W. Liu, C. Xu, H.H. Hng, R. Yazami, T.M. Lim, Q. Yan, Template-free synthesis of urchin-like Co_3O_4 hollow spheres with good lithium storage properties, Journal of Power Sources, 222 (2013) 97-102.

[47]Thinfilmgrowthmodes, http://en.wikipedia.org/wiki/Stranski%E2%80%93Krastanovgrowth.

[48] Thin films, http://en.wikipedia.org/wiki/Thin_film.

[49] A. Miotello, N. Patel, Pulsed laser deposition of cluster-assembled films for catalysis and the photocatalysis relevant to energy and the environment, Applied Surface Science, 278 (2013) 19-25.

[50] C. Zanchetta, B. Paton, G. Guella, A. Miotello, Mesurement Science and Technology, 18 (2007) 21–26.

[51] S.G. Shore, R.W. Parry, The crystalline compund ammonia-borane,1 H_3NBH_3, Journal of the American Chemical Society, 77 (1955) 6084-6085.

[52] T.B. Marder, Will We Soon Be Fueling our Automobiles with Ammonia–Borane?, Angewandte Chemie International Edition, 46 (2007) 8116-8118.

[53] V. Sit, R.A. Geanangel, W.W. Wendlandt, The thermal dissociation of NH_3BH_3, Thermochimica Acta, 113 (1987) 379-382.

[54] Z. Xiong, C.K. Yong, G. Wu, P. Chen, W. Shaw, A. Karkamkar, T. Autrey, M.O. Jones, S.R. Johnson, P.P. Edwards, W.I.F. David, High-capacity hydrogen storage in lithium and sodium amidoboranes, Nat Mater, 7 (2008) 138-141.

[55] H.-L. Jiang, Q. Xu, Catalytic hydrolysis of ammonia borane for chemical hydrogen storage, Catalysis Today, 170 (2011) 56-63.

[56] M. Chandra, Q. Xu, Room temperature hydrogen generation from aqueous ammonia-borane using noble metal nano-clusters as highly active catalysts, Journal of Power Sources, 168 (2007) 135-142.

[57] M. Chandra, Q. Xu, A high-performance hydrogen generation system: Transition metal-catalyzed dissociation and hydrolysis of ammonia–borane, Journal of Power Sources, 156 (2006) 190-194.

[58] J.-M. Yan, X.-B. Zhang, T. Akita, M. Haruta, Q. Xu, One-Step Seeding Growth of Magnetically Recyclable Au@Co Core−Shell Nanoparticles: Highly Efficient Catalyst for Hydrolytic Dehydrogenation of Ammonia Borane, Journal of the American Chemical Society, 132 (2010) 5326-5327.

[59] F. Cheng, H. Ma, Y. Li, J. Chen, $Ni_{1-x}Pt_x$ ($x = 0-0.12$) Hollow Spheres as Catalysts for Hydrogen Generation from Ammonia Borane, Inorganic Chemistry, 46 (2007) 788-794.

[60] J.-M. Yan, X.-B. Zhang, S. Han, H. Shioyama, Q. Xu, Iron-Nanoparticle-Catalyzed Hydrolytic Dehydrogenation of Ammonia Borane for Chemical Hydrogen Storage, Angewandte Chemie International Edition, 47 (2008) 2287-2289.

[61] J.-M. Yan, X.-B. Zhang, S. Han, H. Shioyama, Q. Xu, Synthesis of Longtime Water/Air-Stable Ni Nanoparticles and Their High Catalytic Activity for Hydrolysis of Ammonia−Borane for Hydrogen Generation, Inorganic Chemistry, 48 (2009) 7389-7393.

[62] Ö. Metin, S. Özkar, S. Sun, Monodisperse nickel nanoparticles supported on SiO_2 as an effective catalyst for the hydrolysis of ammonia-borane, Nano Res., 3 (2010) 676-684.

[63] Q. Xu, M. Chandra, Catalytic activities of non-noble metals for hydrogen generation from aqueous ammonia–borane at room temperature, Journal of Power Sources, 163 (2006) 364-370.

[64] P.-Z. Li, K. Aranishi, Q. Xu, ZIF-8 immobilized nickel nanoparticles: highly effective catalysts for hydrogen generation from hydrolysis of ammonia borane, Chemical Communications, 48 (2012) 3173-3175.

[65] A. Baiker, Metallic glasses in heterogeneous catalysis, Faraday Discussions of the Chemical Society, 87 (1989) 239-251.

[66] Z. Wu, S. Ge, Facile synthesis of a Co-B nanoparticle catalyst for efficient hydrogen generation via borohydride hydrolysis, Catalysis Communications, 13 (2011) 40-43.

[67] R. Fernandes, N. Patel, A. Miotello, R. Jaiswal, D.C. Kothari, Dehydrogenation of Ammonia Borane with transition metal-doped Co–B alloy catalysts, International Journal of Hydrogen Energy, 37 (2012) 2397-2406.

[68] R. Fernandes, N. Patel, A. Miotello, R. Jaiswal, D.C. Kothari, Stability, durability, and reusability studies on transition metal-doped Co–B alloy catalysts for hydrogen production, International Journal of Hydrogen Energy, 36 (2011) 13379-13391.

[69] N. Patel, R. Fernandes, A. Miotello, Promoting effect of transition metal-doped Co–B alloy catalysts for hydrogen production by hydrolysis of alkaline $NaBH_4$ solution, Journal of Catalysis, 271 (2010) 315-324.

[70] D.-g. Tong, W. Chu, Y.-y. Luo, H. Chen, X.-y. Ji, Preparation and characterization of amorphous Co-B catalysts with mesoporous structure, Journal of Molecular Catalysis A: Chemical, 269 (2007) 149-157.

[71] N. Patel, R. Fernandes, A. Santini, A. Miotello, Co–B nanoparticles supported on carbon film synthesized by pulsed laser deposition for hydrolysis of ammonia borane, International Journal of Hydrogen Energy, 37 (2012) 2007-2013.

[72] N. Patel, R. Fernandes, N. Bazzanella, A. Miotello, Enhanced hydrogen production by hydrolysis of $NaBH_4$ using "Co-B nanoparticles supported on Carbon film" catalyst synthesized by pulsed laser deposition, Catalysis Today, 170 (2011) 20-26.

[73] P. Martelli, R. Caputo, A. Remhof, P. Mauron, A. Borgschulte, A. Züttel, Stability and Decomposition of $NaBH_4$, The Journal of Physical Chemistry C, 114 (2010) 7173-7177.

[74] J. Lee, K.Y. Kong, C.R. Jung, E. Cho, S.P. Yoon, J. Han, T.-G. Lee, S.W. Nam, A structured Co–B catalyst for hydrogen extraction from $NaBH_4$ solution, Catalysis Today, 120 (2007) 305-310.

[75] U.B. Demirci, P. Miele, Sodium borohydride versus ammonia borane, in hydrogen storage and direct fuel cell applications, Energy & Environmental Science, 2 (2009) 627-637.

[76] J.-H. Wee, K.-Y. Lee, S.H. Kim, Sodium borohydride as the hydrogen supplier for proton exchange membrane fuel cell systems, Fuel Processing Technology, 87 (2006) 811-819.

[77] B.H. Liu, Z.P. Li, A review: Hydrogen generation from borohydride hydrolysis reaction, Journal of Power Sources, 187 (2009) 527-534.

[78] P. Krishnan, T.-H. Yang, W.-Y. Lee, C.-S. Kim, PtRu-$LiCoO_2$—an efficient catalyst for hydrogen generation from sodium borohydride solutions, Journal of Power Sources, 143 (2005) 17-23.

[79] D. Xu, P. Dai, X. Liu, C. Cao, Q. Guo, Carbon-supported cobalt catalyst for hydrogen generation from alkaline sodium borohydride solution, Journal of Power Sources, 182 (2008) 616-620.

[80] D. Zhao, J. Feng, Q. Huo, N. Melosh, G.H. Fredrickson, B.F. Chmelka, G.D. Stucky, Triblock Copolymer Syntheses of Mesoporous Silica with Periodic 50 to 300 Angstrom Pores, Science, 279 (1998) 548-552.

[81] M.S. Ghattas, Cobalt-modified mesoporous FSM-16 silica: Characterization and catalytic study, Microporous and Mesoporous Materials, 97 (2006) 107-113.

[82] K.S.W. Sing, D.H. Everett, R.A.W. Haul, L. Moscou, R.A. Pierotti, J. Rouquerol, T. Siemieniewska, Reporting Physisorption Data for Gas/Solid Systems, Handbook of Heterogeneous Catalysis, Wiley-VCH Verlag GmbH & Co. KGaA2008.

[83] D. Zhao, Q. Huo, J. Feng, B.F. Chmelka, G.D. Stucky, Nonionic Triblock and Star Diblock Copolymer and Oligomeric Surfactant Syntheses of Highly Ordered, Hydrothermally Stable, Mesoporous Silica Structures, Journal of the American Chemical Society, 120 (1998) 6024-6036.

[84] N. Patel, R. Fernandes, A. Miotello, Hydrogen generation by hydrolysis of $NaBH_4$ with efficient Co–P–B catalyst: A kinetic study, Journal of Power Sources, 188 (2009) 411-420.

[85] D.G. Tong, X.L. Zeng, W. Chu, D. Wang, P. Wu, Magnetically recyclable hollow Co–B nanospindles as catalysts for hydrogen generation from ammonia borane, Journal of Materials Science, 45 (2010) 2862-2867.

[86] A. Kantürk Figen, B. Coşkuner, A novel perspective for hydrogen generation from ammonia borane (NH_3BH_3) with Co–B catalysts: "Ultrasonic Hydrolysis", International Journal of Hydrogen Energy, 38 (2013) 2824-2835.

[87] A. Kantürk Figen, M.B. Pişkin, B. Coşkuner, V. İmamoğlu, Synthesis, structural characterization, and hydrolysis of Ammonia Borane (NH_3BH_3) as a hydrogen storage carrier, International Journal of Hydrogen Energy, 38 (2013) 16215-16228.

[88] E.E. Arthur, F. Li, F.W.Y. Momade, H. Kim, Catalytic hydrolysis of ammonia borane for hydrogen generation using cobalt nanocluster catalyst supported on polydopamine functionalized multiwalled carbon nanotube, Energy, 76 (2014) 822-829.

[89] N. Patel, R. Fernandes, G. Guella, A. Miotello, Nanoparticle-assembled Co-B thin film for the hydrolysis of ammonia borane: A highly active catalyst for hydrogen production, Applied Catalysis B: Environmental, 95 (2010) 137-143.

[90] M. Zahmakıran, S. Özkar, Zeolite framework stabilized rhodium(0) nanoclusters catalyst for the hydrolysis of ammonia-borane in air: Outstanding catalytic activity, reusability and lifetime, Applied Catalysis B: Environmental, 89 (2009) 104-110.

[91] S. Akbayrak, S. Gencturk, I. Morkan, S. Ozkar, Rhodium(0) nanoparticles supported on nanotitania as highly active catalyst in hydrogen generation from the hydrolysis of ammonia borane, RSC Advances, 4 (2014) 13742-13748.

[92] S. Basu, A. Brockman, P. Gagare, Y. Zheng, P.V. Ramachandran, W.N. Delgass, J.P. Gore, Chemical kinetics of Ru-catalyzed ammonia borane hydrolysis, Journal of Power Sources, 188 (2009) 238-243.

[93] N. Mohajeri, A. T-Raissi, O. Adebiyi, Hydrolytic cleavage of ammonia-borane complex for hydrogen production, Journal of Power Sources, 167 (2007) 482-485.

[94] C.F. Yao, L. Zhuang, Y.L. Cao, X.P. Ai, H.X. Yang, Hydrogen release from hydrolysis of borazane on Pt- and Ni-based alloy catalysts, International Journal of Hydrogen Energy, 33 (2008) 2462-2467.

[95] Ö. Metin, Ş. Şahin, S. Özkar, Water-soluble poly(4-styrenesulfonic acid-co-maleic acid) stabilized ruthenium(0) and palladium(0) nanoclusters as highly active catalysts in hydrogen generation from the hydrolysis of ammonia–borane, International Journal of Hydrogen Energy, 34 (2009) 6304-6313.

[96] H.-B. Dai, L.-L. Gao, Y. Liang, X.-D. Kang, P. Wang, Promoted hydrogen generation from ammonia borane aqueous solution using cobalt–molybdenum–boron/nickel foam catalyst, Journal of Power Sources, 195 (2010) 307-312.

[97] F. Durap, M. Zahmakıran, S. Özkar, Water soluble laurate-stabilized ruthenium(0) nanoclusters catalyst for hydrogen generation from the hydrolysis of ammonia-borane: High activity and long lifetime, International Journal of Hydrogen Energy, 34 (2009) 7223-7230.

[98] H. Li, H. Yang, H. Li, Highly active mesoporous Co–B amorphous alloy catalyst for cinnamaldehyde hydrogenation to cinnamyl alcohol, Journal of Catalysis, 251 (2007) 233-238.

[99] H. Li, X. Chen, M. Wang, Y. Xu, Selective hydrogenation of cinnamaldehyde to cinnamyl alcohol over an ultrafine Co-B amorphous alloy catalyst, Applied Catalysis A: General, 225 (2002) 117-130.

[100] P. Krishnan, S.G. Advani, A.K. Prasad, Cobalt oxides as Co_2B catalyst precursors for the hydrolysis of sodium borohydride solutions to generate hydrogen for PEM fuel cells, International Journal of Hydrogen Energy, 33 (2008) 7095-7102.

[101] A.M. Ozerova, V.I. Simagina, O.V. Komova, O.V. Netskina, G.V. Odegova, O.A. Bulavchenko, N.A. Rudina, Cobalt borate catalysts for hydrogen production via hydrolysis of sodium borohydride, Journal of Alloys and Compounds, 513 (2012) 266-272.

[102] P. Krishnan, K.-L. Hsueh, S.-D. Yim, Catalysts for the hydrolysis of aqueous borohydride solutions to produce hydrogen for PEM fuel cells, Applied Catalysis B: Environmental, 77 (2007) 206-214.

[103] V.I. Simagina, O.V. Komova, A.M. Ozerova, O.V. Netskina, G.V. Odegova, D.G. Kellerman, O.A. Bulavchenko, A.V. Ishchenko, Cobalt oxide catalyst for hydrolysis of sodium borohydride and ammonia borane, Applied Catalysis A: General, 394 (2011) 86-92.

[104] T.L. Pfeil, T.L. Pourpoint, L.J. Groven, Effects of crystallinity and morphology of solution combustion synthesized Co_3O_4 as a catalyst precursor in hydrolysis of sodium borohydride, International Journal of Hydrogen Energy, 39 (2014) 2149-2159.

[105] S.C. Amendola, S.L. Sharp-Goldman, M.S. Janjua, N.C. Spencer, M.T. Kelly, P.J. Petillo, M. Binder, A safe, portable, hydrogen gas generator using aqueous borohydride solution and Ru catalyst, International Journal of Hydrogen Energy, 25 (2000) 969-975.

[106] N. Patel, R. Fernandes, G. Guella, A. Kale, A. Miotello, B. Patton, C. Zanchetta, P.M. Ossi, V. Russo, Pulsed-laser deposition of nanostructured Pd/C thin films: A new entry into metal-supported catalysts for hydrogen producing reactions, Applied Surface Science, 254 (2007) 1307-1311.

[107] N. Patel, A. Miotello, V. Bello, Pulsed Laser Deposition of Co-nanoparticles embedded on B-thin film: A very efficient catalyst produced in a single-step process, Applied Catalysis B: Environmental, 103 (2011) 31-38.

[108] N. Patel, G. Guella, A. Kale, A. Miotello, B. Patton, C. Zanchetta, L. Mirenghi, P. Rotolo, Thin films of Co–B prepared by pulsed laser deposition as efficient catalysts in hydrogen producing reactions, Applied Catalysis A: General, 323 (2007) 18-24.

[109] N. Patel, R. Fernandes, G. Guella, A. Kale, A. Miotello, B. Patton, C. Zanchetta, Structured and Nanoparticle Assembled Co−B Thin Films Prepared by Pulsed Laser Deposition: A Very Efficient Catalyst for Hydrogen Production, The Journal of Physical Chemistry C, 112 (2008) 6968-6976.

[110] R. Edla, N. Patel, Z. El Koura, R. Fernandes, N. Bazzanella, A. Miotello, Pulsed laser deposition of Co_3O_4 nanocatalysts for dye degradation and CO oxidation, Applied Surface Science, 302 (2014) 105-108.

[111] W.H. Perkin, LXXIV.-On mauveine and allied colouring matters, Journal of the Chemical Society, Transactions, 35 (1879) 717-732.

[112] H.A. Boyter, Environmental legislations USA. In R. M. Christie (Ed.), Environmental aspects of textile dyeing. Woodhead, Cambridge, England, (2007).

[113] K. Singh, S. Arora, Removal of Synthetic Textile Dyes From Wastewaters: A Critical Review on Present Treatment Technologies, Critical Reviews in Environmental Science and Technology, 41 (2011) 807-878.

[114] M. Stoyanova, S. Christoskova, Catalytic degradation of methylene blue in aqueous solutions over Ni- and Co- oxide systems, cent.eur.j.chem., 9 (2011) 1000-1007.

[115] U.G. Akpan, B.H. Hameed, Parameters affecting the photocatalytic degradation of dyes using TiO_2-based photocatalysts: A review, Journal of Hazardous Materials, 170 (2009) 520-529.

[116] M. Ahmad, N. Ahmad, O. Bello, Adsorptive Removal of Malachite Green Dye Using Durian Seed-Based Activated Carbon, Water Air Soil Pollut, 225 (2014) 1-18.

[117] K.P. Singh, D. Mohan, S. Sinha, G.S. Tondon, D. Gosh, Color Removal from Wastewater Using Low-Cost Activated Carbon Derived from Agricultural Waste Material, Industrial & Engineering Chemistry Research, 42 (2003) 1965-1976.

[118] A.G. Espantaleón, J.A. Nieto, M. Fernández, A. Marsal, Use of activated clays in the removal of dyes and surfactants from tannery waste waters, Applied Clay Science, 24 (2003) 105-110.

[119] M.J. Avena, M.M. Mariscal, C.P. De Pauli, Proton binding at clay surfaces in water, Applied Clay Science, 24 (2003) 3-9.

[120] G.W. Beall, The use of organo-clays in water treatment, Applied Clay Science, 24 (2003) 11-20.

[121] K. Sarayu, S. Sandhya, Current Technologies for Biological Treatment of Textile Wastewater–A Review, Appl Biochem Biotechnol, 167 (2012) 645-661.

[122] S. Wang, Y. Peng, Natural zeolites as effective adsorbents in water and wastewater treatment, Chemical Engineering Journal, 156 (2010) 11-24.

[123] S. Babel, T.A. Kurniawan, Low-cost adsorbents for heavy metals uptake from contaminated water: a review, Journal of Hazardous Materials, 97 (2003) 219-243.

[124] J. Zhang, K.-H. Lee, L. Cui, T.-s. Jeong, Degradation of methylene blue in aqueous solution by ozone-based processes, Journal of Industrial and Engineering Chemistry, 15 (2009) 185-189.

[125] Q. Zhuo, H. Ma, B. Wang, F. Fan, Degradation of methylene blue: Optimization of operating condition through a statistical technique and environmental estimate of the treated wastewater, Journal of Hazardous Materials, 153 (2008) 44-51.

[126] S. Ahmed, M.G. Rasul, R. Brown, M.A. Hashib, Influence of parameters on the heterogeneous photocatalytic degradation of pesticides and phenolic contaminants in wastewater: A short review, Journal of Environmental Management, 92 (2011) 311-330.

[127] J.-M. Herrmann, Heterogeneous photocatalysis: fundamentals and applications to the removal of various types of aqueous pollutants, Catalysis Today, 53 (1999) 115-129.

[128] R. Bauer, G. Waldner, H. Fallmann, S. Hager, M. Klare, T. Krutzler, S. Malato, P. Maletzky, The photo-fenton reaction and the TiO_2/UV process for waste water treatment − novel developments, Catalysis Today, 53 (1999) 131-144.

[129] T. Warang, N. Patel, A. Santini, N. Bazzanella, A. Kale, A. Miotello, Pulsed laser deposition of Co_3O_4 nanoparticles assembled coating: Role of substrate temperature to tailor disordered to crystalline phase and related photocatalytic activity in degradation of methylene blue, Applied Catalysis A: General, 423–424 (2012) 21-27.

[130] J.H. Ramirez, C.A. Costa, L.M. Madeira, G. Mata, M.A. Vicente, M.L. Rojas-Cervantes, A.J. López-Peinado, R.M. Martín-Aranda, Fenton-like oxidation of Orange II solutions using heterogeneous catalysts based on saponite clay, Applied Catalysis B: Environmental, 71 (2007) 44-56.

[131] S.K. Ling, S. Wang, Y. Peng, Oxidative degradation of dyes in water using Co^{2+}/H_2O_2 and Co^{2+}/peroxymonosulfate, Journal of Hazardous Materials, 178 (2010) 385-389.

[132] Z. Zhang, J. Hao, W. Yang, B. Lu, X. Ke, B. Zhang, J. Tang, Porous Co_3O_4 Nanorods–Reduced Graphene Oxide with Intrinsic Peroxidase-Like Activity and Catalysis in the Degradation of Methylene Blue, ACS Applied Materials & Interfaces, 5 (2013) 3809-3815.

[133] V. Pralong, J.B. Leriche, B. Beaudoin, E. Naudin, M. Morcrette, J.M. Tarascon, Electrochemical study of nanometer Co_3O_4, Co, $CoSb_3$ and Sb thin films toward lithium, Solid State Ionics, 166 (2004) 295-305.

[134] Y. Wang, Z.-W. Fu, Q.-Z. Qin, A nanocrystalline Co_3O_4 thin film electrode for Li-ion batteries, Thin Solid Films, 441 (2003) 19-24.

[135] Y. Ding, L. Zhu, A. Huang, X. Zhao, X. Zhang, H. Tang, A heterogeneous Co_3O_4-Bi_2O_3 composite catalyst for oxidative degradation of organic pollutants in the presence of peroxymonosulfate, Catalysis Science & Technology, 2 (2012) 1977-1984.

[136] F. Švegl, B. Orel, I. Grabec-Švegl, V. Kaučič, Characterization of spinel Co_3O_4 and Li-doped Co_3O_4 thin film electrocatalysts prepared by the sol–gel route, Electrochimica Acta, 45 (2000) 4359-4371.

[137] M.E. Donders, H.C.M. Knoops, M.C.M. van, W.M.M. Kessels, P.H.L. Notten, Remote Plasma Atomic Layer Deposition of Co_3O_4 Thin Films, Journal of The Electrochemical Society, 158 (2011) G92-G96.

[138] J. Wöllenstein, M. Burgmair, G. Plescher, T. Sulima, J. Hildenbrand, H. Böttner, I. Eisele, Cobalt oxide based gas sensors on silicon substrate for operation at low temperatures, Sensors and Actuators B: Chemical, 93 (2003) 442-448.

[139] V. Balouria, S. Samanta, A. Singh, A.K. Debnath, A. Mahajan, R.K. Bedi, D.K. Aswal, S.K. Gupta, Chemiresistive gas sensing properties of nanocrystalline Co_3O_4 thin films, Sensors and Actuators B: Chemical, 176 (2013) 38-45.

[140] C. Guyon, A. Barkallah, F. Rousseau, K. Giffard, D. Morvan, M. Tatoulian, Deposition of cobalt oxide thin films by plasma-enhanced chemical vapour deposition (PECVD) for catalytic applications, Surface and Coatings Technology, 206 (2011) 1673-1679.

[141] S.C. Singh, H. Zeng, Nanomaterials and Nanopatterns Based on Laser Processing: A Brief Review on Current State of Art, Science of Advanced Materials, 4 (2012) 368-390.

[142] N. Patel, A. Santini, V. Bello, G. Mattei, A. Miotello, Cobalt/cobalt oxide nanoparticles-assembled coatings with various morphology and composition synthesized by pulsed laser deposition, Surface and Coatings Technology, 235 (2013) 784-791.

[143] J. Perrière, C. Boulmer-Leborgne, R. Benzerga, S. Tricot, Nanoparticle formation by femtosecond laser ablation, Journal of Physics D: Applied Physics, 40 (2007) 7069-7076.

[144] E. Millon, J. Perrière, R.M. Défourneau, D. Défourneau, O. Albert, J. Etchepare, Femtosecond pulsed-laser deposition of $BaTiO_3$, Applied Physics A: Materials Science and Processing, 77 (2003) 73-80.

[145] I. Lorite, J.J. Romero, J.F. Fernández, Effects of the agglomeration state on the Raman properties of Co_3O_4 nanoparticles, Journal of Raman Spectroscopy, 43 (2012) 1443-1448.

[146] V.G. Hadjiev, M.N. Iliev, I.V. Vergilov, The Raman spectra of Co_3O_4, Journal of Physics C: Solid State Physics, 21 (1988) L199.

[147] J. Hao, W. Yang, Z. Zhang, S. Pan, B. Lu, X. Ke, B. Zhang, J. Tang, Hierarchical flower-like $Co_{3-x}Fe_xO_4$ ferrite hollow spheres: facile synthesis and catalysis in the degradation of methylene blue, Nanoscale, 5 (2013) 3078-3082.

[148] Y. Hu, Z. Li, Y. Sun, Enhanced photocatalysis by hybrid hierarchical assembly of plasmonic nanocrystals with high surface areas, Catalysis Today, 225 (2014) 177-184.

[149] H. Ceylan, C. Ozgit-Akgun, T.S. Erkal, I. Donmez, R. Garifullin, A.B. Tekinay, H. Usta, N. Biyikli, M.O. Guler, Size-controlled conformal nanofabrication of biotemplated three-dimensional TiO_2 and ZnO nanonetworks, Sci. Rep., 3 (2013).

[150] S. Luo, F. Chai, L. Zhang, C. Wang, L. Li, X. Liu, Z. Su, Facile and fast synthesis of urchin-shaped $Fe_3O_4@Bi_2S_3$ core-shell hierarchical structures and their magnetically recyclable photocatalytic activity, Journal of Materials Chemistry, 22 (2012) 4832-4836.

[151] J. Fei, Y. Cui, J. Zhao, L. Gao, Y. Yang, J. Li, Large-scale preparation of 3D self-assembled iron hydroxide and oxide hierarchical nanostructures and their applications for water treatment, Journal of Materials Chemistry, 21 (2011) 11742-11746.

[152] P. Madhusudan, J. Zhang, B. Cheng, G. Liu, Photocatalytic degradation of organic dyes with hierarchical $Bi_2O_2CO_3$ microstructures under visible-light, CrystEngComm, 15 (2013) 231-240.

[153] H. Li, G.T. Fei, M. Fang, P. Cui, X. Guo, P. Yan, L.D. Zhang, Synthesis of urchin-like Co_3O_4 hierarchical micro/nanostructures and their photocatalytic activity, Applied Surface Science, 257 (2011) 6527-6530.

[154] N. Fukata, T. Oshima, K. Murakami, T. Kizuka, T. Tsurui, S. Ito, Phonon confinement effect of silicon nanowires synthesized by laser ablation, Applied Physics Letters, 86 (2005).

[155] S. Osswald, V.N. Mochalin, M. Havel, G. Yushin, Y. Gogotsi, Phonon confinement effects in the Raman spectrum of nanodiamond, Physical Review B, 80 (2009) 075419.

[156] A.K. Arora, M. Rajalakshmi, T.R. Ravindran, V. Sivasubramanian, Raman spectroscopy of optical phonon confinement in nanostructured materials, Journal of Raman Spectroscopy, 38 (2007) 604-617.

[157] Z.-W. Fu, Y. Wang, Y. Zhang, Q.-Z. Qin, Electrochemical reaction of nanocrystalline Co_3O_4 thin film with Lithium, Solid State Ionics, 170 (2004) 105-109.

[158] D. Liu, X. Wang, X. Wang, W. Tian, Y. Bando, D. Golberg, Co_3O_4 nanocages with highly exposed {110} facets for high-performance lithium storage, Sci. Rep., 3 (2013).

[159] H.J. Fan, P. Werner, M. Zacharias, Semiconductor Nanowires: From Self-Organization to Patterned Growth, Small, 2 (2006) 700-717.

[160] L.-C. Hsu, H.-C. Yu, T.-H. Chang, Y.-Y. Li, Formation of Three-Dimensional Urchin-like α-Fe_2O_3 Structure and Its Field-Emission Application, ACS Applied Materials & Interfaces, 3 (2011) 3084-3090.

[161] Physical Constants of Inorganic Compounds in Handbook of Chemistry and Physics, 87th ed., CRC Press, Taylor&Francis Group, Boca Raton,2006.

[162] J.A.S. R. A. Jones, J. A. Stunkard, J. Siegel, Effects on experimental animals of long term Inhalation expousre to carbon monoxide, Toxicol. Appl. Pharmacol, 19 (1971) 46-53.

[163] G.V.E. B. Lewis, in Combustion, flames and explosions of gases,, 3rd ed. ed., Academic Press, Orlando, 1987.

[164] Y.F.Y. Yao, J. Catal. , 87 (1984) 152 –162.

[165] G. Ertl, Science, 254 (1991) 1750 –1755.

[166] D.D. J. Barbier Jr, Appl. Catal. B 3(1993) 61 –83.

[167] R.J.F. R. M. Heck, Catalytic Air Pollution Control, 2nd ed., Wiley, 2002, Chap. 6, pp. 69–129.

[168] C.D.i. D. Duprez, Catalysis by Ceria and Related Compounds, (Ed.: A. Trovarelli), Imperial College Press, 2002, pp. 243– 280.

[169] S. Royer, D. Duprez, Catalytic Oxidation of Carbon Monoxide over Transition Metal Oxides, ChemCatChem, 3 (2011) 24-65.

[170] N. Sheppard, T. T. Nguyen, Advances in Infrared and Raman Spectroscopy, Vol. 5 (Eds.: R. E. Hester, R. J. H. Clark) Heyden, London, 1978, pp. 67.

[171] X. Xie, Y. Li, Z.-Q. Liu, M. Haruta, W. Shen, Low-temperature oxidation of CO catalysed by Co_3O_4 nanorods, Nature, 458 (2009) 746-749.

[172] L.-C. Wang, Q. Liu, X.-S. Huang, Y.-M. Liu, Y. Cao, K.-N. Fan, Gold nanoparticles supported on manganese oxides for low-temperature CO oxidation, Applied Catalysis B: Environmental, 88 (2009) 204-212.

[173] J. Zhu, Q. Gao, Z. Chen, Preparation of mesoporous copper cerium bimetal oxides with high performance for catalytic oxidation of carbon monoxide, Applied Catalysis B: Environmental, 81 (2008) 236-243.

[174] H. Tuysuz, M. Comotti, F. Schuth, Ordered mesoporous Co_3O_4 as highly active catalyst for low temperature CO-oxidation, Chemical Communications, (2008) 4022-4024.

[175] D.R. Merrill, C.C. Scalione, The catalytic oxidation of carbon monoxide at orfinary temperatures, Journal of the American Chemical Society, 43 (1921) 1982-2002.

[176] C. Yoon, D.L. Cocke, The design and preparation of planar models of oxidation catalysts: I. Hopcalite, Journal of Catalysis, 113 (1988) 267-280.

[177] M. Haruta, N. Yamada, T. Kobayashi, S. Iijima, Gold catalysts prepared by coprecipitation for low-temperature oxidation of hydrogen and of carbon monoxide, Journal of Catalysis, 115 (1989) 301-309.

[178] D.L. Trimm, Z.I. Önsan, Onboard fuel conversion for hydrogen-fuel-cell-driven vehicles, Catalysis Reviews, 43 (2001) 31-84.

[179] S.-H. Oh, G.B. Hoflund, Low-temperature catalytic carbon monoxide oxidation over hydrous and anhydrous palladium oxide powders, Journal of Catalysis, 245 (2007) 35-44.

[180] Y.Xu, J.Ma, Y.Xu, L.Xu, L. Xu, H. Li, H. Li, Palladium nanoparticles encapsulated in porous silica shells: an efficient and highly stable catalyst for CO oxidation, RSC Advances, 3 (2013) 851-858.

[181] M. Jin, J.-N. Park, J.K. Shon, J.H. Kim, Z. Li, Y.-K. Park, J.M. Kim, Low temperature CO oxidation over Pd catalysts supported on highly ordered mesoporous metal oxides, Catalysis Today, 185 (2012) 183-190.

[182] I. Dobrosz-Gómez, I. Kocemba, J.M. Rynkowski, Factors influencing structure and catalytic activity of $Au/Ce_{1-x}ZrxO_2$ catalysts in CO oxidation, Applied Catalysis B: Environmental, 88 (2009) 83-97.

[183] B. Qiao, A. Wang, X. Yang, L.F. Allard, Z. Jiang, Y. Cui, J. Liu, J. Li, T. Zhang, Single-atom catalysis of CO oxidation using Pt1/FeOx, Nat Chem, 3 (2011) 634-641.

[184] Y.-Z. Wang, Y.-X. Zhao, C.-G. Gao, D.-S. Liu, Origin of the High Activity and Stability of Co_3O_4 in Low-temperature CO Oxidation, Catalysis Letters, 125 (2008) 134-138.

[185] N.R.E. Radwan, M.S. El-Shall, H.M.A. Hassan, Synthesis and characterization of nanoparticle Co_3O_4, CuO and NiO catalysts prepared by physical and chemical methods to minimize air pollution, Applied Catalysis A: General, 331 (2007) 8-18.

[186] L.F. Peiretti, I.S. Tiscornia, E.E. Miró, Study of the synthesis of CeO_2 nanoparticles for their use in CO preferential oxidation (COPrOx), Chemical Engineering Journal, 223 (2013) 507-515.

[187] L.F. Liotta, H. Wu, G. Pantaleo, A.M. Venezia, Co_3O_4 nanocrystals and Co_3O_4-MOx binary oxides for CO, CH_4 and VOC oxidation at low temperatures: a review, Catalysis Science & Technology, 3 (2013) 3085-3102.

[188] L.E. Gómez, E.E. Miró, A.V. Boix, Spectroscopic characterization of Mn–Co–Ce mixed oxides, active catalysts for COPROX reaction, International Journal of Hydrogen Energy, 38 (2013) 5645-5654.

[189] Y. Gou, X. Liang, B. Chen, Porous Ni–Co bimetal oxides nanosheets and catalytic properties for CO oxidation, Journal of Alloys and Compounds, 574 (2013) 181-187.

[190] X. Yan, Q. Huang, B. Li, X. Xu, Y. Chen, S. Zhu, S. Shen, Catalytic performance of $LaCo_{0.5}M_{0.5}O_3$ (M = Mn, Cr, Fe, Ni, Cu) perovskite-type oxides and $LaCo_{0.5}Mn_{0.5}O_3$ supported on cordierite for CO oxidation, Journal of Industrial and Engineering Chemistry, 19 (2013) 561-565.

[191] Y. Feng, L. Li, S. Niu, Y. Qu, Q. Zhang, Y. Li, W. Zhao, H. Li, J. Shi, Controlled synthesis of highly active mesoporous Co_3O_4 polycrystals for low temperature CO oxidation, Applied Catalysis B: Environmental, 111–112 (2012) 461-466.

[192] Y. Yu, T. Takei, H. Ohashi, H. He, X. Zhang, M. Haruta, Pretreatments of Co_3O_4 at moderate temperature for CO oxidation at −80°C, Journal of Catalysis, 267 (2009) 121-128.

[193] X.-Y. Pang, C. Liu, D.-C. Li, C.-Q. Lv, G.-C. Wang Structure Sensitivity of CO Oxidation on Co_3O_4: A DFT Study, ChemPhysChem, 14 (2013) 204-212.

[194] L. Hu, K. Sun, Q. Peng, B. Xu, Y. Li, Surface active sites on Co_3O_4 nanobelt and nanocube model catalysts for CO oxidation, Nano Res., 3 (2010) 363-368.